UNIVERSIDAD COMPLUTENSE DE MADRID
FACULTAD DE CIENCIAS FÍSICAS

TESIS DOCTORAL

Acquisition Systems and State-Of-Art Radiation Detectors for Basic Nuclear Physics and Medical Imaging

Sistemas de Adquisición de Datos y Detectores de Radiación de Última Generación para Física Nuclear Básica e Imagen Médica

MEMORIA PARA OPTAR AL GRADO DE DOCTOR

PRESENTADA POR

Víctor Sánchez-Tembleque Verbo

DIRECTORES

José Manuel Udías Moinelo
Luis Mario Fraile Prieto

Madrid

UNIVERSIDAD COMPLUTENSE DE MADRID
FACULTAD DE CIENCIAS FÍSICAS

TESIS DOCTORAL

Acquisition Systems and State-Of-Art Radiation Detectors for Basic Nuclear Physics and Medical Imaging

Sistemas de Adquisición de Datos y Detectores de Radiación de Última Generación para Física Nuclear Básica e Imagen Médica

MEMORIA PARA OPTAR AL GRADO DE DOCTOR

PRESENTADA POR

Víctor Sánchez-Tembleque Verbo

DIRECTOR

José Manuel Udías Moinelo
Luis Mario Fraile Prieto

A Felix, Floren, Dani y Alonso

Soy quién soy gracias a vostros.

El ordenador nació para resolver problemas que antes no existían.

Bill Gates

Agradecimientos

Bueno, finalmente me encuentro aquí, y mira que creo que hay gente que no lo creía posible y que pensaría que buscaría cualquier excusa u ordenador roto para distraerme y seguir con esta tesis un poco más. Y quizás parte de razón no les falte, pero eso es sólo una prueba de que, como en todo viaje interesante, en el fondo queremos que dure un poco más. Y como también todo viaje tiene un final, y en este final es de bien nacidos el ser agradecido, he de agradecer a todas las personas que me han ayudado a estar aquí.

La primeras personas a las que quiero agradecer esto es a mis directores, para José Manuel Udías solo puedo tener buenas palabras y un inmenso respeto intelectual, él me dio la oportunidad de embarcarme en este viaje, y es una de las personas que más conocimiento creo que puede haberme trasmitido, si algún día consigo que mi mente albergue un pequeño porcentaje de su conocimiento, de verdad que podría darme por contento. Para Luis Mario Fraile sólo tengo palabras de agradecimiento por haberme dado la oportunidad de viajar a tantos experimentos distintos, en los que poder formarme y aprender de muchos compañeros.

También quiero agradecer a este grupo profesional, y más que profesional, un grupo de gran calidez humana con él que he tenido la suerte de estar y que es el GFN. A los postdoc que me encontré cuando llegué, como Mariano, el cual tuvo la paciencia de sentarse conmigo toda una tarde frente a un código de FORTRAN y sin que él lo quisiese (porque estoy seguro de que no lo quería) hacer que hasta me gustase este lenguaje y a Dani, que pese a ser claramente un estudiante infiltrado, su versatilidad a la hora de buscar nuevos proyectos me ha dado la oportunidad de probar mis cacharros en los sitios mas dispares. A los que no eran postdocs, pero que me demostraron que se puede llegar a ello, como Vadym y su peculiar forma de ver la vida, Maylin con su buena voluntad y alegría, Paula, una chica muy maja e inteligente pero que quizás tiene demasiados gatos... y a Vicky, con su capacidad de sonreír ante toda adversidad, y a los postdoc que llegaron después, como Samuel y Joaquín, con un gran talento y quizás un no tan gran sentido del humor, y Raúl, pura gracia y sabiduría andaluza.

No todo son agradecimientos para la gente con doctorado, pues creo que el GFN ha contado y sigue contando con un gran equipo de estudiantes (lo que solo me ha hecho preguntarme en más de una ocasión que hacía yo aquí entre ellos). De aquí quiero agradecer especialmente a dos personas, no por ningún motivo en especial, sino porque los pobres han tenido que trabajar conmigo más tiempo, y por tanto aguantarme más, a Jaime, quién desde hace tiempo sé que es la auténtica definición de mejor persona y para el que sólo espero, y sé que tendrá, un futuro profesional de lo más próspero y a Miguel, el cual me ha acompañado en ese extraño arte de montar detectores durante tanto tiempo. También agradecer a ese cuarteto que es la representación del trabajo duro combinado con la majez máxima como son Pablo, Amaia, Alex y Oli. A mis compis de medidas en el CMAM y que también han tenido que soportar mis montajes, Víctor (futuro cabeza de experimentos), Andrea y Aidana, y al resto de nueva savia como son Fer, Clara y Murias. Tampoco quiero olvidar a aquellos cuyo paso fue más breve pero de los que también tengo un buen recuerdo, Fran, Pedro, Jen, Miguel Alto, Pauline, Estefania y Araceli. En definitiva, gracias a todo el GFN por haberme hecho sentir integrado en un gran ambiente de trabajo.

También he de agradecer al grupo de Magdalena Kowalska por la oportunidad de experimento que nos plantearon y que ha sido muy interesante trabajar en él, y a Carolina Gutiérrez, a la cual, creo que la hemos obligado a hacer demasiadas horas en el CMAM, y pese a todo ha seguido siempre con una sonrisa.

Finalmente quiero agradecer a toda mi familia y amigos el apoyo que me han dado durante todo este tiempo, especialmente a mis padres y mis hermanos, que los pobres creo que han sufrido más mi tesis que yo mismo.

En definitiva, gracias a todos estas personas con las que he tenido el privilegio de estar todos estos años.

Contents

Summary

Current experimental nuclear physics requires the continuous development of new detection and analysis systems, whose characteristics and properties surpass those already existing. These systems are not only useful in experimental nuclear physics, but they are of interest in any field where nuclear radiation detector is required, such as nuclear medicine and radiotherapy, where imaging and monitoring techniques are in continuous evolution and development.

The main goal of this thesis is to explore electronics for data acquisition (DAQ) to be used in these experiments, taken from the digital domain. Indeed, we study techniques based on the digitization of the signal from the different detectors analyzed in this work. The main advantage of digitizing these signals is that by doing so, we have a complete control over the processing and analysis of the signal, without the need for specific analog electronics. In this thesis, the digitization of signals has been covered from two different angles:

1. Digitizing the detector signals with high precision, using a high speed digitizer with a sampling speed fulfilling the Nyquist criteria and thus recording the full bandwidth of the signal, into a large number of bits (>12 bits) of resolution for the sampled signals. By doing this we obtain a signal which contains all the information in the original analog pulses. Once the data are digitized, highly complex processing algorithms can be tested that are difficult to reproduce with conventional analog electronics. With this methodology, we show that, using a sufficiently powerful digitizer and processing algorithms, the state of the art results based in the conventional analysis of analog pulse shaping can be easily matched or even surpassed.

2. The other division of DAQ focuses towards inexpensive, very compact, very versatile digital oscilloscopes. We have designed digital DAQ (DDAQ) where we have shown that with the right signal processing algorithms, even with less resolution and limited sampling, these systems can be an economical alternative to much more complex acquisition systems. They also exhibit a performance that perfectly suits the requirements of the experimental activities of our group.

Following these two different approaches to DDAQs, we have grouped the chapters of this thesis

as follows:

In **chapter 1**, a brief explanation of the operation of the detectors used is presented, as well as an introduction to digital processing along with the different alternatives for digitization.

This is followed by the part of the thesis aimed at processing with high sampling rate, high-resolution digitizers. In **chapter 2** we propose and validate a DDAQ system and data processing algorithm based upon machine learning that finds the optimal signal processing to measure both time and energy. In addition, to advance on the improvements offered by this system, in **chapter 3** we have explored the possibilities it offers when used to characterize two new types of detectors.

The second block of this thesis describe simpler digitizing systems designed for three different experiments of our group, where they were shown to perfectly perform according with the standards required by each of these experiments. In **chapter 4** a system has been tested to measure the activation cross section of different materials after being irradiated with a proton beam, with the aim of determining their viability as possible contrasts for range validations in protontherapy. In **chapter 5** a system for the determination of the temporal structure of a clinical LINAC accelerator has been discussed. This information is necessary for the development of models that can reproduce the acoustic waves generated after the deposition of doses in a tissue, and can be used for monitoring it. And finally, in **chapter 6** a system has been proposed for the measurement of a new type of medical image called Polarized Nuclear Imaging (PNI) or also $\gamma-$MRI. This technique is based on the detection of the asymmetric emission of radioactive hyperpolarized nuclei in a magnetic field.

Resumen en castellano

En la actualidad, en física nuclear experimental es de gran importancia el desarrollo continuo de nuevos sistemas de detección y análisis, cuyas características y propiedades superen a los ya existentes. La aplicación de estos sistemas no se restringe a la física experimental, sino que pueden ser aplicados en cualquier ámbito en que sea necesario medir radiación nuclear, como en medicina nuclear y radioterapia, donde las técnicas de imagen y monitorización, que están en continua evolución y desarrollo, precisan de unos sistemas de detección cada vez más precisos y económicos.

El objetivo principal de esta tesis radica en la exploración de alternativas puramente digitales para la electrónica de adquisición (DAQ). Para ello hemos trabajado con técnicas basadas en la digitalización de la señal proporcionada por los distintos detectores analizados en este trabajo. La principal ventaja de digitalizar estas señales es que nos proporciona un control completo sobre el procesado y análisis de la misma, con gran versatilidad, sin necesidad de una electrónica específica para cada necesidad y que puede ser mucho más compleja. En el trabajo realizado en esta tesis, la digitalización de las señales se ha estudiado en dos vertientes distintas:

- Digitalizando las señales del detector con una alta precisión, es decir, un muestreo que cumple el criterio de Nyquist para representar todas las frecuencias de la señal, y con alta resolución ($>$ 12 bits) en la discretización de los valores de las muestras. Haciendo esto obtenemos una réplica digital de la señal analógica sin perder ni un ápice de información: Sobre los datos digitalizados se pueden probar formas de procesado de una alta complejidad que difícilmente son reproducibles con electrónica analógica convencional. Con esta metodología, demostráremos que con un digitalizador suficientemente potente, el estado del arte del análisis analógico de pulsos puede ser fácilmente igualado o incluso superado por el procesamiento digital.

- El desarrollo de un DAQ digital barato, flexible y compacto, basado en osciloscopios digitales con prestaciones más básicas, tanto por número de muestras como por capacidad de muestreo. Hemos podido demostrar que con el procesado de señal adecuado, pueden ser una alternativa económica a sistemas de adquisición mucho más complejos, con un rendimiento que cumple perfectamente con los requisitos de los experimentos donde han sido probados.

De acuerdo con la anterior división, hemos dividido los capítulos de esta tesis de la siguiente forma:

En el **capítulo 1**, se presenta una breve explicación del funcionamiento de los detectores utilizados, además de una introducción al procesado digital y de las distintas alternativas disponibles a la hora de realizar este procesado.

A continuación entraríamos en la parte de la tesis destinada al procesado con digitalizadores de alta resolución, para ello, en el **capítulo 2** se propone y valida un sistema de procesado basado en el uso de algoritmos inteligentes, o de aprendizaje automático, que determinan el procesado de señal óptimo para realizar medidas de tiempo y energía. Además, para avanzar sobre las mejoras que ofrece este sistema, en el **capítulo 3** se ha utilizado para caracterizar dos nuevos tipos de detectores.

El segundo bloque de esta tesis presenta sistemas de digitalización más sencillos que han sido diseñados para tres experimentos distintos. Con ellos hemos demostrado que perfectamente pueden satisfacer las necesidades requeridas por cada experimento. En el **capítulo 4** se ha probado un sistema para medir la sección eficaz de activación de distintos materiales tras ser irradiados con un haz de protones, con el objetivo de determinar su viabilidad como posibles contrastes para validaciones de rango en protonterapia. En el **capítulo 5** se ha desarrollado un sistema para la determinación de la estructura temporal de un haz clínico tipo LINAC. Esta información es necesaria para el desarrollo de modelos que puedan reproducir la ondas acústicas generada tras la deposición de dosis en un tejido, y que pueden ser utilizadas para su monitorización. Y finalmente, en el **capítulo 6** se ha propuesto un sistema para la medición de un nuevo tipo de imagen médica llamada Imagen Nuclear Polarizada (PNI), o también $\gamma-$MRI. Esta técnica está basada en la detección de la emisión asimétrica de radiación de elementos radioactivos, los cuales han sido previamente hiperpolarizados.

Chapter 1

Brief Introduction to Detection in Nuclear Physics

1.1 Introduction

Radiation emissions result from the release of energy and matter from unstable nuclei[1]. The radiation emitted in these processes may be electromagnetic (photons) or other particles. The electromagnetic radiations consist of x-rays and γ-rays while the corpuscular emissions include α-particles, β-electrons, positrons, internal conversion electrons, Auger electrons, neutrons, protons, and fission fragments, among others [2].

These nuclear processes are involved in many applications. For example in nuclear medicine, that is based in the detection of an injected tracer, labeled with a γ-rays emitter. Detection of the radiotracer provides an image of the distribution of the labeled molecule in the body, and hence of the compound to which it was attached. [3].

In order to optimize the information obtained in nuclear imaging, it is important to improve the information obtained with the nuclear detector systems employed. The main goal of this thesis is to develop and to improve the information obtained during radiation detection, not only for its application in nuclear medicine, (although in this thesis this will bear a especial interest because of our developments in this field), but in a more general way, showing improvement that could be used in any nuclear physics experiment or applications.

In this first chapter, we are going to present a brief introduction of the basic operation of the nuclear detectors developed in this work and a explanation of how the acquisition systems employed work, and at the end of the chapter we will summarize the research activities of the group where these systems were employed.

1.2 Radiation Detection

Ionizing radiation is detected identifying the ionization produced by the radioactive particle when it interacts with matter. Scintillator materials are used for these purposes very often, due to their main characteristic, that is, absorbing the energy deposited by the ionizing radiation, converting it into internal excitation energy of the material, and a subsequent de-excitation, returning (part of) the energy absorbed as visible light[2, 4]. This light can be collected and by means of a photodetector, transformed into an electrical pulse that can be recorded in a computer. In this section we will briefly explain how scintillators work and the usual inner wokings of a scintillator detector.

1.2.1 Scintillator Detectors

Scintillator materials are divided into organic or inorganic compounds. In this thesis the main scintillators used are of the inorganic type. The mechanism of scintillation of inorganic crystals is based in the electronic band structure of the crystal[4]. When a ionizing particle reaches the crystal, two processes can happen. On the one hand, a electron of the valence band is promoted to the conduction band, generating an electron-hole pair. On the other hand, the electron is promoted into the excitation band, usually located just below the conduction band. In this case, the electron and the hole form a bound state known as an exciton. In a crystal free from impurities, the forbidden gap between valence and conduction bands can not be populated by electrons, but if the scintillator crystal is doped with even the slightest amount of impurities, intermediate energy levels may be formed in the forbidden energy gap of the crystal. These levels are known as *electron traps*, because if a free hole or a bound state interacts with the impurity, it can be ionized and further when a free electron interacts with the impurity, it can be trapped in these level [5].

The de-excitation of these intermediate levels is called luminescence center. Due to the fact that the energy gap between valence and conduction bands is larger than the energy of the photon produced in the de-excitation, the crystal is transparent to these de-excitations photons. Usually these photons lie within the visible spectrum.

We can enumerate the following important characteristics of scintillator crystals[4, 6]:

- **Photon Yield:** The number of photons produced in the crystal by unit of energy deposited in it by the incident radiation. Larger photon yield implies smaller statistical error in the determination of the energy of the incident radiation.

- **Spectral Range Emission:** It is the frequency of the photons emitted and it is relevant during selection of the most suitable photon detector.

- **Decay Constant:** This is the mean-life of the luminescence process on the crystal. Short decay constants imply better time resolution and prevent pile-up of pulses events at high rate emissions.

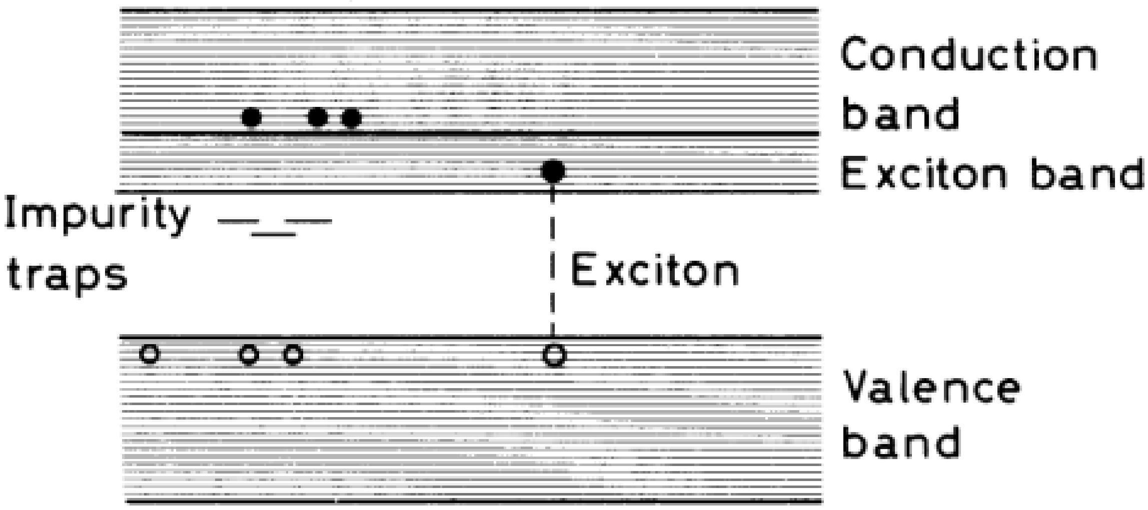

Figure 1.1: Example of electronic band structure in an inorganic scintillator material [4]

- **Z Effective:** In order to favor that the γ-ray deposits all its energy in the crystal, scintillators with a higher Z effective number are favoured to detect photons.

1.2.2 Light Collection System

The light emitted by the crystal is collected or directed to the photodetector which converts the light into a electric pulse whose charge will be proportional to the number of incident photons. As the number of visible photons produced in the scintillator is proportional to the energy deposited in the crystal, the charge of this pulse will be also proportional to the energy deposited. In the following we describe the main photodetectors that have been used in this thesis.

1.2.2.1 Photo Multiplier Tubes

A photomultiplier tube (PMT) consists of a vacuum tube that convert the incident light into a electric signal[4, 2]. A typical structure of the PMT is like this: At the beginning of the tube there is a photosensitive material, known as the photocathode. This material is designed to convert the incident photon into an electron by the photoelectric effect. The electrons emitted in the photocathode are emitted into the vacuum region inside the tube, for this purpose they are accelerated with high voltage potentials existing between the photocathode and metal plates named dynodes. The electron is accelerated and strikes the first dynode. This collision of the accelerated electron with the dynode generates a cascade of secondary electrons. As the voltage continually increases in between contiguous dynodes, primary and secondary electrons are accelerated and generate new cascades at each dynode. Finally, we have the anode at the end of the tube where all the charge is collected. Thanks to the secondary electrons released at each stage, PMTs exhibit exponential gain factors, so that for each electron generated in the photocathode, millions of electrons can reach the anode. The number of these electrons at the anode are proportional to the incident light in the PMT, thus we obtain the seeked correlation energy-charge.

1.2.2.2 Silicon Photomultipiers

Silicon Photomupliers (SiPMs) are a relative new type of light detector. SiPM appeared in the 2000's [7, 8] and they are becoming the most likely substitutes to the PMTs known for decades. SiPM are build from the union in parallel of a huge number (hundreds to thousands) of avalanche photo diodes (APD)[9]. An APD is a p-n junction where a reverse bias has been applied. This bias increases the depletion region where no mobile charge carriers are available and sets up an electric field across this zone. If an ionizing particle interacts in this depletion zone, a pair hole-electron is generated. The electric field existing in that region produces a current at the same time that the generated pair is expelled from the depletion zone. If the bias voltage is larger than a certain value (breakdown voltage), the acceleration of charge carriers in the depletion band can provide enough kinetic energy to these carriers so that they can generate secondary pairs, that will be accelerated too and they will escalate exponentially the process. When the p-n junction is reversed bias very close or above to the breakdown voltage, the device is working in Geiger mode, where an ionization turns on conduction, the current generated being limited only by a quenching resistor. This macroscopic current can be used to count single photons. Indeed, when we sum the contribution multiple APDs in parallel, we will have a combined current whose value depends on the number of activated cells (correlated to the number of incidents photons). Doing this we can correlate the charge recollection with the energy deposited on a scintillator crystal.

There are several reasons that explain why SiPMs are increasingly replacing traditional PMTs:

- **Low Power Supply:** The breakdown voltage of commercial SiPMs is normally around 30-80 V, very low compared with the high voltage ($>$500V) needed for PMTs.

- **Compact Size:** As SiPM are based in semiconductor junctions which take up very little space, they can be very small devices.

- **Independence of magnetic field** PMTs are susceptible of magnetic field because of the long path that the accelerated electrons have to go throw the vacuum tube. On the contrary, SiPMs are immune to very strong magnetic fields.

Although these advantages makes replacing PMTs by SiPMs very worthy, we have to take into account that still there are some disadvantages in SiPMs:

- **Temperature Dependence:** Although the new models improve year after year, there is still a dependence of the breakdown voltage of SiPMs with temperature. Higher temperatures increases voltage breakdown implying a variation on the gain. This temperature dependence is continually decreasing on the new SiPMs.

- **Parasitic Capacitance:** Being made of thousand of cells or p-n junctions in parallel, the added parasitic capacitance of SiPM can be an inconvenient, especially if we intend to read several SiPMs at the same time.

The implications of these inconveniences will be described in more detail in the next chapters.

1.3 Signal Processing

The electric signal provided by the photodetector, in the form of electric pulses, can be analyzed in order to extract the energy and the time of arrival of the radiation to the detector, and often other important information as the kind of radiation or particle. There are two main ways to process the pulses[10]: a) the traditional way, that use analogical electronic chains to shape the signal and to digitize energy and time from the pulse adequately shaped by analog circuits and b) the fully digital way, where the signal is fully digitized, sent to a computing device (PC or similar) and fully processed *in silico* (performed completely on computer), that is, with digital filters and algorithms to extract time, energy and other information from the pulse. We will describe briefly both methods.

1.3.1 Analog Pulse Processing

Readout systems, or data acquisition electronics (DAQ) for particle detectors have been performed for decades, using an electronics chain where analog circuits shape the pulse in different ways. Most often, these analog preamplifiers, shaping amplifiers an other circuits take the shape of modular electronics (nuclear instrument modules or NIM)[4]. These modules are arranged differently, depending on whether time or energy measurements are aimed for. Thus, usually the electric signal is split into two different paths, if we want to know both time and energy.

The first stage that we usually find is a preamplifier, a very low noise analog circuit that receives the weak signal generated by the detector and produces an output signal suitable for the transmission through a cable up to the remaining readout electronics. One can divide preamplifiers into two families[10]: charge sensitive preamplifiers (normally used for energy measurements) and current sensitive preamplifiers, also known as fast amplifiers or wideband amplifiers, most often found in timing measurements.

Charge preamplifiers convert the charge produced in the detector into a voltage amplitude. A simple integration circuit with a capacitor in parallel with a discharge resistor is a typical representation[4, 2]. The integration time constant is usually large. producing slow pulses, which we have to deal with at later stages to avoid pulse pile-up.

After the preamplifier, the pulse is integrated, amplified again and shaped, in order to suit the expected application. Often, a high pass filter (or differentiator filter) is applied to shorten the long decay tail of the pulses. This kind of circuit is easily pictured as a combination of capacitor and resistor (CR) circuit[4, 2]. Afterwards, there are various possible options depending on the information we want. For energy measurements, normally a Gaussian shape for the pulse is preferred. This is obtained with various consecutive integrator stages after a the first CR circuit. With a Gaussian pulse the 'energy' information of the original pulse can be found by digitizing the peak (maximum) of the pulse[2]. If we want timing information, we can use a further CR circuit, which differentiates the signal and produces a bipolar pulse, where the zero cross-point can be taken as time stamp[4].

Finally we have to store the energy/time information of the pulses in a computer or a system to perform pulse-height histograming. Thus an analog to digital converter (ADC) will be employed. ADCs transform the processed signal in a unique digital value where is represented the information that we are looking for. For example, in the energy measurements, we determine the maximum peak value of the shaped Gaussian and we convert into a digital form using a peaking ADC.

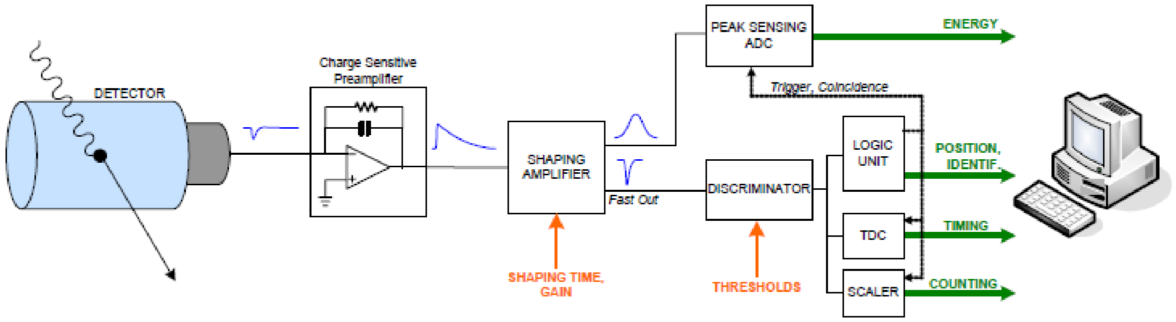

Figure 1.2: Analog chain in nuclear detection [10].

1.3.2 Digital Pulse Processing

Another way of signal processing, which is becoming increasingly available, as most of our common electronics (radio, TV, phone, etc.) are becoming digital, is to digitize the whole pulse, at an speed (number of samples) high enough to capture all the relevant information of the peak. When an event is identified (trigger conditions are met), we use fast ADCs to sample the pulse and send these digital samples to the computer[10], where pulse processing takes over by the digital realm. That is, a difference with the so-called analog DAQ as described in the previous system, where the signal is shaped and filtered and only at the end of this analog processing, some component of the signal (the integral, the maximum of the peak, etc) is digitized to be stored in a computer, in the digital pulse processing, the signal is digitized as soon as possible right after the detector, pulse shaping takes place on the digitized samples instead of on the analog pathways.

There are two basic properties of the digitizer that have to be taken into account when we digitize a signal. First, the number of bits of the digitizer, representing the resolution, or minimum variation that can be recorded. The higher the number of bits, the better resolution and fidelity of the digital signal. The other important parameter of digitizers is the sampling rate, that is, the maximum number of samples that we can digitize by unit of time, measured in samples per second or more often in Gigasamples per second, or Gs/s. Sampling rate impacts the maximum frequency (half of the sampling rate, at most, under ordinary conditions) content of the original signal that we can recover in the digitized version, according to the Nyquist criteria[11]. Other important parameters of digitizers are the integral and differential linearity[4] and the maximum voltage span.

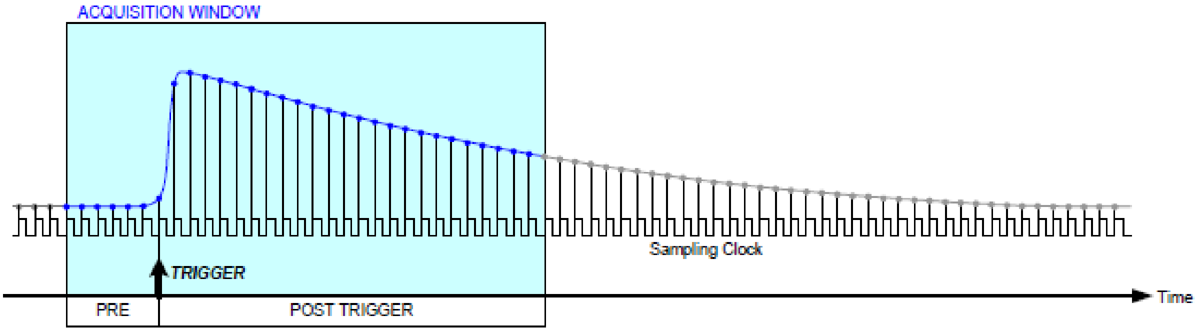

Figure 1.3: Signal digitized with multiples ADCs [10].

Fully-digital acquisition systems have multiple advantages with respect to the mostly analog processing:

- **Simplicity:** The same board can acquire and digitize data for energy and time coincidences, preserving the original pulse properties.

- **Flexibility:** Any kind of processing and filter is possible, even if they do not have an analog circuit' representation: median filter, recursive filters, Fast Fourier Transforms and frequency based filters.

- **Stability and noiseless:** Once digitized, the data is immune to noise, temperature changes, etc...

- **Versatility:** The same raw digitized pulses can be studied with different data processing or algorithms. This is useful to optimize filters *in silico* without the need to repeat the measurements with different setups.

On the other hand, very fast, high resolution digitizers are still an expensive alternative, they require very powerful computers or otherwise dedicated hardware, but digital electronics and DSPs (digital signal processors) are ubiquitous and ever growing in performance and shrinking in price.

1.4 Choice of Digitizer

There are several factors to consider when choosing a digitizer. We can identify three different strategies when we aim to digitize an experiment:

- First one, employing a simple standalone digital oscilloscope. Digital scopes nowadays have a variable bit resolution, depending on the cost, and the possibility of different sampling rates and number of channels. They are employed in many applications, not only nuclear pulse processing, and thus they are inexpensive and readily available from many vendors. They rely on a computer to store and process the pulses. A limitation of this alternative is a possible bottleneck in the data transfer from the oscilloscope to the computer. They present normally with two acquisition modes: a) Block mode, where a number of signals (pulses in our case) is acquired and stored into the oscilloscope memory, and once the internal buffer of the oscilloscope is full, this buffer is sent to the computer. Usually, while the oscilloscope is sending the data, it will not be ready to acquire further pulses, possibly introducing dead times in the acquisition. With the introduction of fast communication protocols such as USB3.0, the performance of this solution may be very interesting. b) Streaming mode, where the signal digitized is continuously sent to the computer where is stored or processed. In this mode, sampling rate is limited by data transfer from the oscilloscope, over USB 2.0 or 3.0 connection. The maximum sampling rate depend on the computer, but for 4 channels and 8 bits samples, sampling of 30 MS/s per channel are typical. The advantages of this solution are the easy deployment and the low price, being possible to build a system to acquire millions of events per second for under 1 k€, including the PC.

- The second strategy is based on incorporating computing capability on the external device, the digitizer itself, off-loading the pulse processing operations outside the computer. External digitizers with lots of fast memory and modern Field-programmable gate arrays (FPGAs), ASIC, or specialized DSP or CPUs, lie in this category. Instead of sending to the computer the whole data stream with all the samples from the pulse, the pulse is digitized and processed on-the-fly in the digitizer, using the capabilities of the device. Most modern choices include flexibility and programming capabilities, so that the user can change the factory algorithms. This approach reduces immensely the amount of data to be sent to the PC: now it will be only the energy, timing and possibly some other shaping parameters. This highly reduces the dead time and sampling rate limitations of the former approach. There are some disadvantages too. These are more specialized devices, with less companies designing them (CAEN and NUTAQ among a few [12, 13]), thus with increased prices, and the processing flexibility is more limited and may involve a more step learning curve.

- Probably the most powerful, flexible and expensive alternative is to rely on modules that can be integrated inside a PC and communicate at the speed of the PCIe or PCIX buses of modern computers, orders of magnitude higher than the USB ports. More advanced modules will incorporate powerful DSP on board, and can communicate directly with GPUs on the computer to do the number crunching. These modules offer the advantages of fast processing, combined with the high speed of the standard PC bus. Modules with high sampling rates and higher number of bits (4 GS/s and 12 Bit [14, 15, 16]) are already common.

In this thesis we will survey several fully digital strategies to process nuclear experiments. In many cases, as a proof of concept, we have used the simplest digital oscilloscope and PC, with results that perfectly suit many experiments. There are several areas of research of the Nuclear Physics Group (GFN-UCM) [17], where this work has been developed, for which DDAQ have been employed and which we will describe in this thesis:

1. Fast timing experiments. The GFN-UCM has a long trajectory in fast-timing measurements. This technique, pioneered among others by H. Mach [18] is the speciality in the group. Indeed, Luis M. Fraile from GFN coordinates the development of FATIMA [19], a fast timing array for nuclear experiments. GFN deploys its detectors and expertise around the world, as needed, in facilities such as ISOLDE@CERN[20], ILL[21], Legnaro[22], etc. The applications of digital pulse processing to these measurements, which require good control of the energy of the pulses and exquisite timing performance, are one of the main parts of this work [23, 24, 25, 26, 27].

2. Prompt gamma and prompt PET measurements during proton irradiation. In the context of the PRONTO project, coordinated by Luis M. Fraile [28], we aimed to verify the proton range in protontherapy by monitoring the prompt radiation produced by protons in tissues. This application requires the ability to handle very high event rates for short periods of time, and good energy resolution, with fast detectors and fast pulse processing. It is also described in this thesis.

3. Dedicated DAQ for PET systems and other medical imaging modalities involving the detection of radiation. The GFN is also very involved in the design and developments of DAQ for PET scanners. This applications requires, above all, to sustain extremely high event rates (hundreds of millions of single events per second), with moderate time and energy resolution requirements. At GFN, digital processing has also been explored for this application [29, 30].

In this thesis we advocate that DDAQ, with high end digitizers, exceeds the performance of the traditional analog shaping DAQs. Either better time or energy of both, resolutions can be achieved with DDAQ, also higher rates can be sustained. Obtaining the maximum performance may require high-end digitizers so that the full integrity of the signal is maintained in the digital version, and as of today this is not always price-competitive with the analog strategy, but the

DDAQ performs better, provided the rigth algorithms are identified. The improvements with regards to the the analog DAQ are due to the versatility that the DDAQ allows, which makes it possible to try complicated filtering schemes, impossible in the analog-only shaping world, and to the ability to change the shaping and filtering strategies several times, even after data acquisition, looking for the best results. Indeed, we will see in the first chapters of this thesis, that DDAQ can be coupled to machine learning strategies, saving man-hours of optimization of the setup.

There is also another side to DDAQ. When we do not seek for maximum possible performance ever, but rather for a simple to handle, diagnose, calibrate, transport and deploy system, for the least possible money, nothing can beat these days the DDAQ systems based on commercial medium speed (1 Gs/s) digital scopes. In the second part of this thesis we will summarize several different applications with diverse nuclear radiation detection needs. With the conventional DAQ we would need to have at our disposal (and to carry) many different NIM modules, most of them different, for each of these applications, depending on whether the emphasis would be made on the time, the energy or the rates. However, the same DDAQ, with a mere change of the parameters of the software, performed more than well under these very different experimental situations, and for a fraction of the cost and the weight.

The confirmation that DDAQs based on state of the art digitizers can outperform even our best traditional DAQ which we have been optimizing for decades, presented in the first part of this work, convinced us to pursue a pure DDAQ strategy for our future scientific projects. However, in terms of the day to day activities of the GFN during the last four years, the introduction of the inexpensive and compact moderate speed and resolution DDAQ, taking advantage of the algorithms and experience acquired in our group to tune the high-end DDAQ counterpart, presented in the second part of this thesis, has completely revolutionized the way our group approaches the deployment of experiments.

Chapter 2

Optimizing Time-Pickup Algorithms in Radiation Detectors with a Genetic Algorithm

2.1 Introduction

As discussed in Subsection 1.3.2 of Chapter 1 fully-digital acquisition systems have multiple advantages compared to analog processing. Fully-digital acquisition systems, for which the pulses from the detectors are sampled at high rate, combined with appropriate pulse processing algorithms can easily simulate, recover, and even improve the results obtained with traditional electronics. In what concerns time measurements, high-speed pulse digital sampling has paved the way for the use of complex, non-standard algorithms to provide the time stamps for radiation detection events. The results supersede those based based upon Constant Fraction Discriminators (CFD), Time to Amplitude Converters (TAC) and multichannel Analog to Digital Converters (ADC) [31, 32, 33, 34].

The use of a DDAQ system has an important advantage: the limitations in the signal processing would only come from our (lack of) skills programming the algorithms; essentially we are not limited by the particular shaping electronics available during the acquisition. Digitized pulses can be stored for further off-line processing providing the opportunity to try many different strategies for signal filters and analysis with the same set of data. The actual difficulty comes from the fact that we have access to an almost infinite number of possible filters and algorithm parameters for signal processing, and it is practically impossible to test by hand all of them and to ensure that the time and/or energy resolutions obtained are the best that can be reached. We tried to solve this problem introducing machine learning techniques by means of a Genetic Algorithm (GA) [35], where the parameters that minimize the Coincident Resolving Time (CRT) could be automatically found by the computer in a reasonable time.

In this work, we use a GA [35] to tune the *in silico* digital filter, the digital time pick-up algorithm and their associated parameters. We compare the best filter obtained from the GA with an *in silico* implementation of CFD-TAC where the CFD parameters have been manually optimized based upon the same measurements, against a finely tuned conventional (CFD-TAC) electronics [33, 34]. The GA-tuned strategy improved the hand-tuned CFD timing performance by more than 10%, proving this method like a viable substitute for conventional systems. All the work presented on this chapter has already been published [23, 24, 25]

2.2 Material and Methods

2.2.1 Experimental Setup

The scintillators used in this study were two identical $LaBr_3$ crystals with the shape of a truncated cone of 3.8 cm in height and bases of 3.8 cm and 2.5 cm, and with a nominal Ce doping of 5% [36]. Both were coupled to a Hamamatsu R9779 PMT [37] operated at –1300 V, with a bialkali photocathode and a 2" window. This experimental setup is the same employed to record the best coincidence time resolutions reported to date with the same $LaBr_3$ scintillators [34]. Those previous measurements employed standard analog NIM electronics.

The DDAQ system is based on the Domino Ring Sampling (DRS4) board developed at the Paul Scherrer Institute (PSI) [38, 39]. The DRS4 is a switched capacitor array capable of sampling 8 input channels with a sampling speed of 0.7 to 5 Gs/s. The analog waveform is stored in 1024 sampling cells per channel read by a 14-bit ADC, with an analog bandwidth of 950 MHz and a noise level of 0.35 mV. The signal can be read after sampling via a shift register clocked at 33 MHz for external digitization. This work used the DRS4 evaluation board, which has four input channels and is read out and powered by a PC via an USB connection.

The dynode PMT signals were digitized, stored and used to perform the energy and time measurements. During digitization it is necessary to choose the optimum voltage range and sampling speed in order to obtain complete pulse information. For dynode signals a voltage range from –0.05 V to 0.95 V and 5 Gs/s of sampling speed were chosen. The anode output signals were terminated with a 50 Ω resistance for impedance matching. Attenuators were used to adapt the output signal of the PMTs to the ADC range of the DRS. In fig 2.1, a sketch of the setup used and its equivalent analog version are shown.

Time measurements were carried out with ^{60}Co and ^{22}Na radioactive sources. ^{60}Co source decays to ^{60}Ni by β emission. The excited level of ^{60}Ni decays to an intermediate level with a γ-ray of 1173 keV. This level has a half-life of 0.9 ps, so a second γ-ray of 1333 keV will be emitted almost immediately. Therefore we can consider that the two γ-rays are essentially simultaneous. The ^{22}Na source decays to ^{22}Ne by β^+ emission. In this case, the positron travels in the surrounding material and loses kinetic energy continuously, until it decelerates to a point where it can interact

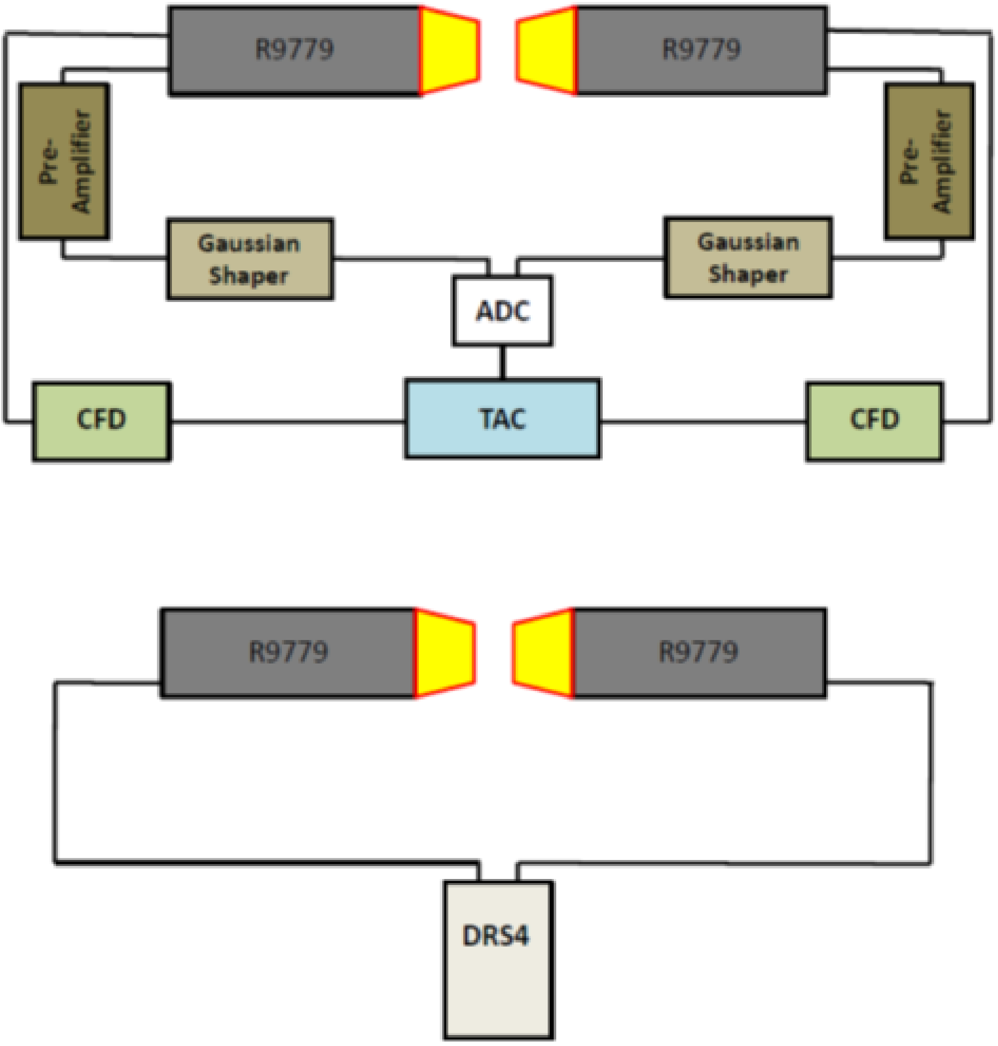

Figure 2.1: Sketch of the electronics of a conventional acquisition system for two $LaBr_3$ scintillators (top panel) compared to the fully digital acquisition chain used in this work (bottom panel).

with an electron. When this happens, both electron and positron are annihilated, producing two co-linear photons of 511 keV. It is important to note that this free path of the positron makes that the pair production is produced in different positions due the positron range, for different positrons emitted from the same source. This position uncertainty introduces a time of flight difference between both annihilation photons which can blur the time resolution, so it is generally observed a worse time resolution for the ^{22}Na coincidences with respect to the ^{60}Co source. This is further aggravated by the fact that ^{22}Na correspond to less energetic photons and thus smaller amplitude pulses than ^{60}Co. An internal logical AND trigger implemented in the DRS4 chip was used to record coincidence events within the DRS4 acquisition window of 200 ns. In order to reduce backscatter (photons that hit in one of the detector doing a Compton scattering and the resulting scattered photon is detected in coincidence in the other detector) and Compton events, energy gates were taken on full-energy peaks (FEP)s. For the ^{60}Co source, gates in the 1173- and 1332-keV FEPs were selected in both detectors. For the ^{22}Na source, a 511 keV gate was chosen. In this last case, the selection of energy gates could not avoid the presence of a small Compton background component arising from the 1275-keV ^{22}Na gamma-ray.

2.2.2 Pulse Interpolation

The DRS digitizes the pulse stored into their thousands of intrinsic cells, each containing a representation fo the pulse in a gven instant. Cells are not identical, and thus the time separation among samples is not equidistant[38, 39], albeit this time space is known for each pulse. Thus, before applying any time or energy algorithm to the stored pulses, we pre-processed the signals to obtain samples in equidistant time-intervals. The DRS4 evaluation board is provided with a tool to calibrate the individual cell delays. Figure 2 reports the time delays found for our particular board. The delays fall around two values, namely 0.12 and 0.26 ns, reflecting the dual inner design of the DRS chip, as mentioned [40]. Most algorithms are easier implemented for equidistant samples, the samples were interpolated with cubic splines into equally spaced (0.2 ns step) samples before processing. Other interpolation schemes have been mentioned in the literature [41], but for our purposes cubic splines performed well enough.

2.2.3 Algorithms for energy measurement

One of the main benefits of digitizing the signal coming directly from the PMT is the opportunity to obtain both energy and time information from the same signal. The development of algorithms to derive the energy of the pulses is not the main focus of this work, since we concentrate in time pickup. Nevertheless a good energy resolution is needed in order to apply energy gates to full-energy peaks and it is required in combination with time response in many nuclear applications.

We used the composite Simpson's rule [11] because it is easy to implement and it complies with our requirement of good energy resolution without the need of more complex algorithms such as a trapezoidal pulse-shaper [42]. We obtained the spectra shown in Fig. 2.3, with an energy resolution of 2.7% at 1332 keV and 5.0% at 511 keV.

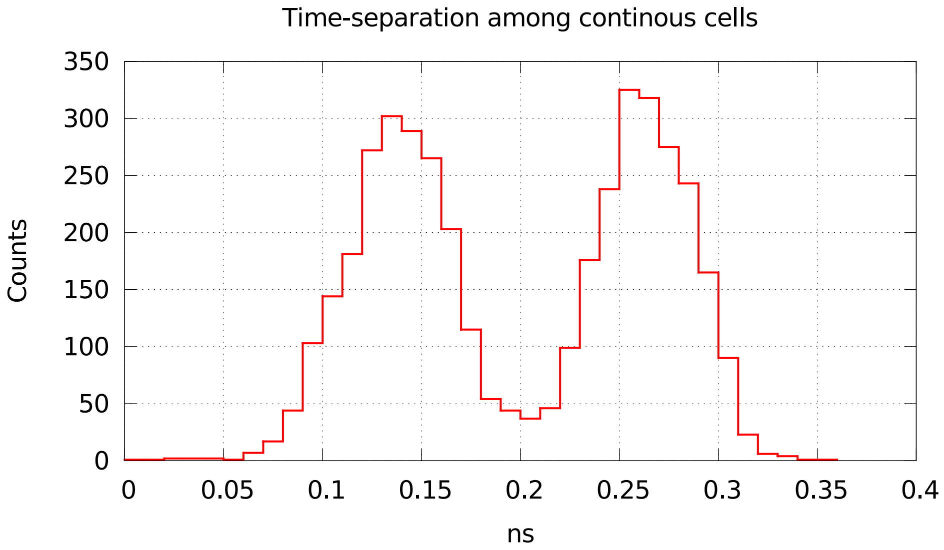

Figure 2.2: Time separation between contiguous samples for the 4 channels of DRS4 board at 5 Gs/s. This separation oscillates between 0.14-0.26 ns providing a sampling rate of 5 Gs/s (200 ps) on average, but making it convenient to use an interpolation routine to translate to pulses with regular sampling.

2.2.4 Genetic Algorithm

Genetic Algorithms are a specific kind of stochastic optimization methods based upon the idea of evolution. There are many excellent textbooks on GA [43, 44, 45, 46, 47, 48]. Here we will describe the main features of GA that are needed to understand our implementation. The particular implementation we use has been developed in our group and applied to several different problems [35, 49]. GAs build sets of possible solutions (also called individuals or genes) of a given problem to form a population. Each individual in the population represents a given value of the parameters explored and is classified according to its fitness value, in our case the value of the CRT, smaller CRT means better individuals. GAs implement operators such as crossing among individuals and mutation [50, 51]. GA have been shown to obtain the optimum solution, if there is any, provided that elitism is introduced, meaning that the best individual at a given time is always maintained as part of the population. In this work we used a GA with elitism and 400 individuals in the population, meaning that up to 400 possible combinations of the parameters of the filter and other time-pickup parameters of the algorithm are considered and combined in a given population. Population evolved for at least 100 generations (meaning that about 40,000 new individuals were generated) and the best solution of the optimization process is taken from the best individual in the final population, once convergence is achieved, namely when the best individual has not been improved during the last 20 generations.

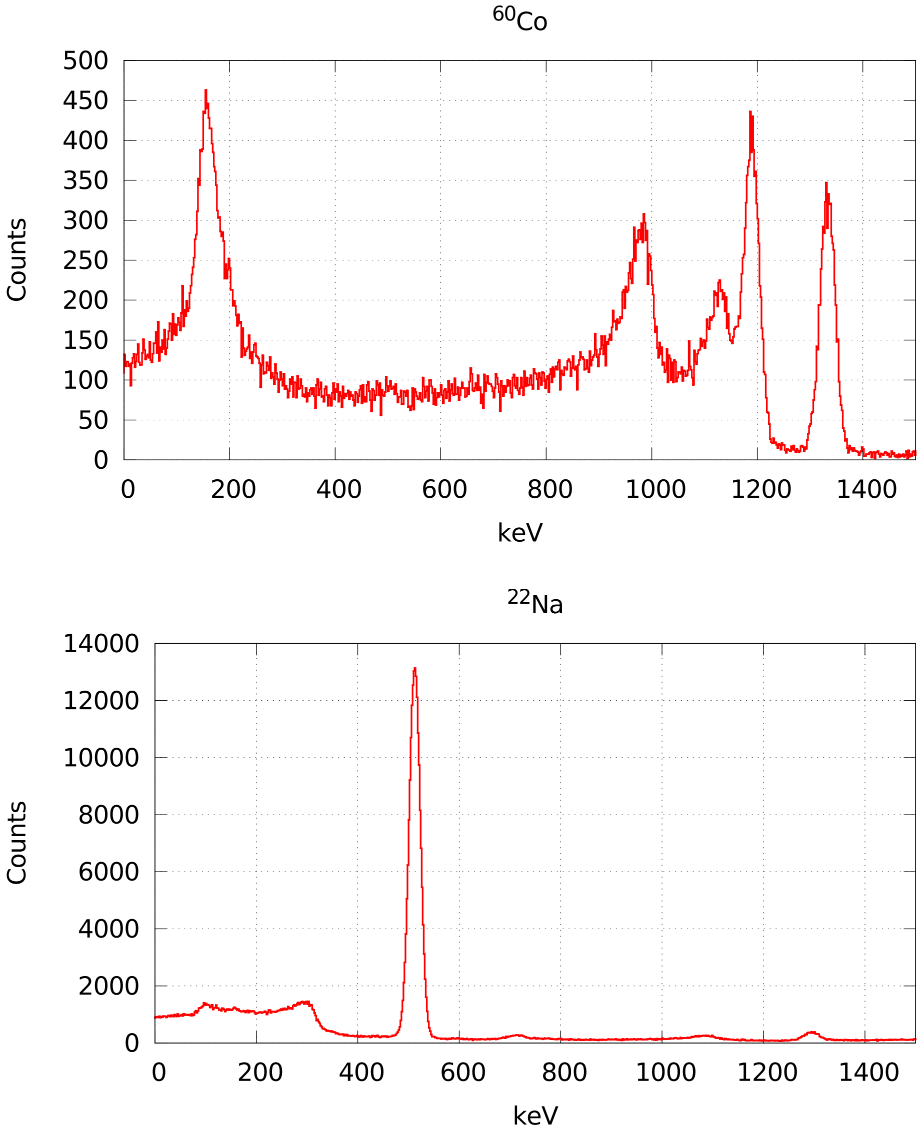

Figure 2.3: Example of energy spectrum for ^{60}Co (top) and ^{22}Na (bottom) obtained with composite Simpson's rule for charge integration. Because of the geometric distribution of the detectors, many backscatter events are inside the coincidence window and appear in the energy spectra.

2.2.5 Time Pick-up algorithms

The first logical approach to the design of time pickup algorithms was mimicking in the cpu, that is *in silico* the signal processing methods commonly applied in analog pulse processing [4]. The simplest of these conventional techniques is the Leading Edge Discriminator (LED), which is based upon obtaining time-stamp values from the crossing of the detector signal with a fixed threshold [52, 53].

The digital implementation of LED [54, 55, 56, 57, 58, 59] consisted in the selection of a fixed threshold and a linear interpolation of the samples that were just above and below the threshold, with the GA employed to choose the optimum value of the threshold. The weakness of this Digital Leading Edge Discriminator (DLED) is the same as for its analog version, namely the time walk. In the analog world, time walk is reduced by the use of CFDs[18], which is easily implemented in the fully digital form. This digital CFD (DCFD) [60, 61, 62, 63, 64] works as in the analog CFD: the digitized pulse is inverted, attenuated and added to a copy of the original pulse, which had been delayed. Time stamps for each pulse were determined with a linear interpolation of the signal zero crossing point of the DCFD shaped pulse. The parameters optimized by the GA in this case were the delay and the attenuation factor. The *in-silico* version of the algorithm had the advantage that the choice of delay and attenuation parameters is not restricted to the values available in the hardware-only CFD. This fact combined with the use of deep learning by means of the GA allowed us to outperform the time resolution of the conventional setup.

As a further step we developed a signal processing algorithm that could not be easily (or at all) implemented with analog systems, and with the potential of providing better results. The simplest idea may be a variation of the D-LED, where the upper level that the signal must cross was not an absolute threshold, but a percentage relative to the maximum of each peak. The time-stamp condition became thus a Relative Digital Leading Edge Discriminator (RDLED).

One problem with this algorithm is that it can receive additional noise contribution stemming from the estimation of the maximum value of the peak from the same noisy data. The presence of jitter or noise in the maximum may lead to oscillation in the chosen threshold. In order to avoid this, instead of determining the maximum just by taking the highest point, we used a second order polynomial to fit around the maximum a certain set of points of the pulse. Like the DLED case, the relative thresholds were optimized using the GA. One of the advantages of this algorithm is the substantial reduction of the time walk, that is, distinct time response at different energy values.

Although the time walk contribution is reduced with this method, it exhibits a worse time resolution than the DCFD. Thus, to improve the time resolution while keeping the absence of time walk, we have developed a signal filtering strategy aimed towards making the slope of the rising edge of the pulse as steep as possible. These techniques are commonly used in the conventional analog shaping analysis, where a differentiator (CR) filter is used [4]. This kind of analog filters can be easily reproduced *in silico* with simple algorithms. Eq. 2.1 and 2.2 show a digital simulation of CR and RC circuits respectively. In our digital analysis we implemented the

CR circuit before applying the RDLED, adding the RC time constant τ to the list of parameters to be optimized by the GA.

$$y[n] = \left(1 + \frac{1}{\tau}\right) y[n-1] + x[n] - x[n-1] \tag{2.1}$$

$$y[n] = \left(1 + \frac{1}{\tau}\right) y[n-1] + \frac{1}{\tau} x[n-1] \tag{2.2}$$

The idea of using optimal digital filters to shape the pulses before obtaining the time stamps with RDLED was explored even further by looking for the family of recursive filters (2.3) that provides the best timing performance.

$$y[n] = Ay[n-1] + Bx[n] + Cx[n-1] \tag{2.3}$$

A, B, and C are parameters optimized by the GA alongside with the threshold values. This general recursive filter contains any RC and CR circuit combinations as particular cases, but it is way more general than those. The pulses shaped with the GA-optimized version of the filter seemed at first very similar to the unfiltered ones. However, a closer inspection of the rise time reveals a much higher slope for the digitally shaped pulses 2.4. The increased slope contributes to the reduction of time jitter effects introduced by noise at the threshold crossing. This method provided the best results as it is shown in the next section.

2.2.6 Time walk correction

Although the algorithms presented in this work reduce the time walk with respect to the simplest DLED algorithm, there remains a residual dependence on the energy of the pulse. Taking advantage of the fact that our algorithms can provide simultaneous time and energy information, one can correct for this dependence. If we plot the difference in energy deposited in each detector against the coincidence time between detectors, we can observe a correlation of these two quantities. This is shown in fig. 5. We can easily correct for most of this time walk simply using a linear fit and removing the bulk of this dependence, improving significantly the CRT, especially in some cases where the time walk is larger, as it is the case of the DLED algorithm. For this algorithm, we can reduce the CRT by about 20% after correcting for the time walk.

2.3 Results

We compared the algorithms applying them to the same set of raw data. For the ^{60}Co source, 1.44 million pulses were acquired. Out of these, 40,000 pulses were inside the FEP gate selection.

For the ^{22}Na source, 600,000 pulses were acquired and 100,000 of them were inside the energy gate. In figure 2.6, time spectra obtained with the different algorithms and for each source are shown. In table 2.1, the time resolution (Coincidence resolution time FWHM) for the different algorithms is given. The values of CRT were calculated using a Gaussian fit to the time spectra shown in figures 2.6 and 2.7. Reduced chi-squared values are included in both tables like goodness of fit parameter, with a p-value of the chi-squared greater than 0.05 of statistical significance for all the cases. In order to evaluate the uncertainty of the time resolution, we divided each acquisition in two randomly chosen subsets and calculated the CRT again for each subset. This process was repeated 100 times in order to obtain 200 estimations of the FWHM and finally we provided our error for the Gaussian fit like the standard deviation in the 200 FWHM values calculated. These results are compared with those obtained with the traditional acquisition setup [34]. From this table we see that even without energy-time walk correction we can obtain comparable performance to the traditional analog signal processing. The introduction of a flexible filter optimized by means of a GA combined with the RDLED algorithm resulted in the best CRT of all cases, outperforming the analog counterpart. With FWHMs of 140 and 194 ps for the ^{60}Co and ^{22}Na cases, these results improve by more than 10% the resolution obtained with the conventional setup based on analog CFD and conventional TAC modules, and yield individual time resolutions of 99 and 137 ps FWHM at ^{60}Co and ^{22}Na energies. The DCFD algorithm, and the RDLED algorithm combined with a less general CR filter (eq. 2.1) exhibited similar results with a FWHM of 148 and 149 ps for ^{60}Co and 208 and 210 ps for ^{22}Na, respectively. A study of the good behavior of the linear interpolation in the calculation of the zero crossing stamps for the DCFD is implemented too. For this purpose we compared a cubic spline interpolation with 20 ps step size with the one of 200 ps step size employed throughout this work. We did not find significant differences between the FWHM values computed with both interpolations, so we can conclude that the 200 ps step size chosen coupled to linear interpolation for the DCFD algorithm is as good as it can get. The improvement with regards to the conventional setup was smaller in these two algorithms, but still significant. RDLED without any filtering showed worse resolution than the previous algorithms, with a CRT FWHM of 162 ps for ^{60}Co and 222 ps for ^{22}Na. The results with the DLED algorithm were the worst for the ^{60}Co case with a CRT FWHM of 199 ps, due to a larger time walk in the algorithm. When applied to the ^{22}Na case, where there is just one energy peak, time walk was less important. Even this simple algorithm achieved a resolution similar to the obtained with RDLED algorithm, with a CRT FWHM of 220 ps.

As explained in the previous section, the time walk dependence can be accounted for with a simple linear fit. As expected, the time walk was larger for the DLED algorithms. For the other algorithms the time walk was very similar and relatively small, less than 5 ps. Apart from the simple DLED algorithm that exhibits an obvious time walk, for the other algorithms the time walk has to do with the dependence on the noise of the time derived with them. The analysis of the time walk identifies a linear correction which removes most of it. Figure 2.7 and table 2.2 show the same results than figure 2.6 and table 2.1, but after time walk correction.

A marginal improvement for the ^{60}Co results showed up after the time walk correction for all the algorithms except for the DLED one where, as expected, the improvement was as high as 20%.

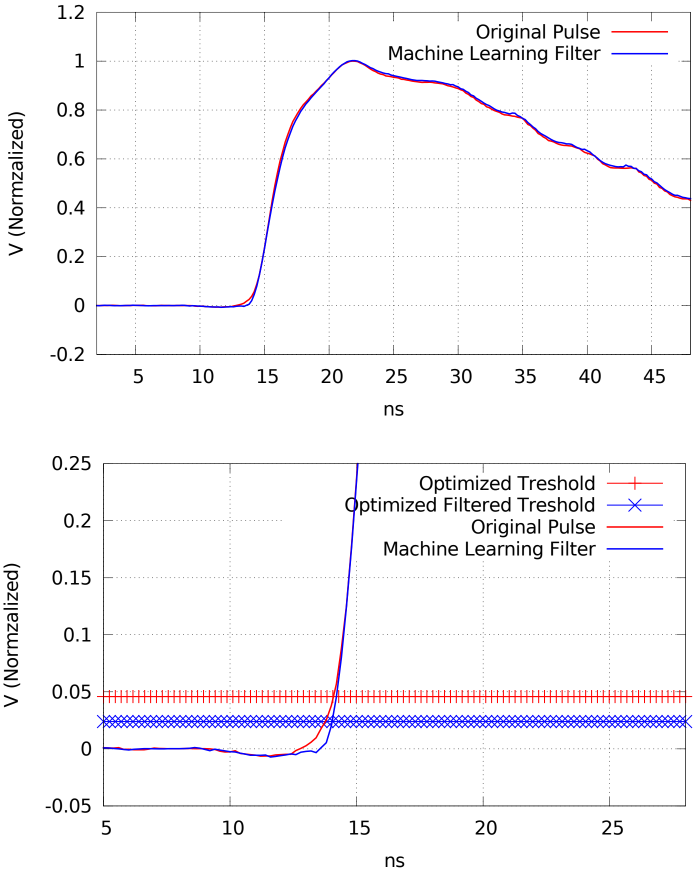

Figure 2.4: In the top part of this figure it is shown a normalized pulse for the ^{60}Co source compared with the same pulse after the general filter optimized by the GA. The effect of the filter is better seen after zooming out in the "first photon zone" shown in the bottom part. One can see that after filtering, the slope at the threshold of the pulse is larger, and that the optimal threshold found by the GA is in this area, just above the first photon zone.

For the other algorithms the improvement is just a few percent. For instance we could reach a CRT FWHM of 136 ps at ^{60}Co for the general filter plus the RDLED algorithm, improving by 12% the result of the conventional acquisition setup reference [34], and giving a FWHM time resolution per detector of only 96 ps.

2.3.1 Linearity of the general filter

When introducing an ad-hoc filter of the pulses one must make sure that no time-compression effects are introduced, which would distort the time measurements and time coincidence performance parameters. To verify that the filter preserves the time content of the signal, we generated pulses derived from the real ones, but with an artificial delay in one of the two time signals of the coincidence pair, and repeated the analysis on this derived sample. The

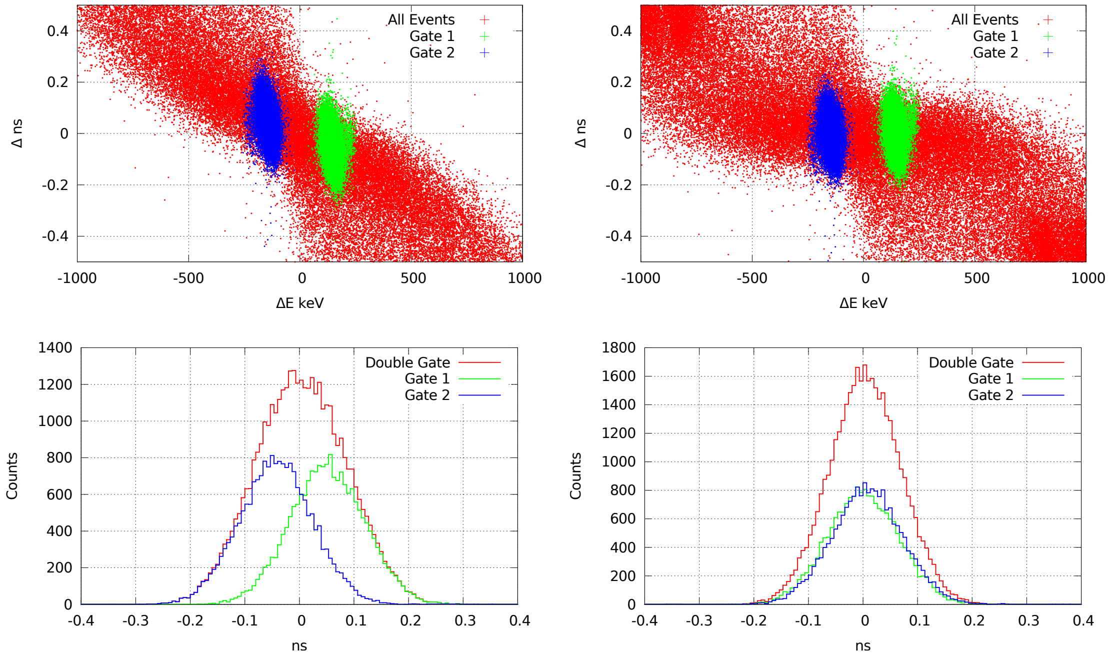

Figure 2.5: Example of energy walk for the DLED case using a ^{60}Co source, in the top-left figure the difference of deposited energy in each detector is compared to the coincidence time. Gate 1 is selected so the 1173 γ is deposited in detector number 1 and the 1333 γ in detector 2. Gate 2 is the reverse configuration. This way is easy to appreciate the correlation between the energy and the time distribution. In the top-right figure the same plot is displayed but after a linear correction for time walk applied. In the lower-left and lower-right panels the coincidence time spectra with and without this linear energy-walk correction are shown. The double gate is independent of which γ reach each detector.

artificial delay was randomly chosen as a number of delayed samples. Plotting the artificial delay introduced against the time difference measured should produce a 1:1 linear relationship. In figure 2.8 this relation is plotted.

For the ^{60}Co source, indeed we find a clear linear distribution. The number of pulses that appeared off the diagonal represented less than 0.5 % of the total of pulses and resulted from pile-up and random coincidence events that the delay in one of the branches of the time pair identifies. On the other hand, for the ^{22}Na source, the time differences for the delay pulses showed a larger spread outside the ‘correct’ diagonal, with a 2% of the total events off it. This is due to the contribution from Compton events coming from the 1.275 MeV gamma-ray of ^{22}Na. This contribution could not be removed just by the energy gate as we use only two detectors, and resulted in an effectively larger time coincidence window for true coincidences, and thus more random coincidences. The number of events off the diagonal matches the Compton background events that appear in the energy spectrum when an energy gate in the 511 keV peak is selected. Notice that this method of adding random delays on one line and re-verifying the time obtained by the algorithm is not only useful to test that the time-signal is not being tampered by the filter,

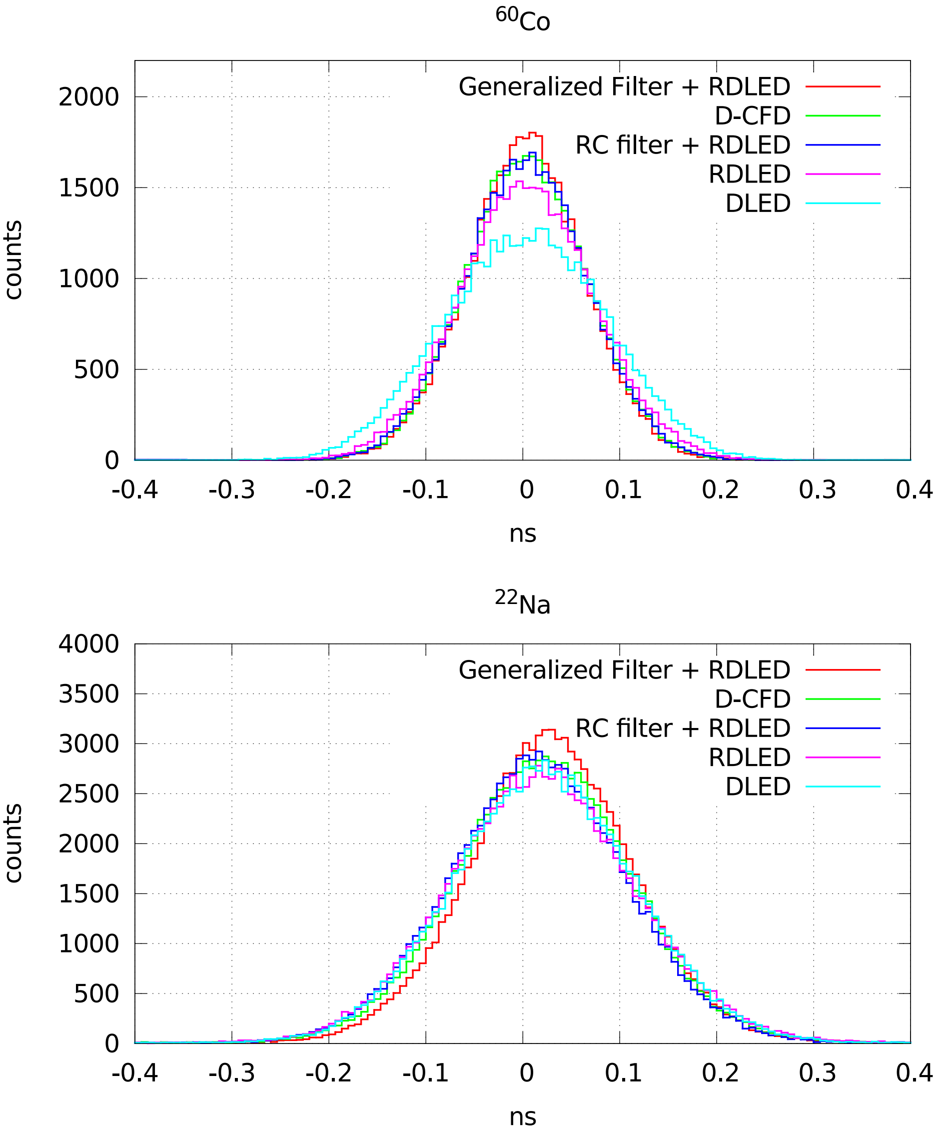

Figure 2.6: Time spectra for the different algorithms introduced in this work, the top figure for ^{60}Co and the bottom figure for ^{22}Na. In both cases, it is seen than the best resolution was obtained with the combination of a quite general filter whose parameters had been calculated with the GA, combined with a RDLED algorithm, with thresholds calculated with the same GA

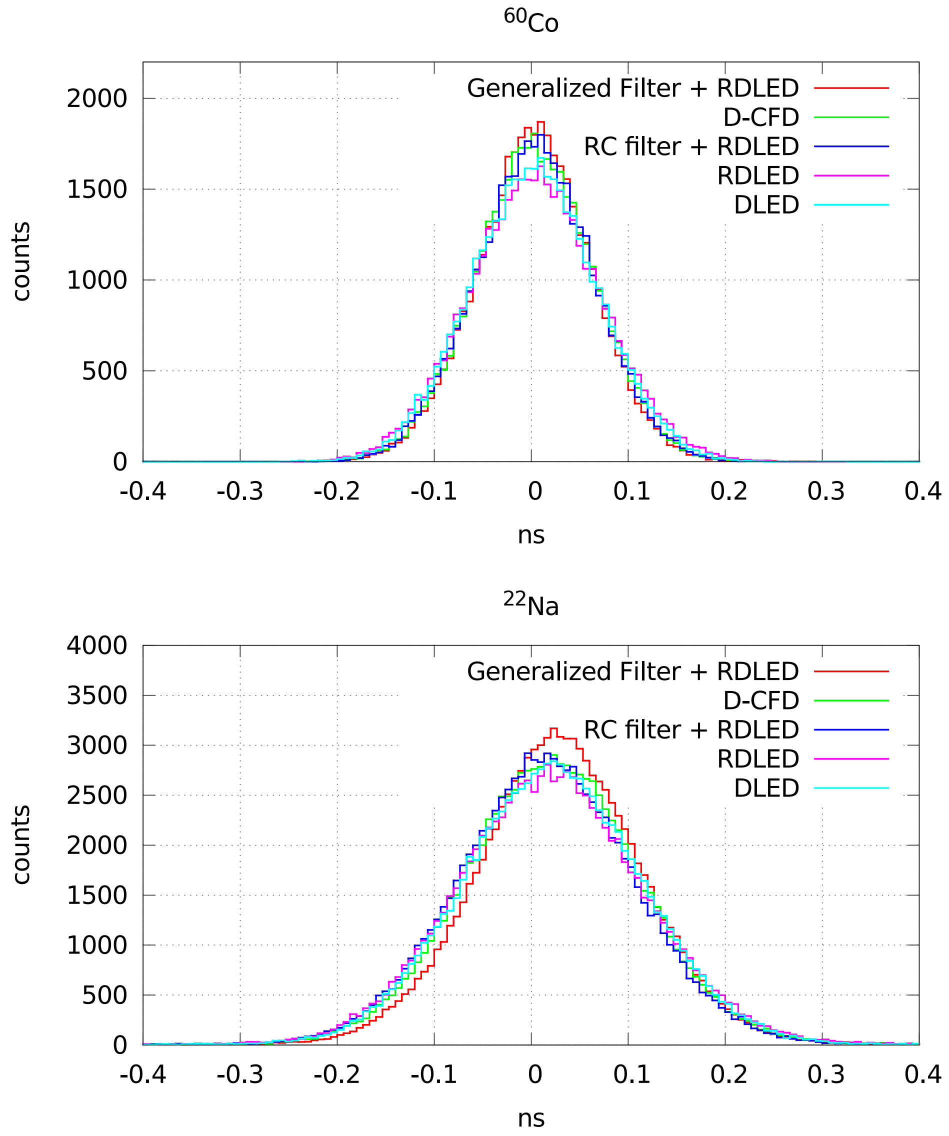

Figure 2.7: Time spectra for the different algorithms studied in this work after linear time walk correction, the top figure for ^{60}Co and the bottom figure for ^{22}Na. The best resolution was again obtained with the combination of a more general filter and the RDLED algorithm. The main visible difference with respect to figure 2.6 is the improvement in the DLED results for ^{60}Co

Algorithm	^{22}**Na**	χ^2/**p-Value**	^{60}Co	χ^2/**p-Value**
CFD + TAC[4]	226 ± 4 ps	-	156 ± 4 ps	-
DLED	220 ± 1 ps	1.32/0.07	199 ± 1 ps	1.34/0.07
RDLED	222 ± 1 ps	1.33/0.07	163 ± 1 ps	0.65/0.96
CR filter + RDLED	210 ± 1 ps	1.11/0.28	149 ± 1 ps	0.96/0.55
DCFD	208 ± 1 ps	0.93/0.6	148 ± 1 ps	0.75/0.9
General filter + RDLED	194 ± 1 ps	1.74/0.05	140 ± 1 ps	1.2/0.21

Table 2.1: Results of CRT as FWHM, in ps, for the different algorithms introduced in this work compared to the ones obtained with the traditional setup with essentially the same detectors and sources [34]. The error given is derived from the fit of a Gaussian to the CRT spectra. No time walk correction was applied to the results in this table.

Algorithm	^{22}Na	χ^2/**p-Value**	^{60}Co	χ^2/**p-Value**
CFD + TAC[4]	226 ± 4 ps	-	156 ± 4 ps	-
DLED	216 ± 1 ps	0.84/0.77	154 ± 1 ps	1.16/0.22
RDLED	222 ± 1 ps	1.21/0.15	159 ± 1 ps	1.04/0.4
CR filter + RDLED	210 ± 1 ps	1.13/0.25	143 ± 1 ps	0.8/0.83
DCFD	208 ± 1 ps	0.95/0.57	143 ± 1 ps	1.01/0.45
General filter + RDLED	194 ± 1 ps	1.17/0.2	136 ± 1 ps	1.21/0.2

Table 2.2: Results of time resolution giving as CRT FWHM (ps) for the different algorithms studied in this work after removing the linear part of the time walk

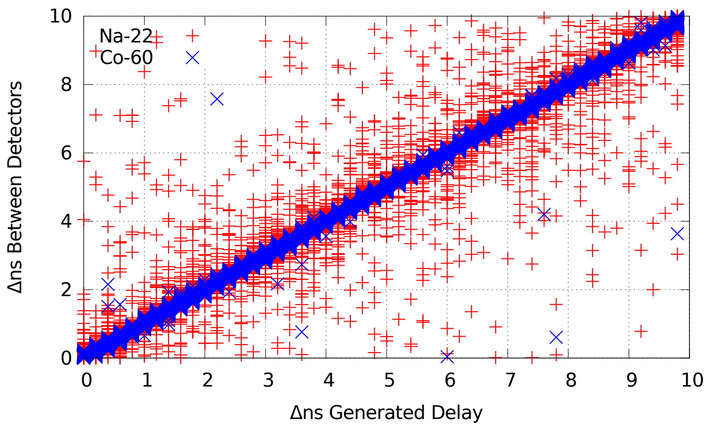

Figure 2.8: Linear correlation between the time differences calculated by the filter and the delay artificially generated by us. The correlation is 1:1 is seen clearly for ^{60}Co, as expected. The larger dispersion that appears in the case of ^{22}Na is due to Compton events that came from the 1275 keV gamma-ray.

but it will also identify pulses which suffered pile-up or belong to random coincidences.

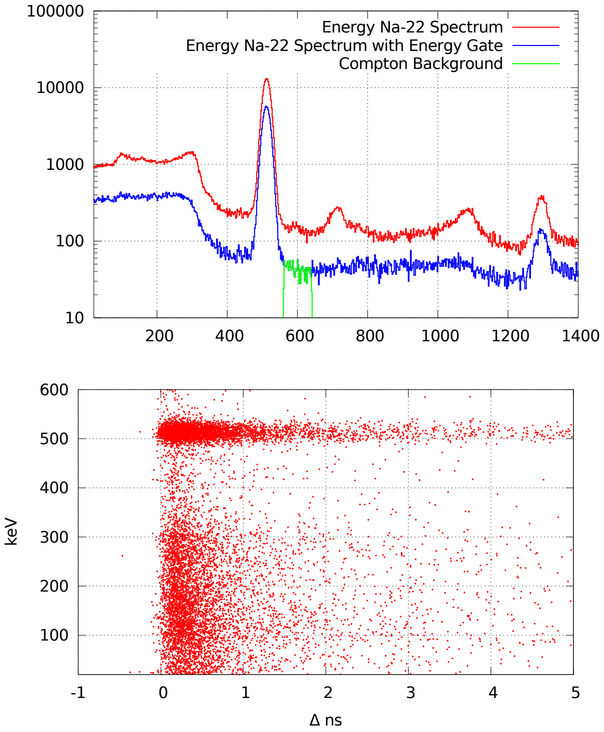

Figure 2.9: Top figure shows the spectrum of single events in one of $LaBr_3(Ce)$ detectors (red) for the ^{22}Na source, and the same spectra after selecting an energy gate of 511 keV in the other $LaBr_3(Ce)$ (blue). A Compton background appears due to the 1.275 MeV gamma-ray from ^{22}Na. A section in the background (green) with the same energy width than the FEP is selected to compare the contributions of Compton events to the 511-keV FEP. These events represent the 5% of the total counts in the photopeak. The bottom figure shows the time differences for the ^{22}Na source when an energy gate is selected in the 1275 keV peak with respect to the energy in the other detector. The time distribution around the 511 keV peak matches the number of events outside the diagonal in fig. 2.8

.

2.4 Summary and conclusions

High speed pulse digital sampling together with the use of advanced algorithms for signal processing represent a major breakthrough when fully digital acquisition systems are used for the read out of radiation detectors. The arrival time (time-stamp) of the incoming photons as well as the time resolution of a system can be determined through an off-line analysis of the pulse employing complex algorithms. This digital procedure has proven to perform equally well or even better than highly optimized analogue equivalent systems [31, 32, 33, 34] and has the advantage of lacking physical constrains, being the flexibility of the software the unique limitation. However, digital algorithms depend on many parameters with multiple possibilities, and manual iterative optimization becomes unfeasible. To address this inconvenience and finding optimal parameter settings, we have used machine learning strategies through a Genetic Algorithm (GA) to tune the multiple combinations of parameters, obtaining outstanding timing values, which are better than the best values quoted to date using analogue electronics [34].

In this work, we focused in optimizing the CRT between two $LaBr_3$(Ce) detectors that were read out by a DDAQ through the use of an *in silico* digital filter and digital pick up algorithms previously optimized by machine learning techniques. Measured values are compared with the numbers provided by the *in silico* digital filter with the most performing parameters set by hand. Results show that the timing performance provided by the GA strategy was better by 10%.

In this study, we have optimized the dependent parameter of three different types of time pick-up algorithms and we have studied the influences of the application of RC filters. The measured values of CRT are comparable to the best values quoted to date with analogue electronics [34]. Among all algorithms, the one corresponding to a general filter plus relative leading edge discriminator (RDLED) provides an excellent CRT value of 140 ps, at ^{60}Co energies and 194 ps at ^{22}Na (511 keV), being 10% better than the 156 ps at ^{60}Co and 226 ps at ^{22}Na (511 keV) of the analogue system.

Our study also proves the positive effect of implementing RC filter in the algorithms as well as the time walk corrections, where the use of the same pulse as the carrier of the energy and time information results in a great advantage. The main result from our study is that the use of machine learning strategies for the optimization of the algorithms relevant parameters provide excellent CRT results. We did not consider here algorithms for which the time signal and the energy signal are processed in a different way. For instance in [54] the time signal is amplified much more than the energy one and the time threshold is set just above the noise level, in this way trying to minimize the time walk. We propose that all the processing can be simply made *in silico*, with the flexibility of using any kind of filter and process over our signal without the necessity of a complex analog processing system. This fact combined whit the use of our GA as a guide to find the optimal filters and parameters make the measurements obtained with digital fast timing techniques competitive with the ones obtained with analog systems. Future implementation of these techniques requires the translation of our system to an on-line mode. With our current system it is still complicated to obtain a good acquisition speed (more than 1 GS/s) without dead time. But, on the other hand, some other references focused on interpolating strategies in order to obtain results with relatively low sampling rate [41]. The use of our GA for the search of the optimum filter parameters combined with these interpolating strategies could represent a possible way to obtain the best time and energy resolutions without the necessity of high sampling speed, simplifying the electronic and with a reasonable acquisition speed. This will ease a future implantation of on-line digital DAQs that keep the good resolution obtained in this work.

Chapter 3

Test of Genetic Algorithms for Time Measurements with New Detector Systems

3.1 Introduction

In the previous chapter we have shown how the use of digital filtering can be used to match, and even improve, the results that analog system can achieve. The employed DDAQ is not only useful as proof of concept of the potential of digital processing, but also it has applications in the characterization of new setups.

There are two factors to be taken into account in the design and improvement of new scintillation detectors. The first one is the selected crystal, and its characteristics. There are various scintillation properties to consider when we search for an ideal crystal[4]. Higher photon yield brings about a greater number of emitted photons and this implies better statistics in the photon detection, and thus an improvement in the energy resolution. In principle, the light energy conversion should be linear, therefore the photon yield should be proportional to the energy deposited in the crystal in a range as wide as possible. Other important characteristic is the scintillation decay time constant. Developing faster crystals is essential in order to enhance the intrinsic time resolution of the detectors and reduce the intrinsic detector dead time.

The second factor is the photosensor used in the measurement. It is important to select the light sensor with a good matching to the crystal light emission and with sufficient quantum efficiency in order to maximize the light collection. State-of-the-art of light sensors rely on the shift from convectional PMTs to novel SiPMs. Their compact size, their almost complete insensitivity to magnetic fields and their low working voltage, combined with their continuously decreasing prices make them perfect substitutes for traditional PMTs. Despite this fact, there is still ample room for improving the development of SiPM-based detectors. Increasing their effective area, something crucial for the read out of large monolithic crystals, and the improvement of the timing resolution are still hot topics in their design.

In this chapter we will illustrate how the DDAQ proposed in the previous chapter can be used as a reliable test tool for new detector systems. Taking into account the two factors mentioned above, we will show on one hand how the DDAQ was used to test a new, promising scintillator crystal [26], recently available on the market. On the other hand, the application to a read-out system using SiPMs [27] will be discussed. The aim is to convey the versatility of our DDAQ, and to underline its advantages as a compact and user-friendly test system. We will show one more example of the powerful potential of the use of digital filters combined with a genetic algorithm (GA).

3.2 Evaluation of a $\mathrm{LaBr_3(Ce+Sr)}$ detector

It has already been proven that there are several possible modifications in $\mathrm{LaBr_3(Ce)}$ crystals that may enhance their performance, both in terms of energy resolution, but also related to time response. While increasing the amount of Ce doping can improve the time resolution [65], the crystal size and its shape are important to optimize the response. An analysis of the influence of both factors is given in [33, 34].

Ionic co-doping with 0.5% Sr has been shown to increase the $\mathrm{LaBr_3(Ce)}$ light yield [66] while keeping the same light emission spectrum, peaking at around 380 nm. In this section we will focus on the use of our DDAQ to evaluate a new $\mathrm{LaBr_3(Ce+Sr)}$ crystal produced and made commercially available by Saint-Gobain Crystals under the trademark BrilLanCe390S [67]. While the energy resolution has been previously investigated, the effect of the slightly shifted light emission and the presence of the ionic co-dopant on the time response has not been addressed before. Therefore, we will study the possible advantages of this new crystal by comparing it with a standard $\mathrm{LaBr_3(Ce)}$ crystal. In order to avoid any geometrical and light collection consideration, the co-doped and the reference crystals are selected of the same size and shape. Both crystals are cylinders 3.8 cm in height and 3.8 cm in diameter, encapsulated in a aluminium housing with a thin entrance window of 0.5 mm and with a glass light guide to couple it to the photosensor. A PMT by Hamamatsu, model R9779 (MOD4) in assembly H10570 is chosen. The PMT was operated at 1350 V for both tested crystals. The dynode outputs were digitized using the DRS4 evaluation board and processed for time and energy measurements.

3.2.1 Pulse shape comparison

For the $\mathrm{LaBr_3(Ce+Sr)}$ crystal an increase in the photon yield compared to $\mathrm{LaBr_3(Ce)}$ from 70 000 photons/MeV to 77 000 photons/MeV has been reported [68]. In spite of this fact, the mechanisms of photon emission are generally slower in the co-doped scintillator than in the Ce-only crystal. In [68] three decay time constants of 18 ns (78%), 82 ns and 2500 ns are reported, versus 16 ns for $\mathrm{LaBr_3(Ce)}$. Our DDAQ is the perfect tool to study the shape of the crystal output pulses. It should be mentioned that, owing to the transit time spread of only 250 ps, the contribution of the response of the R9779 photomultiplier can be neglected at this stage. For this purpose, we have recorded 40000 pulses for 511-keV photopeak from a ^{22}Na source with each crystal in order to analyze the differences in pulse shapes. We have selected the 511-keV energy, applied an averaging procedure, and computed the 10%–90% rise time for both detectors. The results are τ_{rise}= 6 ns for the $\mathrm{LaBr_3(Ce+Sr)}$ crystal, compared to τ_{rise}= 5 ns for the $\mathrm{LaBr_3(Ce)}$, an increase of 1 ns compared to the standard, non co-doped, scintillator. Fig. 3.1 illustrates the pulse shapes as digitized from the PMT outputs. The slower rise and decay times of the $\mathrm{LaBr_3(Ce+Sr)}$ crystal can be readily observed.

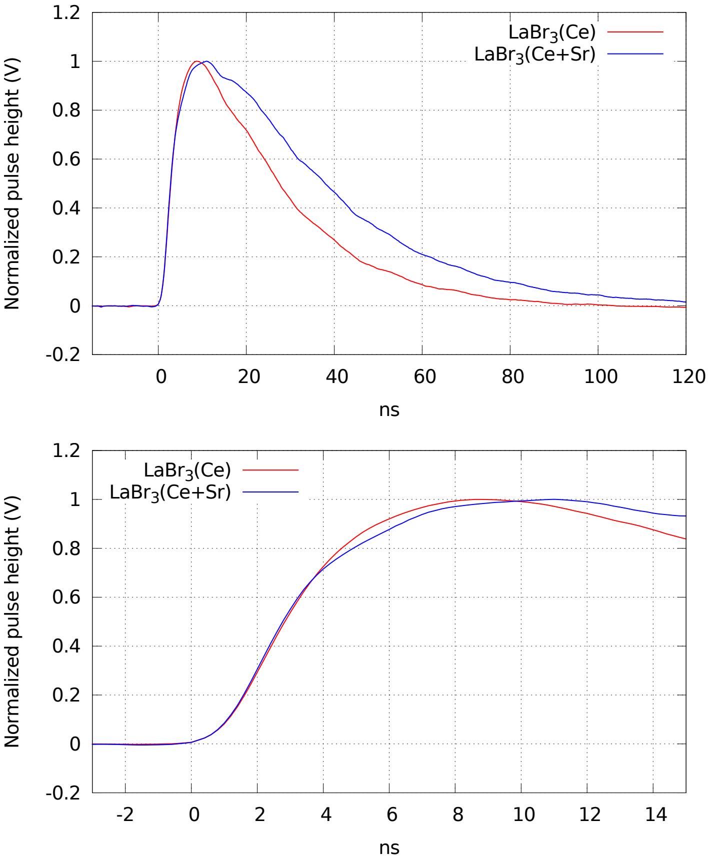

Figure 3.1: Dynode signals from the R9779 PMT for the $\mathrm{LaBr_3(Ce)}$ (red) and $\mathrm{LaBr_3(Ce+Sr)}$ (blue) crystals under evaluation. The signals shown are obtained by the average of 1000 pulses selected on the 511-kev photopeak. They are aligned and normalized by height before calculating the average samples. The top picture shows the pulse shape for the two combinations, while the bottom picture presents a zoom into the rise time region. It easy to observe the slower time constants in the co-doped crystal.

3.2.2 Energy resolution

After examining the pulse shapes for both types of crystals, which provide the initial input of the processing parameters, the energy resolution has been investigated. For the energy measurements

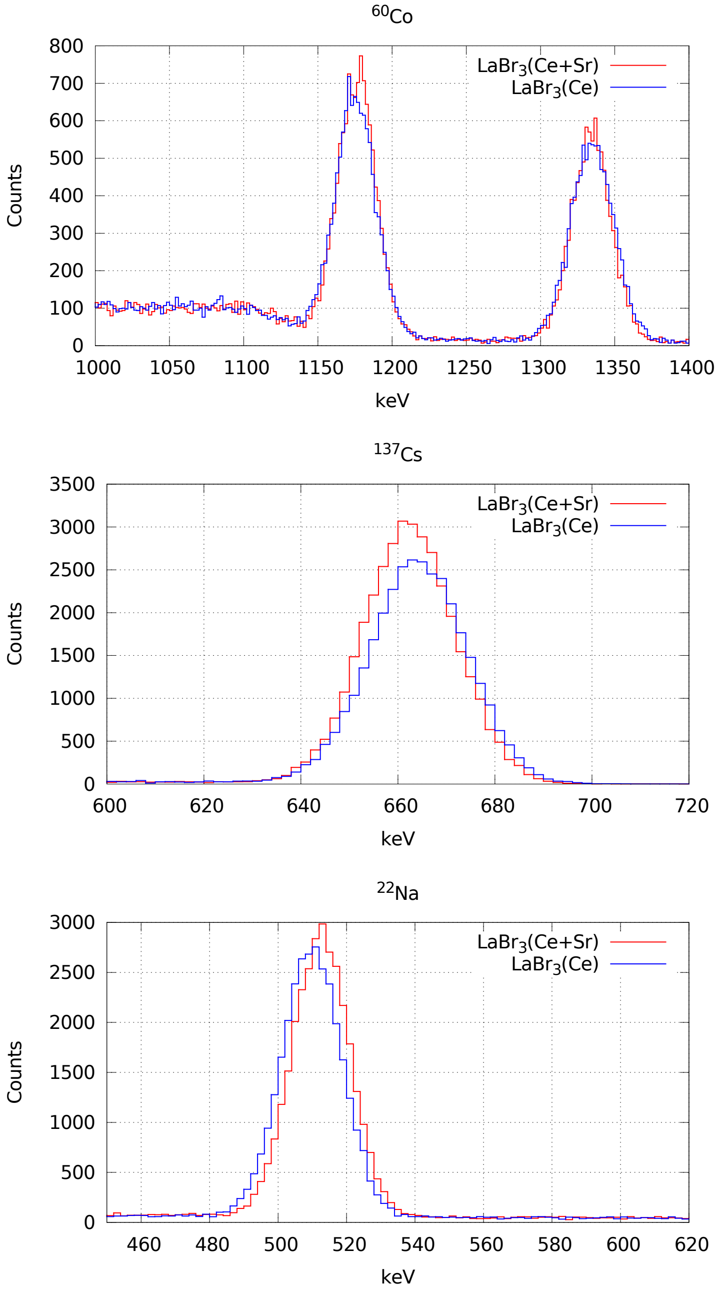

Figure 3.2: Comparison of the energy resolution of the $LaBr_3(Ce)$ and $LaBr_3(Ce + Sr)$ crystals coupled to a R9779 PMT for different radioactive sources

the sample speed selected was 1 Gs/s, enough to record the full pulse and to have a sufficiently long signal baseline. We evaluate the energy resolution of the $\mathrm{LaBr_3(Ce+Sr)}$ crystal coupled to the Hamamatsu R9779 PMT by examining the full-energy γ peaks from ^{137}Cs, ^{22}Na and ^{60}Co sources, in comparison to the $\mathrm{LaBr_3(Ce)}$ crystal. The baseline is subtracted and the energy is calculated as the integral of the pulse using the Simpson's method for numerical integration. The results are plotted in Fig. 3.2 and shown in Table 3.1 for both detectors. The increase in the photon yield arising from the 0.5% Sr2+ ionic co-doping translates into a slight improvement of the energy resolution from 3.5% to 3.3% FWHM for the 622-keV full-energy peak.

Energy (keV)	$\mathrm{LaBr_3(Ce+Sr)}$	$\mathrm{LaBr_3(Ce)}$
511	3.8%	4.0%
662	3.3%	3.5%
1332	2.3%	2.6%

Table 3.1: Comparison of the full-energy peak FWHM resolution of both crystals using different radioactive sources.

3.2.3 Time resolution

Next the time resolution of the new crystal is quantified. The expectation is that, according to subsection 3.2.1, the time response should be fast, but slightly slower that the non co-doped crystal. The time response of both the $\mathrm{LaBr_3(Ce+Sr)}$ and $\mathrm{LaBr_3(Ce)}$ cylindrical crystals was characterized by coincidence measurements against a reference detector, consisting on a $\mathrm{LaBr_3(Ce)}$ crystal with the shape of a truncated cone coupled to a fast PMT, like the one used in Chapter 2.

The time characterization was carried out at both ^{60}Co and ^{22}Na (511 keV) energies. Timing data were obtained from the time stamps processed off-line using an energy gating condition for the full-energy peaks of interest. The time stamp values are obtained with the leading edge filter with variable threshold computed as a percentage of the maximum of the pulse, which was optimized independently for both crystals using the genetic algorithm (GA) discussed in Chapter 2. The $\mathrm{LaBr_3(Ce+Sr)}$ and $\mathrm{LaBr_3(Ce)}$ individual time resolutions are extracted by de-convoluting the reference $\mathrm{LaBr_3(Ce)}$ contribution of 110±2ps at ^{60}Co energies and 158±2 ps at 511 keV (^{22}Na). The results are provided in Table 3.2. The values given refer to the individual FWHM time resolutions after de-convolution.

Crystal	^{60}Co	^{22}Na
$\mathrm{LaBr_3(Ce)}$	142 ± 3 ps	207 ± 3 ps
$\mathrm{LaBr_3(Ce+Sr)}$	170 ± 3 ps	252 ± 3 ps

Table 3.2: De-convoluted time resolutions for both monolithic large-size crystals.

The time difference spectra are depicted in Fig. 3.3 for the 1173.2 + 1332.5 keV ^{60}Co combination and for 511-keV photons from ^{22}Na. It is apparent that the time resolution for the co-doped $\mathrm{LaBr_3(Ce+Sr)}$ crystal is 20% worse than the one from the identical $\mathrm{LaBr_3(Ce)}$ under the

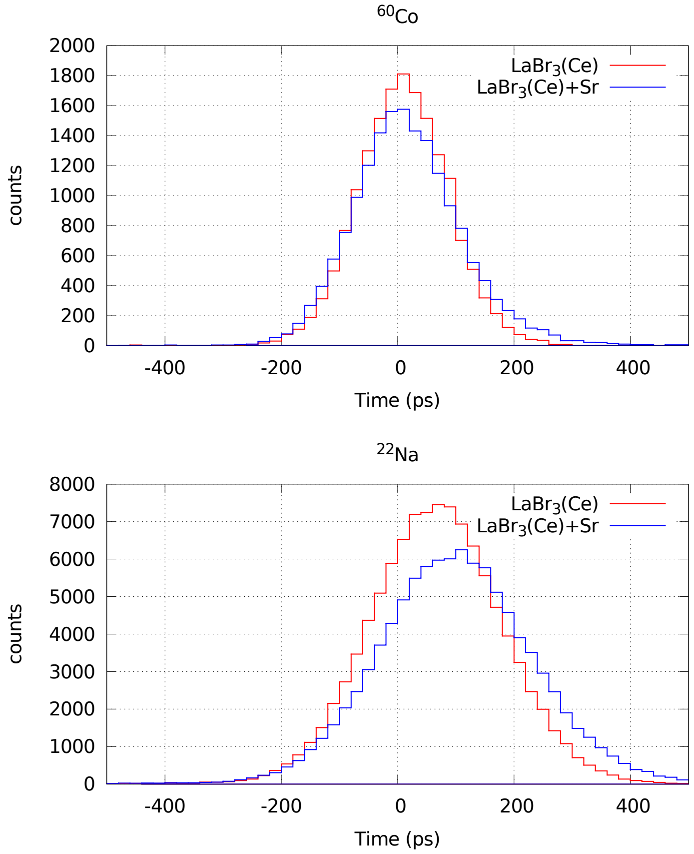

Figure 3.3: Time difference spectra overlapped for $\mathrm{LaBr_3(Ce + Sr)}$ and $\mathrm{LaBr_3(Ce)}$ cylindrical crystals.

same conditions. The decrease of time resolution of the $\mathrm{LaBr_3(Ce)}$ crystal with respect to the reference detector is only due to the different geometries. The shape and size of reference detector has been optimized in order to enhance its time response, at the expense of its energy resolution [34]. Something similar could be happening in our case of study, where in spite of the slight improvement (5%) in energy resolution, the $\mathrm{LaBr_3(Ce + Sr)}$ crystal shows a slowed down time distribution of the photons emitted by the crystal, leading to a deterioration of the time resolution.

We can have a better insight into the deterioration of the time resolution of the $\mathrm{LaBr_3(Ce + Sr)}$ by studying the effect of the filters, and comparing it to the non co-doped crystal. The filter calculated by the GA for the case without co-doping is pretty similar to the one calculated in the previous chapter for the reference detector. The GA filter keeps the shape of the signal practically identical to the original shape, but increases the slope of the rising edge of the pulse. In Fig. 3.4 an average of the pulses after and before the implementation of the filter is shown. On the contrary, for the $\mathrm{LaBr_3(Ce + Sr)}$ the GA found a different solution. In this case the shape of the pulse is pretty invariant, like in $\mathrm{LaBr_3(Ce)}$, but here with slight changes. The filter does

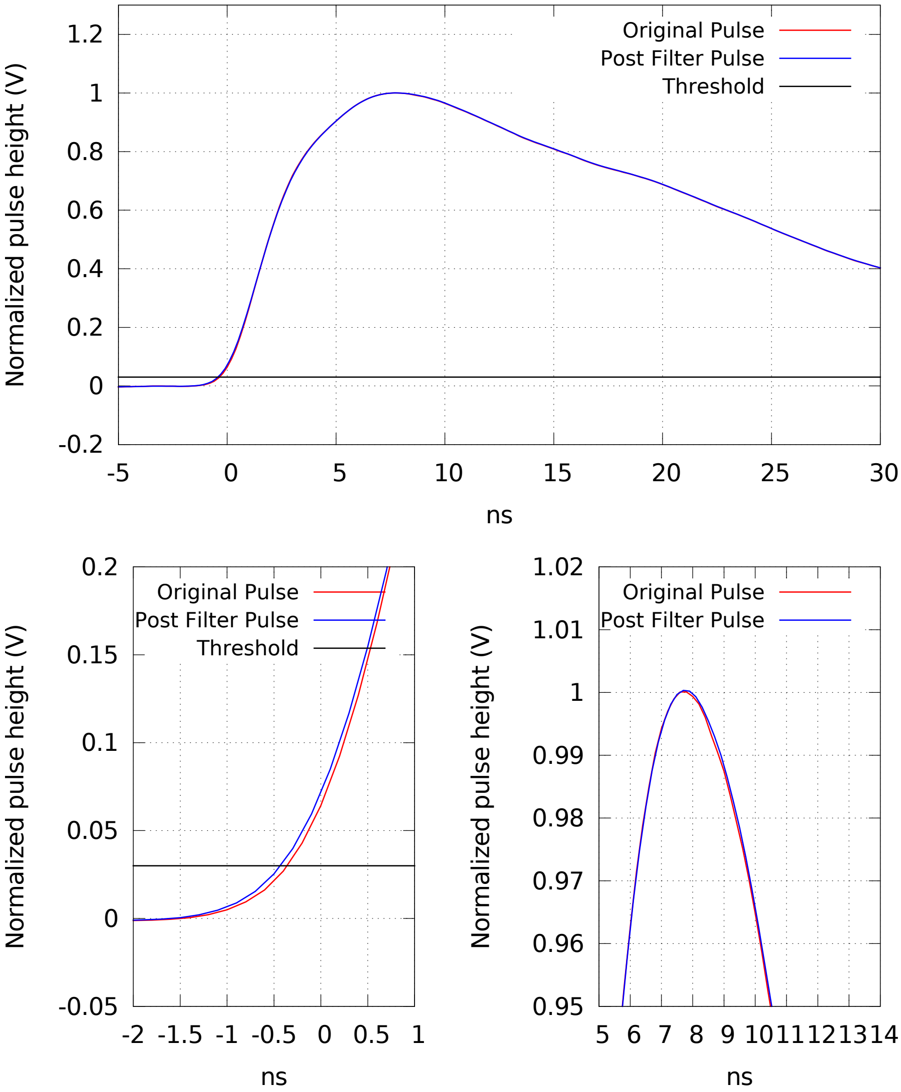

Figure 3.4: Comparison of the effect the GA filter for the LaBr$_3$(Ce) crystal. The two plotted signals are the average of 1000 normalized pulses selected on a 511-keV energy window, after and before the filter. Special attention should be directed to the pulse rising edge, where the filter effect is most notorious.

not only affect the slope, but also tries to stabilize the maximum of the pulse. We are using a RDLED in order to calculate the timestamp values; this implies that if the fit of the maximum is not sufficiently precise there will be uncertainties in the relative threshold. Because of this, the GA prioritizes that the maximum be as stable as possible before obtaining a sharper slope in pulse rising edge. In Fig. 3.5 the effect of this filter is shown.

The deterioration of the time resolution amounts to just above 30%, and it is also observed for the ^{60}Co full-energy peaks, which reinforces the notion that the algorithm is robust with respect

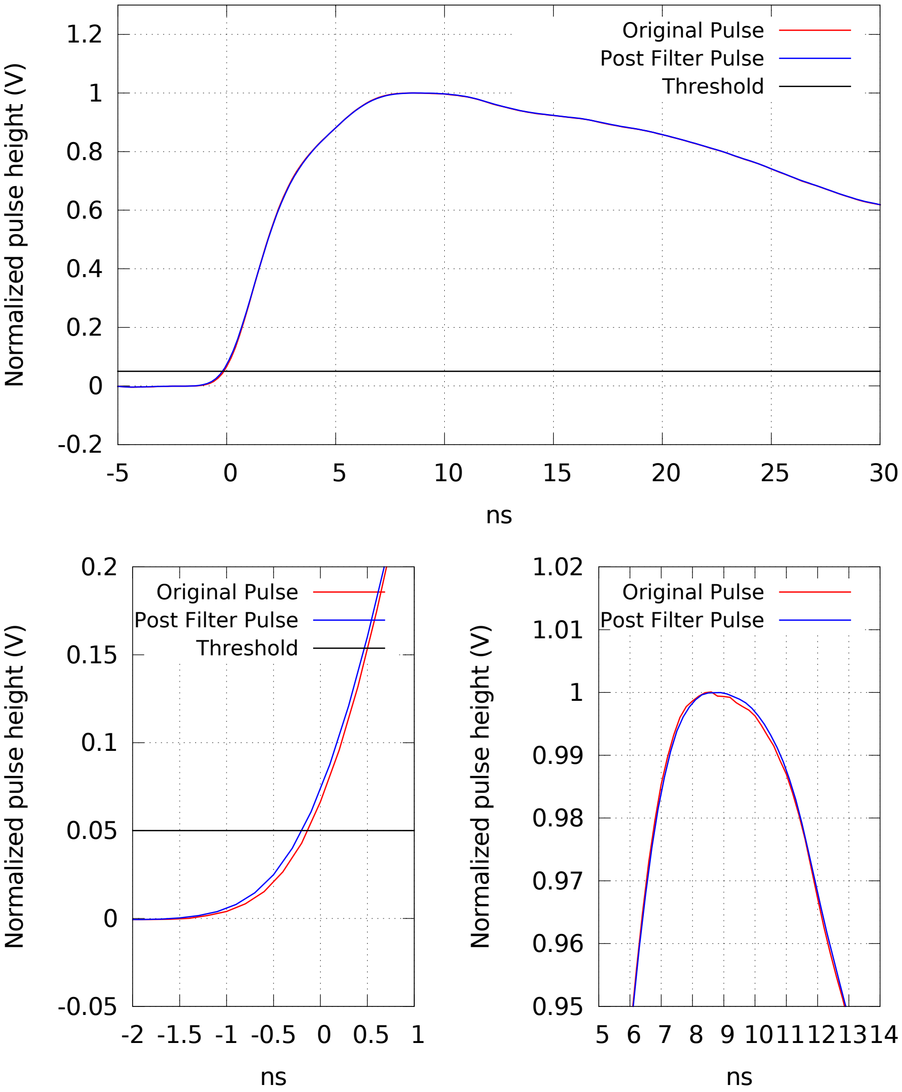

Figure 3.5: Comparison of the effect of the GA filter, similar to Fig. 3.4, but for $\mathrm{LaBr_3(Ce+Sr)}$. In this case it is important to note how the filter stabilizes the region around the maximum, making it more constant, and thus reducing the fit uncertainty.

to the signal amplitude, but also points out to the intrinsic nature of the worse time resolution of the $\mathrm{LaBr_3(Ce+Sr)}$ crystal.

3.3 Evaluation of the PA3325-WB-0808 SiPM matrix

The second illustration of the versatility of the DDAQ using a genetic algorithm deals with fast scintillators coupled to a SiPM matrix. In recent years SiPMs are on their way to replace

PMTs. The multiple qualities that endorse this change have already been discussed in Chapter 1. Nonetheless these detectors have limitations too, one of then it is their small size. Normally, the largest size provided by manufacturers for a single SiPM it is not larger than 1×1 cm^2. This is due to high parasitic capacitance of the SiPM cells. SiPMs with a bigger size have a larger number of cells that have to be read in parallel, so the parasitic capacitance of the SiPM increases drastically [69]. This high capacitance acts like a low-pass filter, producing slower pulses and hampering a fast discharge. The limited size is a special obstacle when we need to study large monolithic crystal, since a large active are that minimizes light collection losses is necessary. A possible solution to this problem is the use of a matrix of several SiPMs that can cover the whole crystal surface.

In this work we are going to test the possibilities offered by one of such matrices. The matrix used is model PA3325-WB-0808 by Ketek. It consists of 16 individual SiPM pixels read in parallel, whose principal characteristics can be found in Table 3.3. It is important to note that the parasitic capacitance of the individual SiPMs have to been taken into account when we read the matrix signal too. There are different approaches to read out SiPM arrays, but for our tests we are going to focus on the simplest way to do it. It consists on making a passive sum of the signals coming from each SiPM. Being this method the simplest one, it is relevant to mention that it is the most affected one by the parasitic capacitance of each pixel. Other, more complex, approaches include reading each matrix pixel individually or dividing the matrix in smaller groups that are passively summed, and later summed again in one signal using wide-band amplifiers [70]. These will not be analyzed in this work.

The solution that we use to confront the challenge of the low-pass filter effect produced by the coupling of parasitic capacitance is the same principle used in [54, 71] to read out digital signals of individual SiPMs. The approach consists in two stages. First, the supply voltage of the SiPM is increased until the signal is almost saturated. Afterwards, the signal is taken through a gain amplifier, saturating our digitizers. By this procedure the contribution of the first optical photons is amplified, which are the ones that carry most of the timing information. This method takes advantage of the bit resolution of the digitizer by only recording this part of the signal. The simplest way to obtain this information is by a DLED whose threshold is implemented in the first part of the amplified signal, only a few mV higher than the electronic noise.

Our idea is going one step further than previously by using our genetic algorithm to calculate the threshold, and also by searching for a general filter to process the amplified signal.

Photon Detection Peak	**Breakdown Voltage**	**Active area of each Pixel**	**Matrix Size**
450 nm	24.7 V	3 x 3 mm^2	26.84 x 26.84 x 5.21 mm^2

Table 3.3: Main characteristics of the PA3325-WB-0808 matrix

3.3.1 Experimental Setup

Our setup consists of two $LaBr_3$ cylinders of 2.5 cm in height and 2.5 cm in diameter, each of them coupled to a PA3325-WB-0808 matrix. There are multiple readout systems for large monolithic crystals using SiPMs matrices available in the literature [72, 73, 74]. All of them underline the importance of trying to minimize the contribution of the low-pass filter generated by the matrix capacitance. One option is reducing the intrinsic RC value of the filter. For this purpose we used a surface mount radio-frequency transformer TC4-11G2+ from Mini-Circuits [75] with a primary/secondary Ω ratio of 50/12.5. In this way we reduced the RC value while keeping a good impedance matching with the output wires. The coil output was divided in two different signals, one of them was directly connected to the DRS4 and was be used to obtain the energy information. The other signal was connected to a ZFL-500LN-BNC low-noise amplifier from Mini-Circuits [75] before the DRS4. The sampling rate selected in this case was 2 GS/s. We have reduced it with respect to the previous studied cases because of the limited memory of the DRS4, which is able to record only 1024 samples per pulse. If we had chosen a larger sampling rate, such as 5 GS/s, we would have reduced the acquisition window to 200 ns, which is not enough to record the whole decay component of the signal. In Fig. 3.6 a schematic view of the setup is presented. In Fig. 3.7 the matrix pulses after and before the amplification are shown.

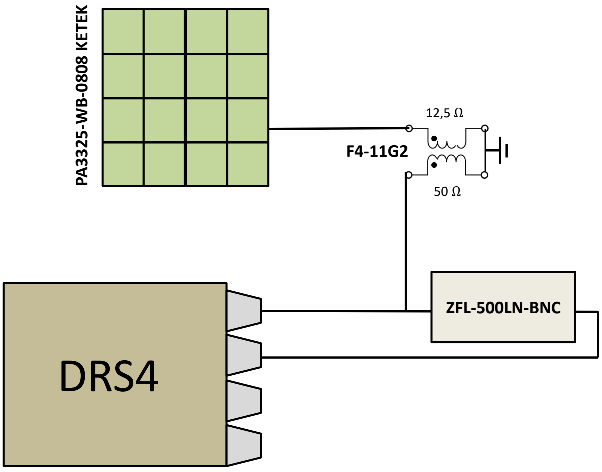

Figure 3.6: Sketch of the SiPM matrix connections.

3.3.2 Energy resolution

For the energy measurements the signal taken directly from the matrix is employed. Although we selected a sampling rate of 2 GS/s, the parasitic capacitance of the matrix made it impossible to record the whole decay component of the signals. A priori this could pose a problem to achieve a good energy resolution. But, considering that the long decay is only due to an electronic issue, the information of the $LaBr_3$(Ce) emission should still be contained in the pulse rise time,

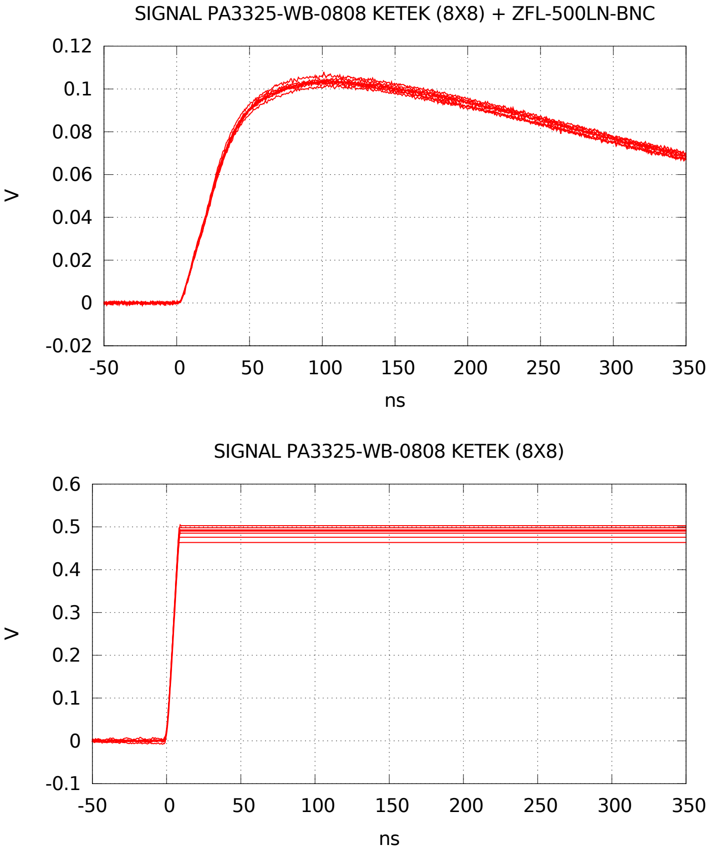

Figure 3.7: Pulse comparison of the SiPM matrix signal directly connected (top) and after the use of the ZFL-500LN-BNC amplifier (bottom).

and it should be enough to get sufficient energy resolution. Since the decay constant of the $LaBr_3(Ce)$ is much shorter than the RC component of the matrix, if we select a good integration window and the subtraction of the baseline is properly made, a good energy resolution should be obtained. We used a trapezoidal rule to obtain the energy, selecting again 200-ns-wide integration windows from the beginning of the pulses. Using these parameters we obtained a FHWM energy resolution of 2.8% at 1332 keV and 5.0% at 511 keV. These values are consistent with the expected ones obtained with a PMT as photosensor (like for example those discussed in section 2.2.3 or shown in Table 3.1). Using a similar crystal and a Hamamatsu R9779 fast PMT, FWHM energy resolutions of 2.4% at 1332 keV and 3.9% at 511 keV were reported in [33]. The procedure described here thus provides a satisfactory solution to maintain a good energy resolution, which is one of the main properties of $LaBr_3(Ce)$ crystals.

3.3.3 Time resolution

In Chapter 2 it is mentioned that the proposed filter is a generalization of CR and RC filters. As mentioned before, at least one of these two filters is a possible solution when the best filter

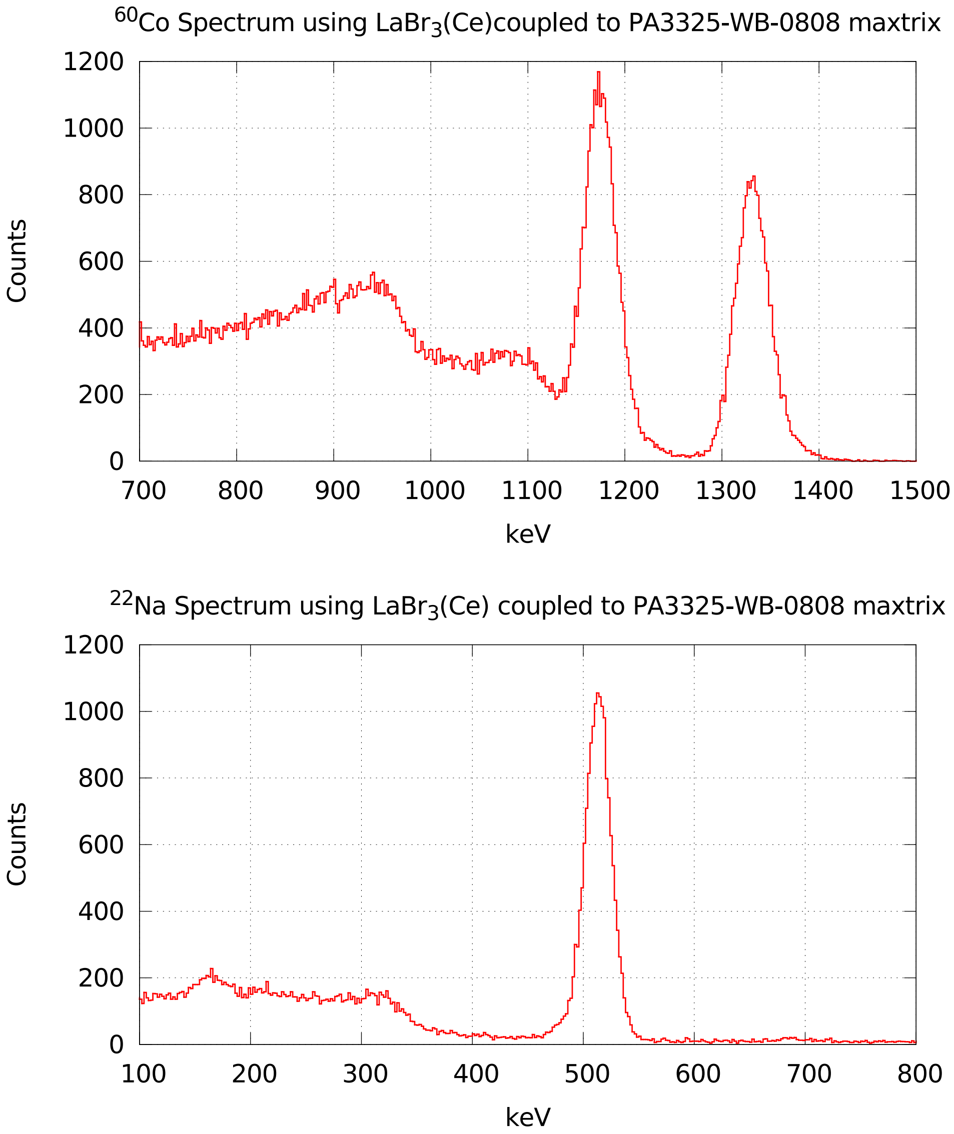
^{60}Co Spectrum using LaBr$_3$(Ce)coupled to PA3325-WB-0808 maxtrix

^{22}Na Spectrum using LaBr$_3$(Ce) coupled to PA3325-WB-0808 maxtrix

Figure 3.8: Example of the energy spectra for ^{60}Co (above) and ^{22}Na (below) obtained by integrating the rise time of the PA3325-WB-0808 matrix pulses.

is searched. This was actually the case for the best solution that the GA could find. Because of that, the GA selected the equivalent of a high-pass filter with cutoff frequency of 200 MHz. The purpose of this filter was to make the slope as sharp as possible. This is combined with the absolute threshold that the GA found. As expected, the threshold is located very close to the first-photon height, just above the noise signal in the baseline. The effect of the filter and the calculated threshold are shown in the Fig. 3.10.

In Fig. 3.9 it is shown the time spectra obtained with the DLED combined with the filter calculated by the GA, for ^{22}Na and ^{60}Co sources. Both spectra are measured after selecting the gates corresponding to the FEPs. In Table 3.4 the FWHM for the CRT of each source is shown.

An important aspect to take into account it that in this case we are using a DLED and this implies that the absolute threshold is completely independent of the shape of the pulse. This causes that the contribution of the time walk can be larger than expected. Following the procedures explained in Chapter 2 we can study this effect. If we plot the difference of the energy deposited on each detector and we compare it to the time difference, we find that there is a clear dependence with respect to the energy. This dependence is shown in Fig. 3.11.

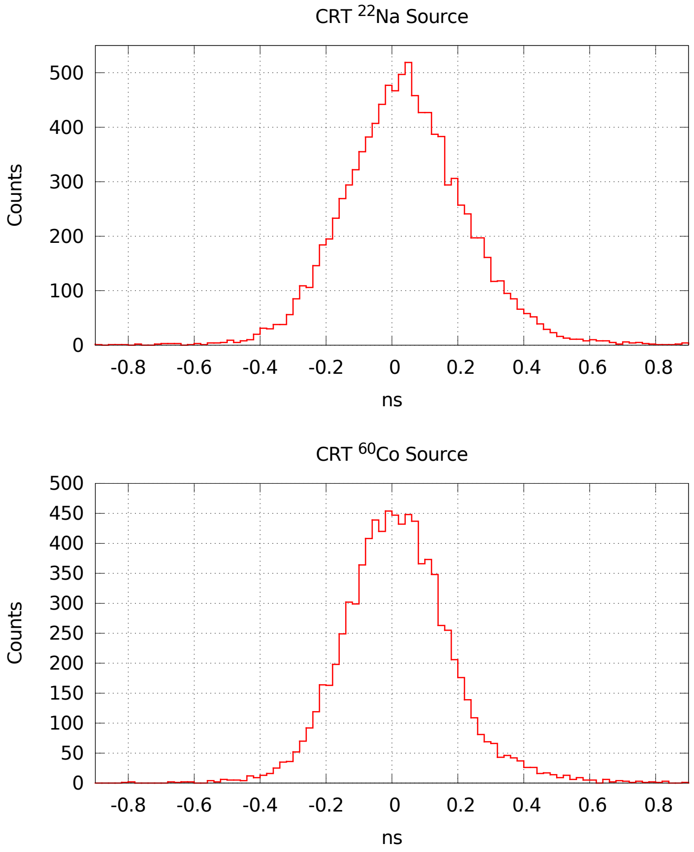

Figure 3.9: Time spectra for ^{22}Na (above) and ^{60}Co (below) sources using a LED algorithm combined with a high-pass filter to the matrix signal after amplification by the ZFL-500LN-BNC amplifier.

Although the results may not look optimal if we compare them to those obtained with the same detectors and a PMT, if we de-convolute the contribution of each detector (by assuming that they have equal response) we obtain individual FWHM time resolutions of 238(2) ps and 272(2) ps for ^{60}Co and ^{22}Na, respectively. These values do not match those obtained by fast PMTs,

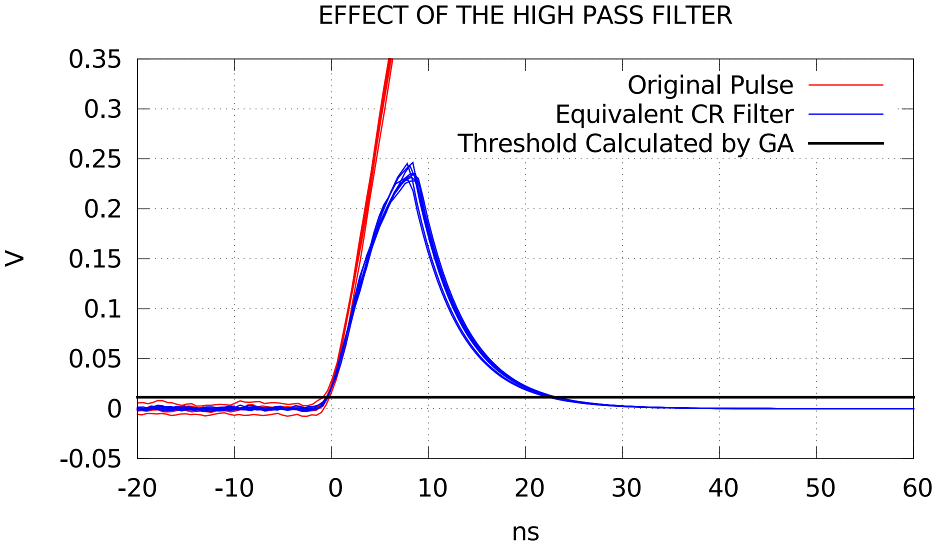

Figure 3.10: Comparison of the CR filter calculated by the genetic algorithm. The CR affects the amplifier signal and increases the slope at the beginning of the pulse, where the absolute threshold calculated by the GA is located.

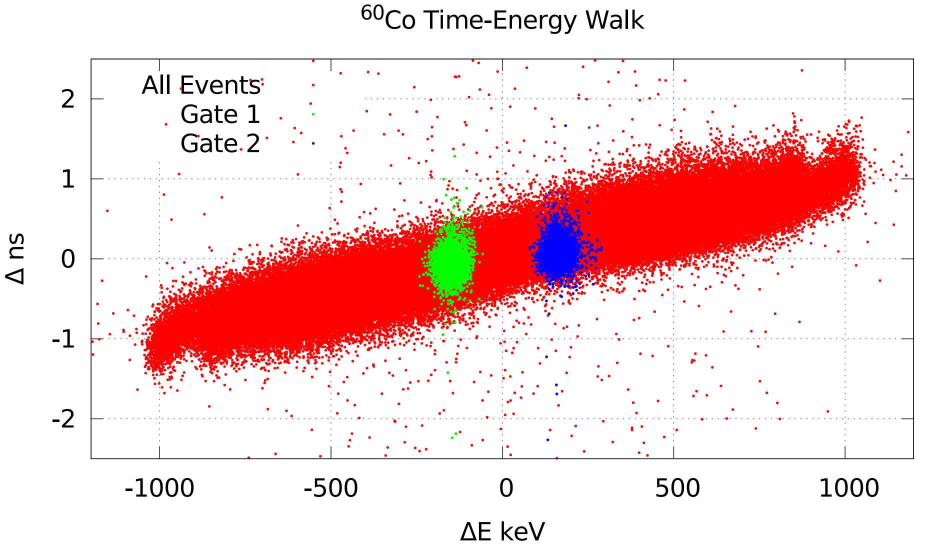

Figure 3.11: Example of time walk for the DLED case using a ^{60}Co source. The energy difference between the two coincident detectors is shown on the x-axis while the time difference is presented on the y-axis. Gate 1 is chosen so that the 1173-keV γ ray is detected in detector number 1 and the 1333-keV γ ray in detector 2. Gate 2 is the reverse configuration. The events without any gating condition are shown in red. The steep slope shows how the time walk is still notorious with the algorithm used.

^{60}Co	^{22}Na
337 ± 2 ps	385 ± 3 ps

Table 3.4: Coincidence resolution time given as the FWHM of the time spectra for the two $LaBr_3$(Ce) crystals coupled to the PA3325-WB-0808 matrix. By assuming equal time response individual FWHM time resolutions of 238(2) ps and 272(2) ps are obtained.

but are a good first approach. In the literature there are measurements of the time resolution of $LaBr_3$(Ce) monolithic crystals, such as those described in Ref. [76]. In that work the time measurements are based on a DLED, like in our case, and the individual resolution for ^{22}Na is 226 ps. But there are very substantial differences that explain a slightly worse time resolution in our results. To start with, the crystal in [76] has a volume of 16.2x18x10 mm^3, more than a factor 4 smaller that the one used by us. The sampling rate of the digitizer described in [76] is also higher, 8 GS/s, which provides an even better sampling of the signal. And, finally, the matrix only has 4 SiPMs, in comparison with our matrix with 16, which obviously reduces the sum of parasitic capacitance.

In this context the results that we obtain are very satisfactory. Nonetheless, there is ample room for improvement in our system. For example, new SiPMs developed by ON Semiconductor [77] provide a mechanism to minimize the effect of the parasitic contribution of the SiPM by the use of Schottky diodes between the individual pixels. Work on this direction is already ongoing in our group [78]. Future developments in electronics could also be combined with the use of a GA, but this work is beyond the scope of this thesis.

3.4 Conclusions of this chapter

The premise in Chapter 2 was to find a way to automatically optimize time-resolution measurements with a digital system for a well-defined case. In this chapter we have proved that the genetic algorithm could be a universal solution to find the best possible filter in other situations. We have illustrated the applicability of the GA to two different setups, a new kind of scintillator crystal made of $LaBr_3(Ce + Sr)$, and a PA3325-WB-0808 SiPM matrix used as photodetector coupled to a standard $LaBr_3$(Ce) crystal. In both cases a satisfactory time resolution using the GA could be achieved, and even if not fully competitive with other standard solutions, it shows the potential of GA.

In fact, in both cases the limiting factors can be tracked down to hardware issues. In the case of the co-doped crystal, the $LaBr_3(Ce + Sr)$ pulse was not stable enough compared to the $LaBr_3$(Ce) case. Anyways, the versatility of the GA is demonstrated by the solution found. Concerning the PA3325-WB-0808 SiPM matrix, we faced the challenges of a much larger crystal and matrix than previously reported. Still the GA was capable of reaching a very good result, maybe far from the optimal value that could be expected for a $LaBr_3$(Ce) crystal, but very competitive with respect to SiPMs coupled to medium-size monolithic crystals of this type. This hints towards a strong potential for the use of the genetic algorithm.

It is worth pointing out that, out of all the possible filters that could be found, the GA solution is mostly (but not quite just) a CR differentiation circuit, which would be one of the natural options we would try to make the pulses faster and to obtain a better timing with the conventional approach. Notice that the GA not only saves us the effort of figuring out the differentiation constant, but that also it introduces a bit of integration, not only differentiation, to reduce the noise. We have verified that a differential only circuit performs worse than the combination chosen by the GA.

Chapter 4

High Performance Digital Acquisition I: Design of a DDAQ for the Study of Prompt Gamma-Rays in Protontherapy

As we were arguing in te introduction, digital filters are becoming an indispensable tool in the development of compact, flexible, powerful DDAQ systems. The systems described in chapters 2 and 3 are examples of it. For the systems described so far we used a large digitizing speed and a high vertical resolution (16 bits), useful to assess the viability of DDAQ, the performance advantage with regards to analog shaping DAQ, and to identify possible improvements. But in nuclear data acquisition, beyond time and energy resolution, other parameters are of relevance. For instance, many experiments are very demanding in terms of the expected rates of events, as we may find in PET, nuclear fusion reactors or proton therapy. Besides using a very fast detector, able of sustaining rates of tens of millions of events per second without significant pulse pile-up, the electronics should also be able of coping with the rates and dealing with pulse pile-up. This would entail pulses of length <100 ns, and this combined with high rates, we would need to sample the signal at speeds which will overflow state-of-the-art USB ports. Our fast $LaBr_3$(Ce) or $CeBr_3$ detectors fall in this category of fast scintillators, as well as plastic scintillators do. As mentioned in the Introduction, there are several ways to cope with high rates. The first one is to avoid communicating with the computer as much as possible, doing the signal pulse processing in the digitizer, on the fly, during acquisition. This will require a smart digitizer with a FPGA, DSP, GPU or any sort of computing chip, in which our filters and algorithms could be implemented. Although the situation nowadays has improved a lot, programming FPGAs it is not a simple task and it requires a deep knowledge of digital electronics and quite some training, although some vendors provide predefined libraries for pulse processing which simplifies this task.

Another option is to couple the (relatively expensive) digitizer directly to the PC board using the high speed PCIe bus. This would allow the digitizing card to communicate directly to the CPU, GPU and on board memory, at speed transfers in excess of 8 GB/s.

In this chapter we resorted to downgrading the maximum data rate achievable for a given detector, stretching the pulses, so that we can sample the signal at a lower pace, allowing for the signal to be continuously sampled and sent to the computer in triggerless mode, where it can be recorded or analyzed on the fly. Data rate will be limited now by losses due to pile-up, or by the computer being unable of processing the pulses as they arrive. Downgrading the speed of the pulses may look as a poor solution, but it is inexpensive, and it will allow us to compare the computing burden of different algorithms and the event rate that a modern computer can handle. Furthermore, it is a simple solution which will allow us to verify the capability of DDAQ of dealing with pulse pile-up. Thus in the following chapters we are going to introduce three different DDAQs employed in actual experiments, as a proof of principle with good enough results, where we trade off high sampling rates and high vertical resolution for cost and simplicity, by resorting to very common USB digital scopes. In each one of the following chapters we will use a similar structure: a short background about the measurement, a description of the setup developed by us and finally a brief summary of the experimental results obtained. It should be pointed out that it is not the goal of this thesis to discuss in depth the data analysis and results for each of these experiments, but to study the viability, limitations and advantages of the inexpensive DDAQ systems proposed.

4.1 Theoretical Background: Proton Therapy

Proton therapy (PT) is a well-known radiotherapy technique with currently more than 90 facilities operating worldwide and more than 200.000 patients treated so far [79]. The technique uses proton beams for cancer treatment. Its main advantage is that the majority of the energy is deposited in a narrow and well-defined area at the end of the proton range, known as the Bragg peak. Most of the dose is deposited in a small region and it sharply falls to zero afterwards [80, 81]. This makes it possible to improve spatial dose conformity, reducing potential toxicities and damage to healthy tissues around the tumor, mostly in the distal zone of the tumor [82].

A well-defined dose deposition explains the huge potential of PT, but it can become a problem too. The sharp distal dose fall-off requires a precise knowledge of the proton range in tissues [83] as uncertainties in its determination can make dose delivery very inaccurate. Therefore, monitoring the edges of the proton dose is of paramount importance for the correct treatment planning of dose coverage of the tumor and protection of organs at risk.

In the last decades, several methods have been proposed to monitor proton range and control dose deposition within the patient (during or shortly after treatment) with submillimeter accuracy [83, 84, 85]. Most of these techniques are based on the indirect measurement of the proton range from the secondary radiation originated by nuclear reactions of protons in human tissues. They have been implemented either as PET (Positron Emission Tomography), which is based on the detection of the positron emitters activated in the tissue [86, 87], or as prompt-gamma (PG) imaging[88], when the detected secondary radiation consists of γ rays coming from very short-lived isotopes.

One possible way to increase this secondary radiation is the administration of external contrast agents, in the form of isotopes with a large proton capture cross section that produce a well-defined radiation field, in a volume close to the proton Bragg peak. The prompt emission of these contrast agents could be used to monitor the Bragg peak position and therefore the dose deposition. This is the main research envisaged by the PRONTO project [28], which focuses on the evaluation of possible contrast agents, studying their cross section and the radiation field they produce after proton activation. At present, two principal areas of work are identified in PRONTO: the first one consists in searching for possible contrast candidates, based in Monte Carlo simulations [89], and the other one focuses on experimental tests of these contrast agents, measuring their activation cross-sections [90].

4.2 Experimental Setup

4.2.1 Detector Selection

Our objective is to be able to experimentally measure activation cross sections of potential contrasts. When it comes to developing an experimental setup for this goal it is important to keep in mind that the highest level of γ-ray emissions is produced during and right after proton irradiation, that is, prompt radiation. The high rates involved made it necessary to design detectors that could handle a large number of counts without pile-up losses or energy resolution worsening. Good energy resolution is also essential in order to resolve the prompt gamma photopeaks. Many possible contrast agents that we wanted to assess were β^+ emitters, which could be also candidates for prompt and delayed PET range verification, so it is also important that our detector system could provide time-resolved coincidence events, with high rejection of random events, even at very high rates. Finally, we need our setup to provide us with instantaneous information about the experiment performance, in order to verify that the decay in the samples is what we expected, allowing to monitor beam position and intensity.

A detector system based on fast inorganic scintillator crystals, as the ones we use for fast timing nuclear measurements, suits our requirements. The high efficiency and fast response of the crystals reduce count losses and increase the statistics for the experiment. We already have shown the benefits of using digital acquisition with these detectors. Therefore we will implement again a fully digital strategy which allowed for a very compact and easy to deploy setup, flexible and inexpensive, that preserves the good energy resolution of the crystals.

The scintillators selected were $LaBr_3(Ce)$ crystals, for the first runs, and $CeBr_3$ for later measurements. We have chosen them because of their high photon yield (70 photons/keV), providing good energy resolution, and besides, fast decay constant (of the order of 20 ns), making them perfect to minimize dead time due to pile-up events. $CeBr_3$ crystals have the further advantage of exhibiting a very small internal activity, very useful to reduce background counts in order to measure very small activation cross-sections, with very long half-lives, or both.

Our measurement system consisted typically of four crystals coupled to fast PMTs of the R9779 type by Hamamatsu. Crystals had truncated cone geometry with a nominal height of 3.8 cm, and top and bottom bases with a total nominal length of 2.5 cm and 3.8 cm respectively. The crystals were specially designed for enhanced time response and packing fraction and they have already been tested with our digital DAQ. Each detector was kept in a fixed position at a distance of 4.5 cm measured from the detector end-cap to the center of the target to be irradiated by the proton beam. The detectors are at 30 degrees with respect to the plane perpendicular to the proton beam. Polylactic acid holders designed by us with a 3D printer were employed to keep the setup in place in between consecutive irradiations. A photo of the setup is shown in Fig. 4.1. We have shown that a DDAQ can provide excellent energy and timing resolution capabilities for this setup, better that the ones obtained with the analog conventional system [23].

4.2.2 DDAQ Selection

The DDAQ that we have developed is based on the digitization of the PMT signal with a digital oscilloscope (Picoscope 6403D) [91]. Oscilloscope specifications are shown in Table 4.1. We have selected this scope because of its simplicity to program and its versatile acquisition modes, making it a very flexible tool for different applications. In streaming mode it makes it possible to deploy an online acquisition system. Using multithreading in modern computers with more than one CPU/core, the signal is digitized in an internal memory buffer in the scope and continuously sent to the computer in triggerless mode. The signal received is processed *in silico* in the computer, identifying the pulses with a threshold condition (or any other trigger condition, for that purpose, including coincidences) and energy and time stamps. This information is continually recorded to disk in a list-mode file, including the identification of the detector that has triggered.

Data sheets Picoscope 6403D	
Bandwidth	350 MHz
Sampling Rate (Maximum for 1 channel activated)	5 MS/s
Maximum streaming data rate	Streaming to SSD hard drive 78 MS/s
Resolution	8 bits
Input Impedance	1 MΩ ± 1% 15 pF, or 50 Ω ± 2%

Table 4.1: Specifications of the digital scope employed in this chapter.

Most digital oscilloscopes include a variable gain amplifier stage which allows to match the height of the signals to the maximum voltage spanned by their ADCs, and they incorporate also low-pass filter to avoid aliasing in the signal due to frequency components exceeding the Nyquist limit.

Due to the fact that the digitized pulses are streamed to the computer, the maximum sampling

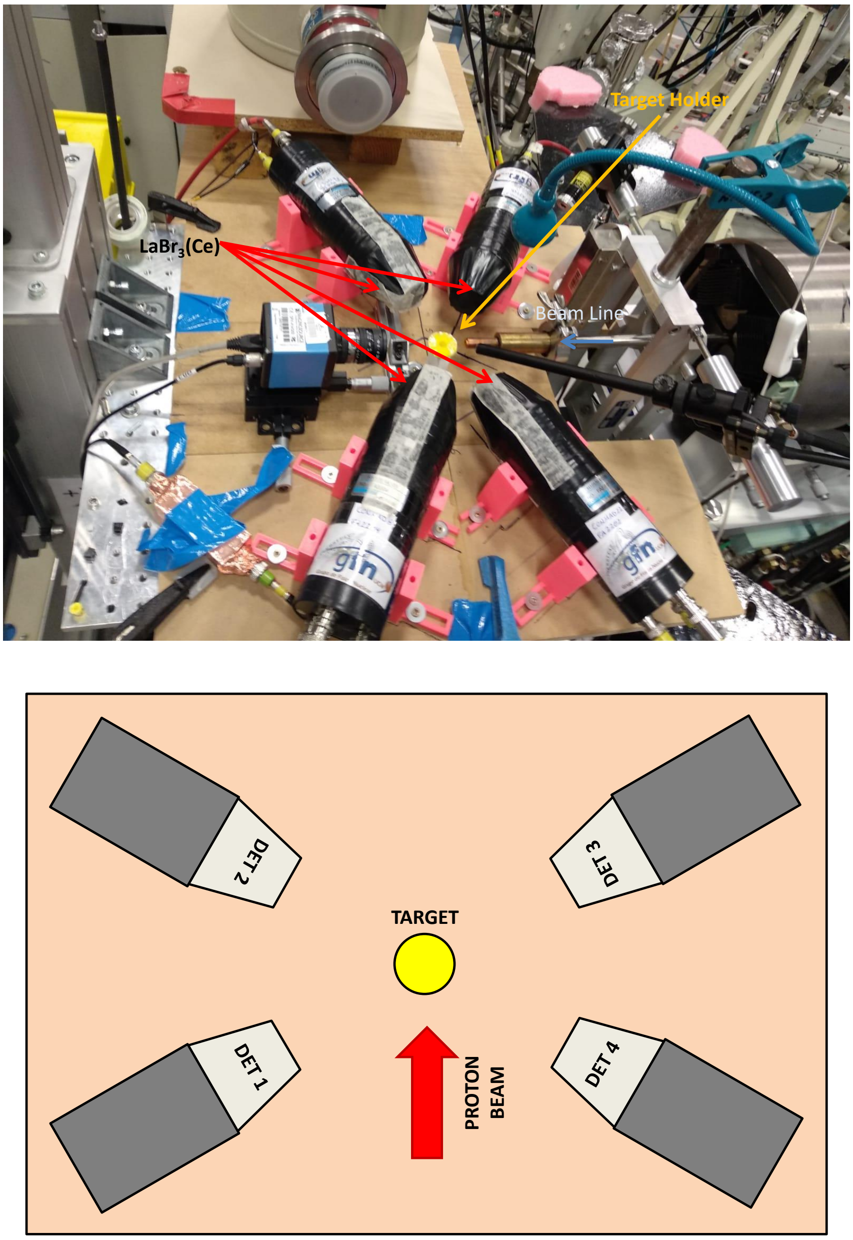

Figure 4.1: Setup used in this experiment. The four LaBr$_3$(Ce) are placed in such a way that each of them is on the same line in order to detect pair-annihilation events. The polylactic acid holder for the samples are located in the center between the four detectors. In the photography (top) one of the calibration sources used in this work is shown on top of the holder. It is in this location where the contrast candidate sample will be produced.

rate of the scope was limited by the USB transfer speed. This scope model can use USB3.0 ports, so theoretically we could obtain data transfer of the order of 150 MS/s without losses (one sample every 26 ns with the 4 channels active). This maximum transfer speed can be further limited at the PC end, and thus will depend on how powerful the computer is. We made tests with a pulse generator FY2200SP by FeelTech to assess the actual maximum rate of our system when processing pulses in the notebooks we intended to use. We sent trains of pulses with a frequency of 1 MHz and counted the number of them that our system processed without losses, for different sampling rates. Doing this, we determined that the maximum possible rate was 64 ns between samples with the four channels switched on, in a simple i5 (2 cores/ 4 threads, 2.4 GHz Intel CPU, 8 GB RAM) notebook. The decay time of the $LaBr_3$(Ce) is of the order of 20 ns, smaller than the sampling we can manage this way. To stretch the pulses, we have implemented a simple RC-CR circuit after the anode signal and before the scope. With our RC-CR circuit we obtain a decay of 1 μs, that comfortably matches the number of samples we can manage and provides good energy resolution, and sufficient timing. Termination at 50 Ω is not provided by the circuit, but it is present in the PMT and the scope ends. Certainly a gated integrator would perform much better, but for our purposes of doing a fast proof of control run, this was good enough.

4.3 Signal Processing

4.3.1 Time Acquisition

The digitized signal of the four detectors is stored in a memory buffer in the computer. This buffer is read on-the-fly by a program written in C++ by the author of this thesis. The code looks for pulses testing a trigger condition. The way to look for pulses is as follows: we select a section of the buffer and we go through each channel applying a digital threshold condition, verifying whether the signal rises above a threshold of a few mV for a long enough time, to avoid triggering in spikes and noise. This identifies the beginning of the pulse. If the trigger condition is met, the time stamp of the event and the energy of the pulse is saved. Each recorded event is finally labeled with the corresponding channel, the energy and its time stamp value. Recording events in list mode is useful for post-analysis to search for coincidences, which need additional codes, for time alignment and calibrations. Once the events in the list file were time ordered, we selected coincidence events with a narrow time window. Fig. 4.2 shows the time difference spectrum for detectors 1 and 2 for a calibration source of ^{22}Na. The time spectrum shows, as we expected, a narrow peak corresponding to true coincidences and a background of random coincidences. The time resolution of this coincidence peak is 60 ns FWHM. This relatively poor time resolution, compared to the one obtained for similar detectors in previous chapters, is due, obviously, to the decimation in the sampling rate we introduced in this DDAQ. But even so it is more than enough for the purposes of our experiment. A future prototype of this DDAQ will implement a more complex time algorithm and a more sophisticated pulse stretching strategy, which may improve time resolution significantly.

As said before, once the list mode data are properly aligned, it is very easy to obtain singles or coincidence energy spectra of individual or combinations of detectors, for a given time coincidence window. We show results for a test run, again with ^{22}Na, with a time window of 100 ns. Figure 4.3 illustrates the energy spectrum of this source in singles mode for detector 1, and compared

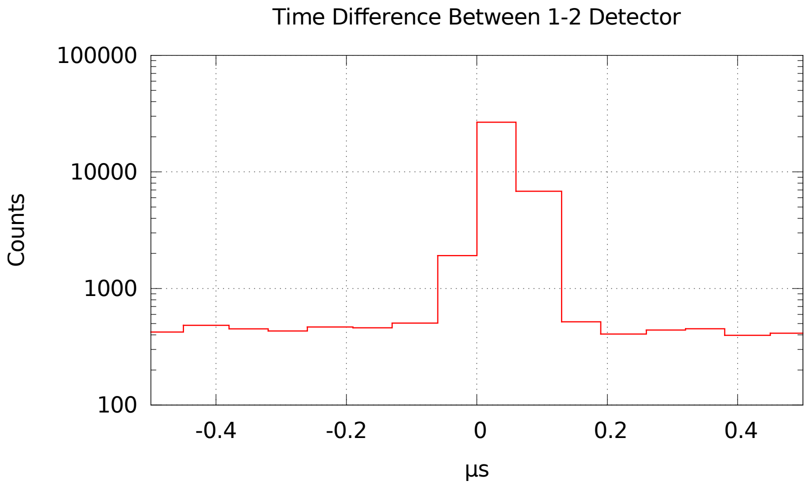

Figure 4.2: Time difference spectrum within a 5 μs time window for detectors 1 and 2 with a source of ^{22}Na

.

to the spectrum in coincidence with any of the other four detectors. The interpretation of these coincidences is straightforward. For example, the coincidences in detectors 1 and 3 are mostly due by the 511-keV annihilation γ ray. We can see in Fig. 4.1 that both detectors are in the same line. This is also the reason why only for this pair of detectors we observe the sum peaks of the 511- and 1275-keV γ rays in coincidence. The contribution of the 1275-keV peak is similar for all the detector combinations, which is consistent with the isotropic emission of the 1275-keV γ ray compared to the 511-keV one.

4.3.2 Energy Measurement

We may think that the 8-bit resolution of the scope can be a limiting factor for the energy or the time stamp. For the time stamp the low digitizing certainly introduces some error, even after interpolating contiguous samples, but it is a very small addition. For the energy, as it is built from all the samples of the pulses, the 8 bit per sample is not really a limitation, and of course the internal representation of the data in the PC is based on float numbers, with no problems for finite resolution. Energy can be obtained with a simple integration (by Simpson's rule or trapezoidal rule) or by applying a Gaussian filter to the pulse (with a digital algorithm) and reading the maximum of the peak to extract the energy [92], in both cases after baseline subtraction. We find better results with a digital gaussian filter as in equation 4.1 and interpolating/fitting to a polynomial the points around the maximum of the gaussian peak. We find a 6% energy resolution for the 511 peak, slightly worse than the best values obtained with this detector, but good enough

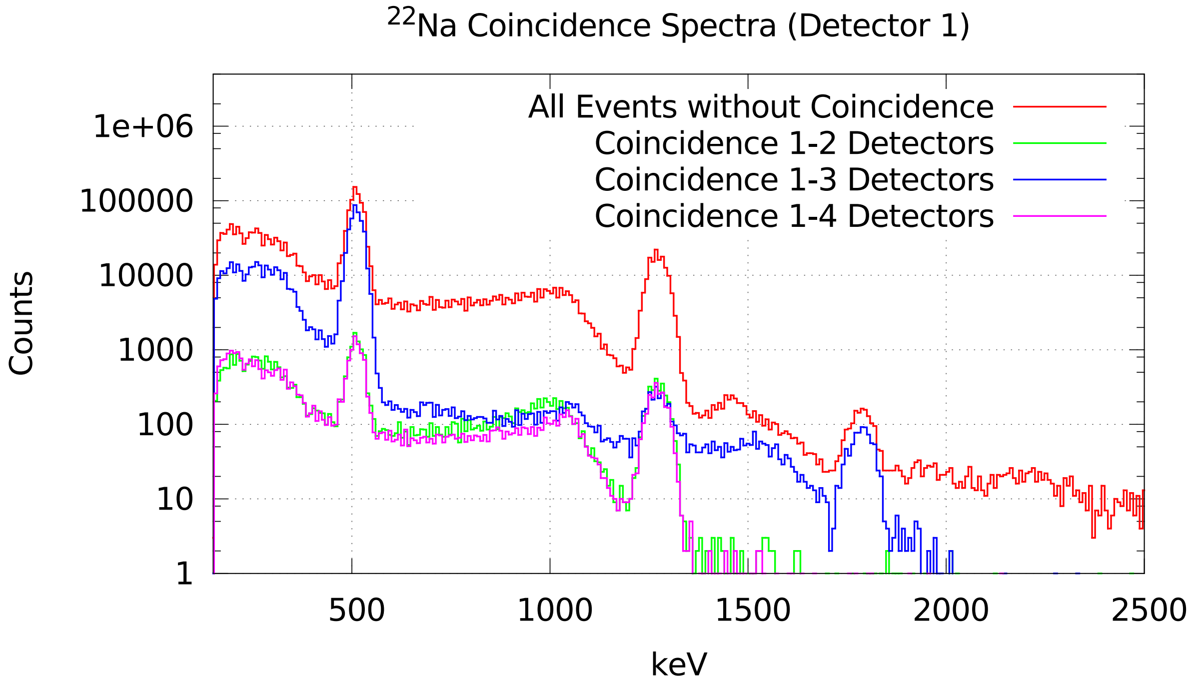

Figure 4.3: Energy spectrum of a ^{22}Na in detector 1 in singles and in coincidence with the other detectors inside a coincidence window of 100 ns

.

for our experiment. The effect of filter is shown in Fig. 4.4.

$$y[n] = \frac{(\tau + \tau^2) y[n-1] + \tau^2 y[n-2] + 2x[n]}{(1 + \tau + \tau^2)} \tag{4.1}$$

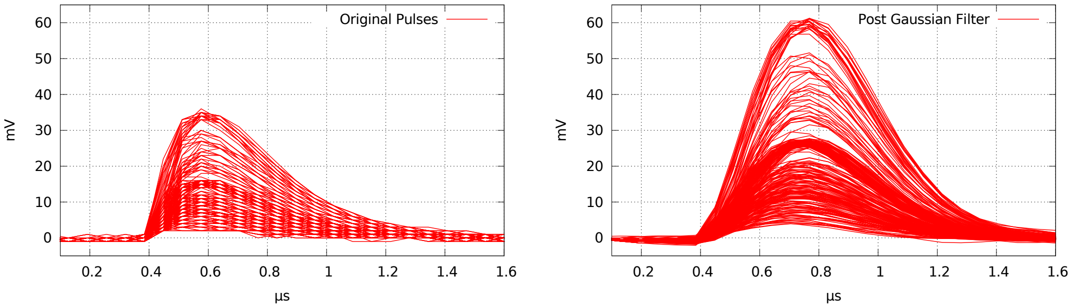

Figure 4.4: Effect of the Gaussian filter on LaBr$_3$(Ce) pulses already shaped by the RC-CR filter.

.

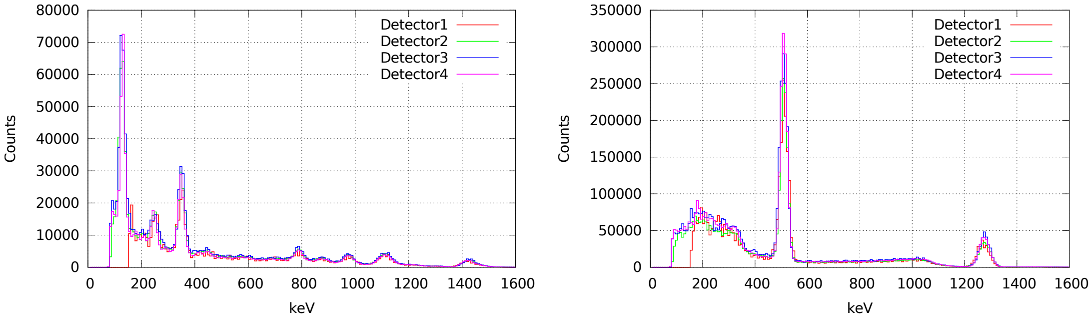

Figure 4.5: Energy spectra from the Gaussian filtered peaks from the calibration sources ^{22}Na and ^{152}Eu.

4.3.3 Efficiency calibration

In order to determinate the absolute activities of the samples after the proton beam irradiation, it is necessary to calibrate the efficiency of each detector. Efficiencies for this experiment have been calculated with a Monte Carlo (MC) simulation using the Penmain package of the Penelope MC code[93]. Further, we validate these simulations for each detector against previous measurement of a standard ^{152}Eu calibrated source placed in the same position as the activated targets. The comparison of measurements with the calibrated and the simulations is shown in Fig. 4.6.

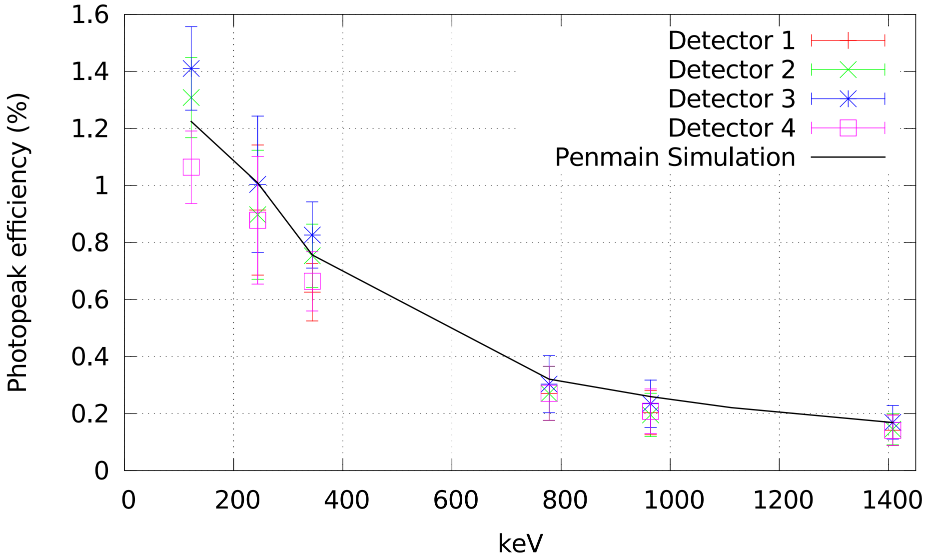

Figure 4.6: Comparison of efficiencies for the full energy peaks. Measured efficiencies agree with the simulations within uncertainties.

4.4 Validation of the DDAQ

The analysis of the activation results is not the main purpose of this thesis, but to illustrate the actual use of the setup, we will summarize the results from the irradiation of various targets, showing how the system managed high enough emissions rates after the irradiation. We will present results for two possible contrast agents and comment on the response of our detector when these targets are irradiated with the 8 MeV proton beam.

The irradiation took place at the exit of the External Microbeam Line of the CMAM facility. This beamline is mainly designed for ion beam analysis in archeometry, but the possibility of producing narrow beams of (much) less than 1 mm in size and with good control of the proton intensity makes it very suitable to simulate a pencil-beam dose deposition of a clinical accelerator. The beam exists the line from vacuum into normal atmosphere through a 0.1 μm thick Si_3N_4 window, with minimum energy losses. The intensity selected in the cases shown here was 3 nA. During the experiment intensities were varied between 0.4 and 7 nA.

4.4.1 Choice of Targets

Targets of CsI and NaCl, were selected to measure iodine and sodium activation cross-sections, respectively. Iodine is a well known used contrast agent in X-ray imaging, mainly in computed tomography (CT)[94]. The only stable isotope of iodine is (^{127}I). Irradiation of this isotope with protons can produce the $^{127}\mathrm{I(p,n)}^{127}\mathrm{Xe}$ reaction. This reaction meets all the requirements to be used as possible production mechanism for a contrast in protontherapy. The threshold for the reaction is very low, around 1.8 MeV, and the activity coming from this isotope will overlap very well with the Bragg peak for dose deposition. ^{127}Xe is a γ-emitter with a meta-stable state with a half life of 69.2 s. In NaCl the reaction of interest is $^{23}\mathrm{Na(p,n)}^{23}\mathrm{Mg}$. The half-life of the corresponding β^+ emission is 11.3 s and it has an associated γ-ray emission. The reaction threshold is around 5 MeV. A summary of the most important parameters of the reactions are shown in Table 4.2 and the decay Scheme of both nuclei is shown in the Fig. 4.7.

The selection of these target materials as powder salts was made because of two reasons: i) that the other elements in the compound will not be activated at the energies studied and ii) that the physical properties of the powder made it possible to built compact targets for easy irradiation. The powder was pressed into thick solid tablets with radius of 0.65 mm and with a mass of 1 g in a tablet press at CMAM. The thickness of the tablets depended of the selected powder, 2 mm for the NaCl and 4 mm for the CsI.

In the following I will discuss the performance of the system and the results obtained.

4.4.2 Decay Results

Fig. 4.8 shows the evolution of the count rate in each detector during NaCl and CsI irradiation. Just before irradiation we see only room background. The beam is at this moment stopped in a Faraday Cup in the middle of the line. This Faraday Cup provides a reading of the current

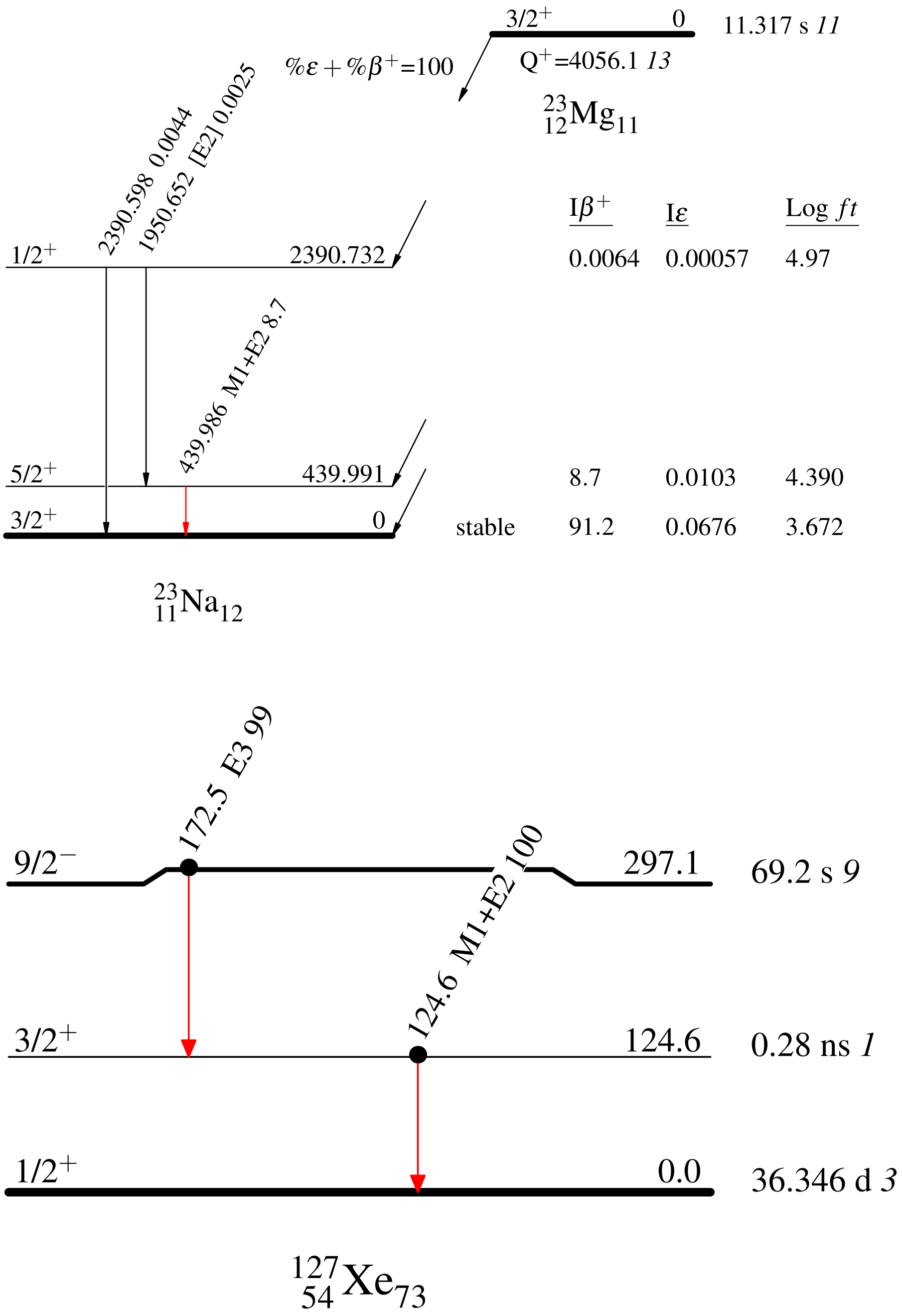

Figure 4.7: Decay scheme for ^{23}Mg (top) and for ^{127}Xe (below).

intensity of the protons, and when present in the path of the beam, it generates activation on the line, producing a prompt emission that increases the background counts in the detectors. After

Target	Product	Energy (keV)	Intensity (%)	Energy (keV)	Intensity (%)
NaCl	^{23}Mg	440 keV	9%	511 keV	200%
CsI	^{127m}Xe	125 keV	69%	172 keV	38%

Table 4.2: Main properties of the radiation emitted when irradiated with protons by the materials tested as contrast agents in protontherapy [95].

measuring the current just before the irradiation, the Faraday cup is removed and the beam reaches the target. At this moment, within milliseconds, due to the large proton intensities, the production/activation is maximum and each detector sees in excess of 100 kcps for NaCl. This value probably reflects saturation of the PC, who is unable of processing pulses at a larger rate. When the time of irradiation is completed, the beam was turned off again, prompt production ceases and only the radiation produced during the decay of the activated targets remains.

Two detectors register larger rates. If we inspect Fig. 4.1 we see that these correspond to the detectors looking at the front face of the targets, the one through which the protons enter directly. Proton range in the target is very small, so there is inert material, inactivated in between the activated zone and the back detectors, much more than between the activated region and the front detectors. Gamma attenuation then explains the difference in the rates of the front and back detectors, and simulations corroborate this fact.

In Fig. 4.9 and Fig. 4.11, we can see the difference on the energy spectra between the whole acquisition time and after the end of the irradiation. We can clearly identify the ^{23}Mg and ^{127m}Xe γ peaks after the irradiation. For the ^{23}Mg, the 511-keV of the β^+ decay appeared along with the associated γ emission.

The 440-keV peak for ^{23}Mg and the 125- and 173-keV peaks from ^{127}Xe were used to set a time gate indicating the production of the activated nuclei

With the time and energy gates applied to the data we can isolate events corresponding to the decay spectra of both elements. In Fig. 4.10 and 4.12 decay curves are shown. They curves correspond to individual detectors and to the sum of all of them. The energy selection, as discussed earlier, was 440 keV in the ^{23}Mg case, and 125 keV for ^{127}Xe. We can fit the curves to the universal decay law 4.2 to measure the half-lives of the activation products.

$$A = A_0 e^{\frac{-t}{\tau}} \tag{4.2}$$

In table 4.2 we show the half-lives derived from our data, and compared them to the tabulated values that can be found in the bibliography. Both for ^{127}Xe and ^{23}Mg the data matches well the NNDC value within uncertainties.

Reaction	$^{23}\mathrm{Na(p,n)}^{23}\mathrm{Mg}$	$^{127}\mathrm{I(p,n)}^{127}\mathrm{Xe}$
Detector	$T_{1/2}$ (s)	$T_{1/2}$ (s)
Detector 1	10.8 ± 0.2	69.3 ± 0.6
Detector 2	11.3 ± 0.3	71.2 ± 1.5
Detector 3	11.5 ± 0.3	73.8 ± 1.9
Detector 4	11.0 ± 0.2	68.9 ± 0.6
Channel sum	11.1 ± 0.1	69.3 ± 0.4
NNDC [95]	11.32 ± 0.01	69.2 ± 0.9

Table 4.3: Half-lives obtained from our fit of the decay curves and comparison to the evaluated nuclear data values.

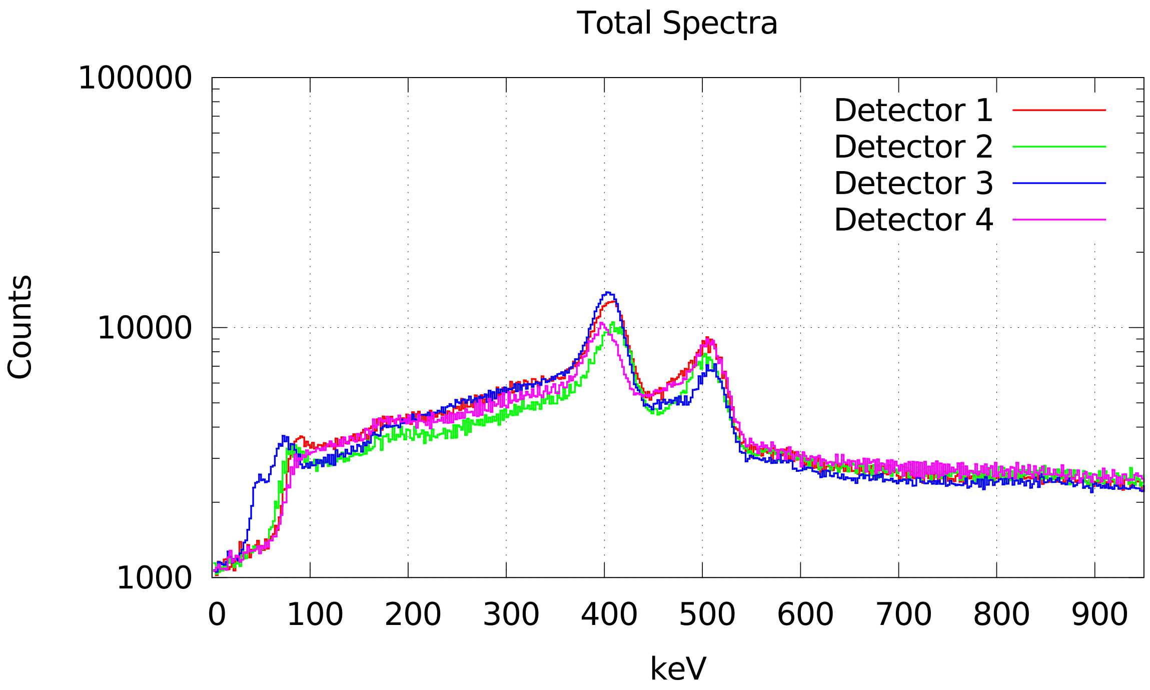

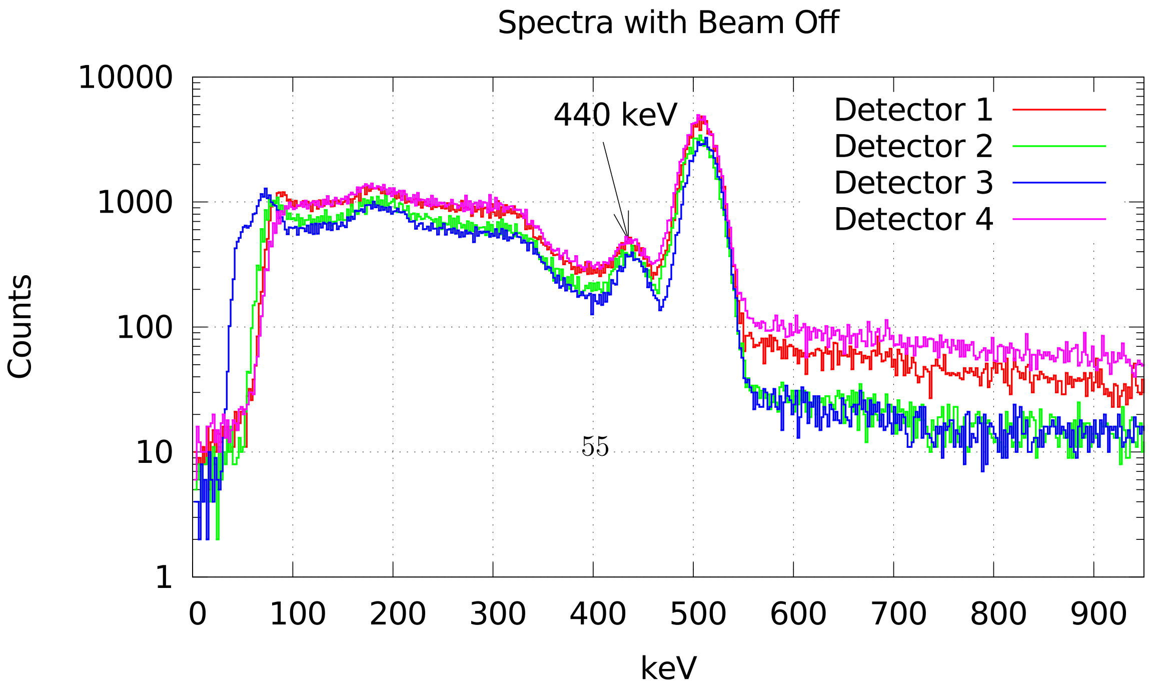

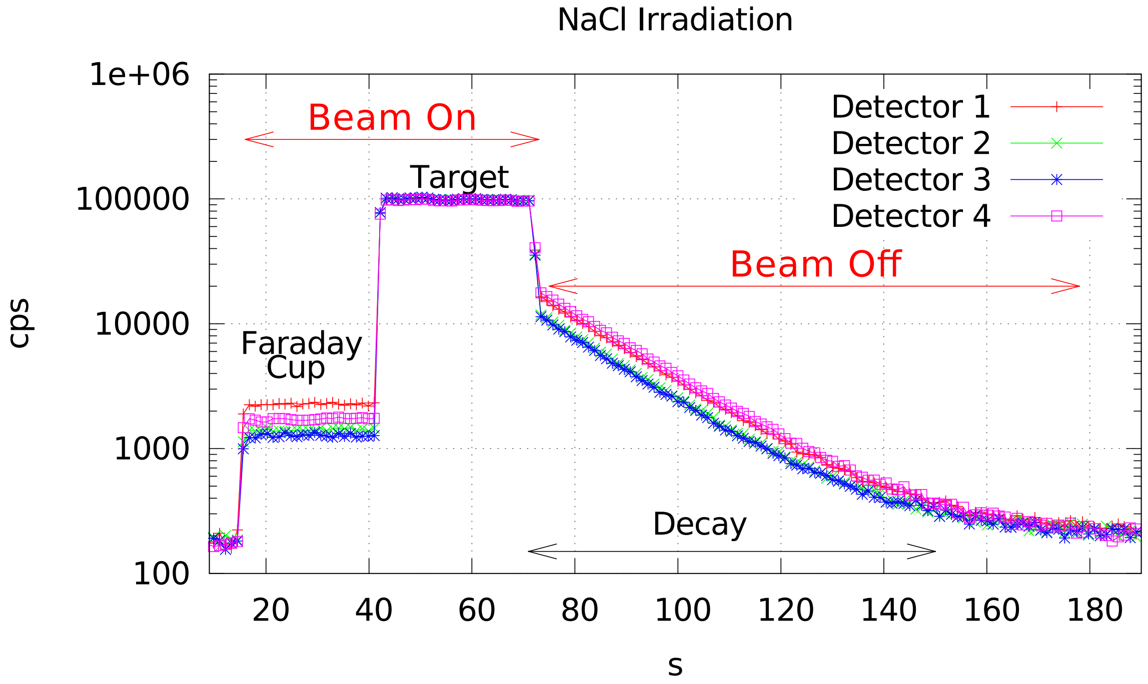

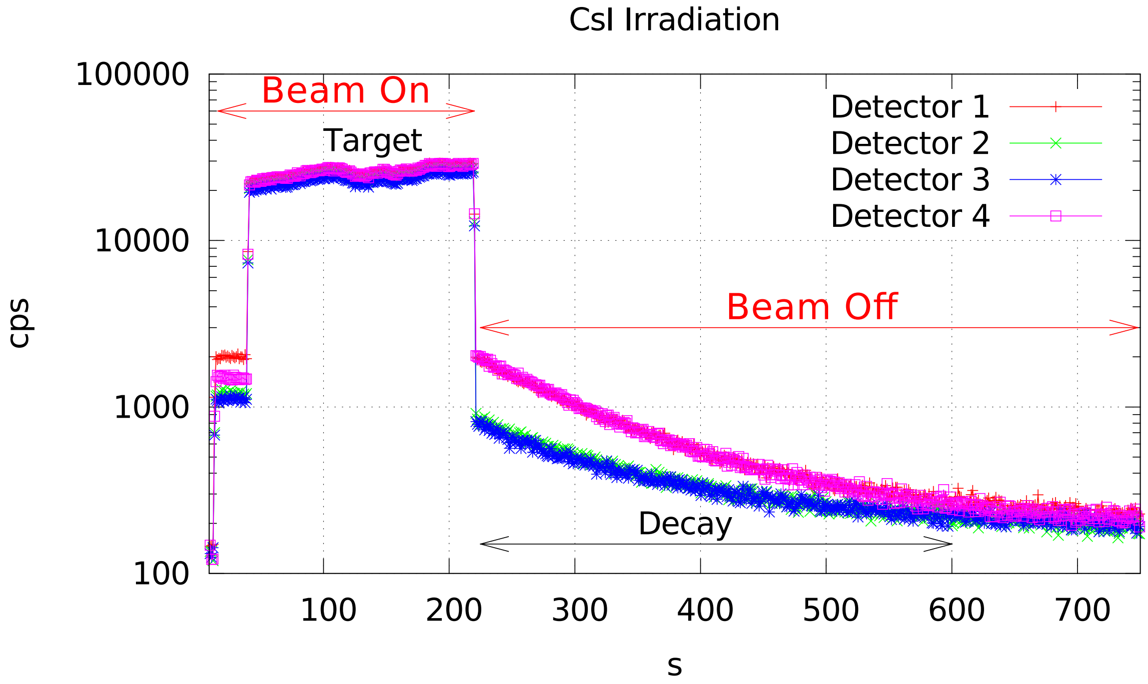

Figure 4.8: Evolution of rates from the NaCl during irradiation and right after proton beam is stopped.

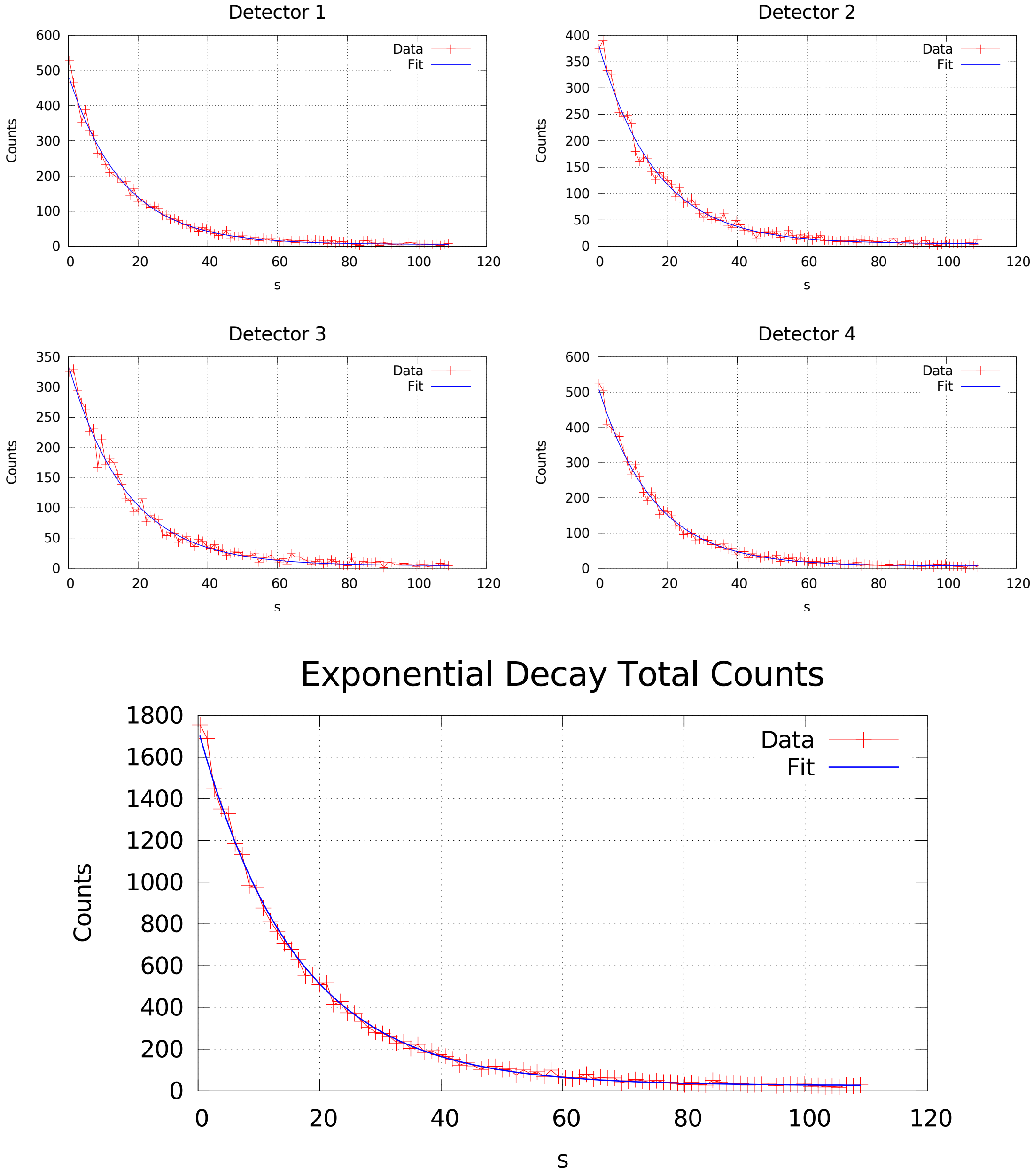

Figure 4.10: Decay curves from each single detector and the sum of them after imposing a gate on the 125-keV peak, and the exponential fit.

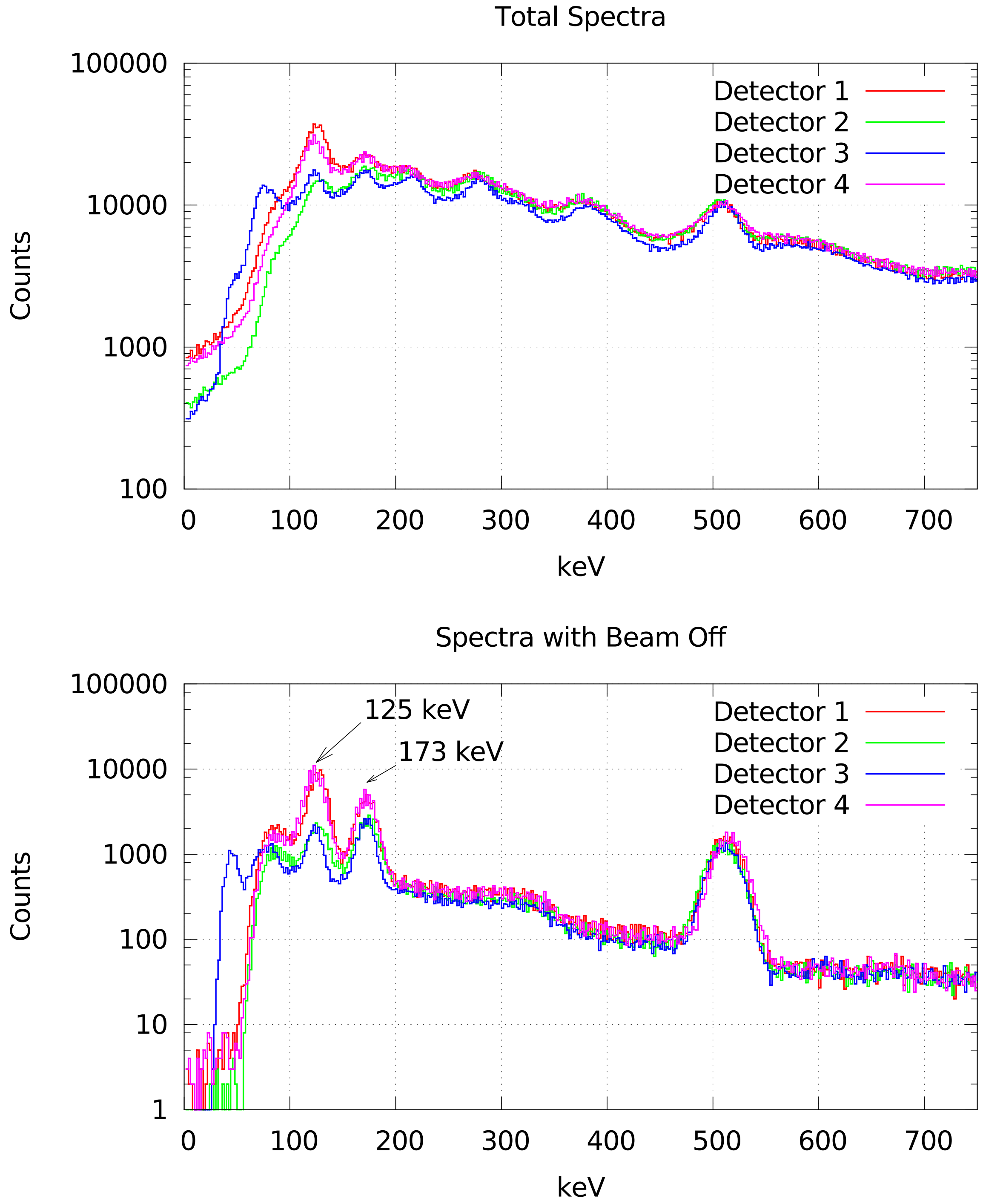

Figure 4.11: Energy spectra of events during all the acquisition (Proton beam on + Proton beam off) and only for events without proton beam (down). In this picture the decay of the metastable state of ^{123}Xe is the main contribution after proton irradiation.

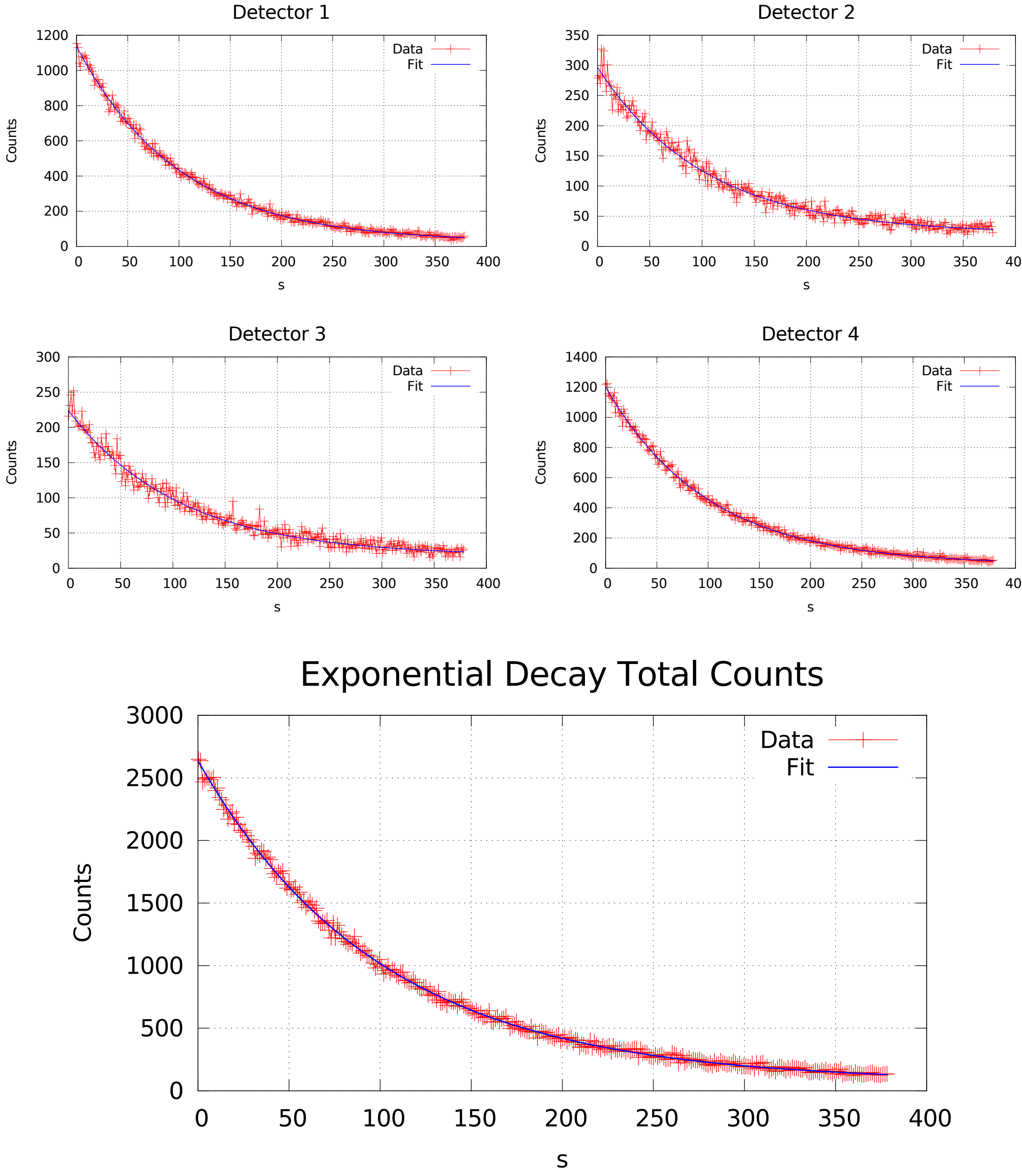

Figure 4.12: Decay curves for single detectors and for the sum of all of them with a gate on the 125-keV peak. The exponential fit is also shown.

4.5 Conclusions

It has been shown in this chapter the viability of our system to handle large event count rates while maintaining a usable energy and time information. The system is very inexpensive, compact and versatile. The most recent tests, described in this chapter, show that our results were limited by the computing power of the notebook, and with a slightly more powerful computer the maximum event rate with this same setup can be much higher. This result paves the way for very simple DDAQ systems in more complex experiments.

Chapter 5

High Performance Digital Acquisition II: Simultaneous measurement of the spectral and temporal properties of a LINAC pulse from outside the treatment room

5.1 Introduction

Another high rates DDAQs designed in this work arises from the need to perform a beam analysis system that can record, from outside the treatment bunker and with high accuracy, the time profile of the γ rays emitted by a clinical linear accelerator (LINAC). This DDAQ is based on digital signal processing of the pulses measured by a fast scintillating crystal with spectroscopic capabilities coupled to a PMT. The system, placed in the control room of the treatment unit, is sensitive to scattered photons emitted from the treatment head when the beam is on[96].

Traditionally, water-equivalent (or tissue-equivalent) plastic scintillators coupled with PMTs have been used for beam monitoring of radiotherapy devices [97], since the time decay of the light emitted is on the order of a few ns, allowing for high count rates and time resolutions of the order of 100 ps. However, plastic scintillators will not provide useful information on the energy spectra of the photons detected within the radiotherapy range. As mentioned in chapter 4, new inorganic scintillating crystals such as $LaBr_3$(Ce) or $CeBr_3$ with a very fast decay time of 20–30 ns have come into the market, allowing for high count rates and very good time resolutions also. In addition, owing to their very good stopping power, they provide good detection efficiency and their energy resolution for photons has no match.

The need for a precise timing characterization of clinical beams arose during our research in photoacoustic imaging [98, 99, 100], where an exact knowledge of the time profile of the dose pulse is essential for reconstructing the three-dimensional dose distribution from detected shock waves. In protoacustic measurement [101] it is used the fact that after the fast deposition of energy produced by the deposition for X-ray or protons in a tissue, there is an increase of temperature that generates a thermoelastic expansion. This expansion produces an acoustic wave via the photoacoustic effect[102, 103]. Ultrasound transducers may detect this acoustic signal and generate a image of the dose deposited in it. Synchronization of the signal received in the sensor with the pulses impinging in the irradiated object is very important, as well as knowledge of the fine time structure of the beam of particles, in order to compute the expected acoustic wave the beam produces, and which would be used to reconstruct the deposition of the dose.

A key attribute of the proposed system is its ability to perform measurements of the actual time structure of the beam, with a detector located in the control room, outside the treatment bunker, taking advantage of the limited amount of detectable radiation present in the control room. This is possible thanks to the increased sensitivity of the scintillating crystals [104, 105], which also provides precise spectral knowledge of the scattered radiation, and it allows the measurements to be carried out without any interference with patient treatment or research activities. Together with the new scintillator materials, full digitization of the pulses was employed in this work, in order to obtain the maximum flexibility, and to take advantage of the many algorithms which can be applied in the digital domain to deal with pulse pile-up. Also, we have to consider the very limited time we had to characterize the radiation in the hospital, and that the possibility to acquire all the data and to try on the same sets many possible algorithms, without the need to acquire further data, constituted a very strong advantage of the DDAQ approach. Digital analysis allowed us to obtain clean spectra, free from pulse pile-up in a very simple manner.

5.2 Experimental Setup

The detector used in this work was a cylindrical Scionix $CeBr_3$ scintillator (2.5 cm length, 2.5 cm diameter) coupled to a fast PMT, model Hamamatsu PMT model R9779. The PMT was connected to a high voltage of 1000V (slightly below the recommended value of 1300V, to avoid pile-up and saturation effects). The dynode signal from the PMT was digitized with an Agilent DSO 6104A oscilloscope with a bandwidth of 1 GHz, 8-bit vertical resolution and a maximum sampling speed of 4 Gsamples/s. We selected a sampling speed of 0.1 Gsamples/s and an time acquisition window of 10 μs. At this digitizing speed, the scope used the additional samples to increase the effective vertical resolution to 11 bits. The oscilloscope was read via USB to a PC.

The measurements were performed in the Cyberknife^{TM} unit (Accuray Technologies, Sunnyvale CA, USA) at the Hospital Ruber Internacional (Madrid, Spain). The unit is equipped with a 6 MV linear accelerator mounted on a 6 degree-of-freedom robotic arm. A circular brass collimator was used to shape the field, with an aperture size of 5 mm at a reference distance of 80 cm. The dose rate was kept at 600 Monitor Units per minute (100 MU are equivalent to an absorbed dose of 1 Gy delivered to the point of maximum dose in the depth-dose profile in a phantom of water of 10×10 cm^2 of cross-section). In order to study geometrical and scattering effects, measurements were taken with the robotic arm in horizontal, vertical and oblique (45^{o}) positions, and no target. Furthermore, to investigate in-patient scattering, an additional measurement was taken with the arm in vertical position and the beam irradiating a cubic (1 m-side) water phantom, positioned at a source-surface distance of 48 cm. The detector system was placed at in the Cyberknife control room (outside the shielding maze), at an approximate distance of 5 m from the isocenter and behind a 1.8 m-wide wall of concrete. In the Fig. 5.1 the positioning of the detector is shown.

The acquisition was triggered using the magnetron output signal (MAG) from the Cyberknife control unit. This signal is active whenever the high voltage magnets are energized, regardless of whether the beam is on or not, which allowed us to use the same trigger signal for the background measurements. This signal is approximately square, with a duration of about 5 μs and a pulse repetition frequency of 100 Hz.

5.3 Digital signal processing

Every time the trigger signal goes active, the oscilloscope captures 10 μs from the dynode output of the PMT. A batch of signals then consists of several captures (20,000 samples per measurement), which must then be post-processed to obtain the time profile and energy spectrum of the beam.

5.3.1 Background Subtraction

Radiotherapy treatment rooms are environments with high electromagnetic noise, due to the presence of radiofrequency fields and high-voltage switching devices. This noise can easily alter the measurements of sensitive electronics. Moreover, the possible presence of activated radioactive elements can contribute to an increased background radiation being detected by the scintillating crystal. It is therefore necessary to perform a background measurement and to use it to correct all subsequent acquisitions.

Before the irradiation, we took a background measurement of 2000 samples with the high voltage magnets energized and the robotic arm in vertical position. Due to the low duty cycle of our measurements (below 0.1%), the rate of random events (radiation captured at the scintillating crystal but not originating from the beam) is extremely low in comparison with the signal from scattered radiation present outside the treatment room during irradiation. The main contribution to the background is the electromagnetic noise caused by the accelerator, which appears synchronized with the trigger signal and is present regardless of whether the beam is on or off. Fig. 5.2 displays a superposition of 15 consecutive traces (in red), together with the noise synchronous background signal (in black) and the trigger signal (in blue). It is not possible to avoid this synchronous noise by averaging consecutive signals, and it must therefore

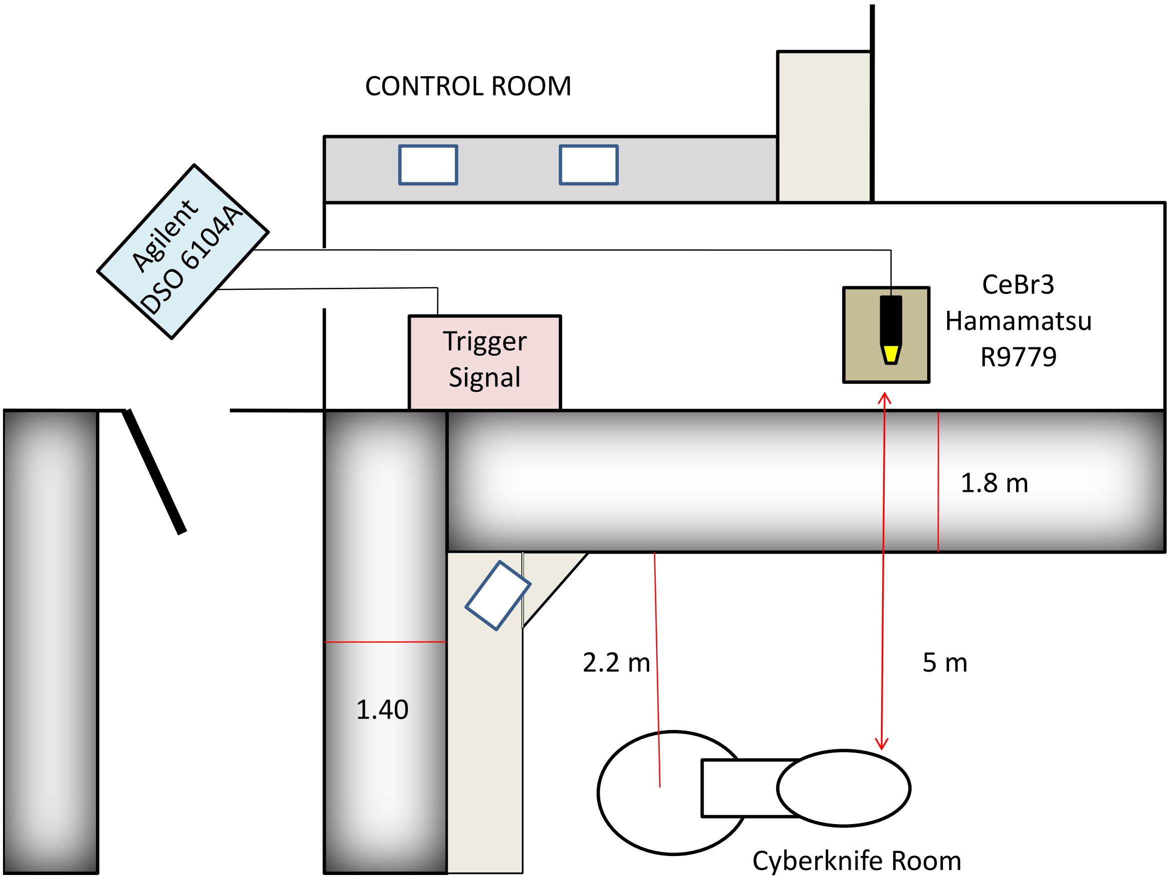

Figure 5.1: Sketch of the treatment room showing the relative position of the detection system and the treatment unit. Detector is placed at 5 meter from the accelerator and with a wall 1.8 m of concentrate between them. The idea is to design a way to analyze the information of the photon produced by the Cyberknife (time distribution and energy spectra). For this purpose, the $CeBr_3$ detector has to be located outside the treatment room. The large number of events that could hit the detectors if we placed it inside the bunker is too large to handle without saturating the detector and with a large possibility of even damaging it. The main reason behind the design of this system was to develop an easy way to monitor the time distribution of the emitted photons (important to know the time distribution of dose deposition in the tissues), and usually it is assumed as a Gaussian but this does not need to be the case. Digital systems allow us to easily determine this distribution by means of a fast crystal like $CeBr_3$ and correlate each event with the trigger signal. Decreasing the number of events keeps the time distribution invariant and only reduces the number of events in the detector.

be subtracted from all measured pulses in the post-processing stage.

5.3.2 Pile-up events

The high voltage gain of the PMT coupled to the $CeBr_3$ crystal and the trigger level in the scope are adjusted to count individual photons arriving at the detector. Because of the high pulse rate

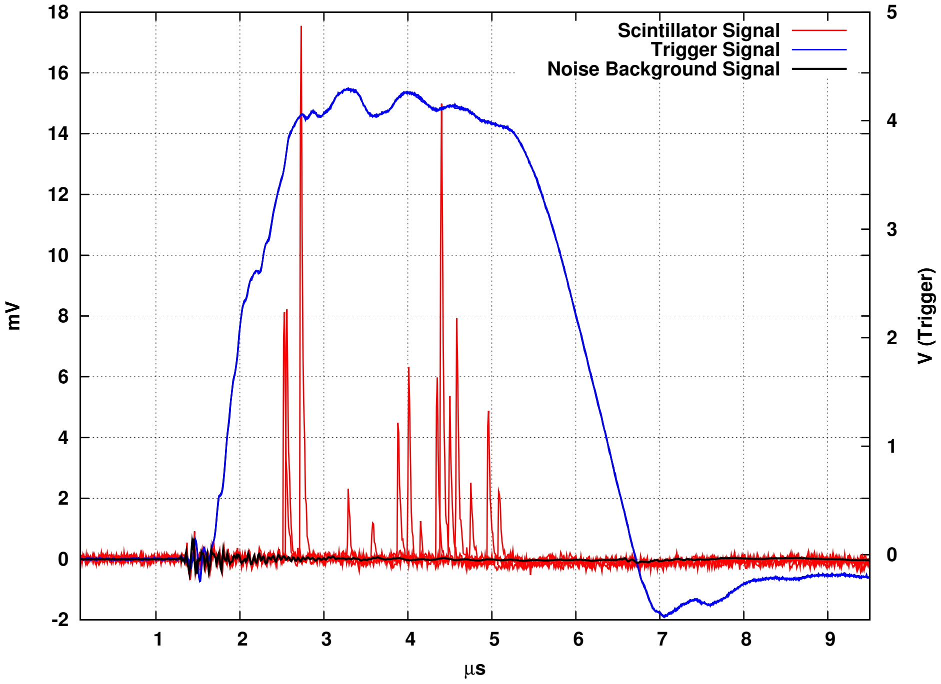

Figure 5.2: In black, the background signal averaged from 2000 samples. We can eliminate this contribution only by subtracting it from the PMT signal. In red, superposition of 15 signals measured by the CeBr$_3$-PMT detector containing one photon each. We can count photons individually and to determine their time stamp with respect to the Magnet Trigger signal (blue line). After this, we can easily make a histogram of the time distribution of the emitted photons

.

in the detector when the trigger is on, different photon events can be captured in the same time window in a single trigger cycle (what we call time-window pile-up events). This effect can alter the derivation of temporal and spectral profiles from the set of collected signals and must thus be corrected for.

The correction for pile-up events was based on a shape-factor study of the pulse. There are different ways to relate pulse shape with incoming photon energy, with the simplest of them using either the maximum pulse value or the pulse integral (obtained via trapezoid rule). Therefore, we expect a linear correlation between these two values, as they both are expected to have a linear correlation with the incoming photon energy. When more than one photon hits the detector during a single acquisition window, the correlation between maximum pulse height and pulse integral is changed, and we can use this to filter out these pile-up events.

For our measurements, we applied a cut-off to events where the integral value does not follow a linear correlation with the maximum pulse value to filter out pile-up events, setting the threshold (solid line in Fig. 5.3) at 20% of the median of the integral values for a given maximum value. Events reaching the maximum dynamic range of the digitizer were also filtered out. The ratio of filtered events ranged from 2.5% of the pulses (in vertical position) to 7% of the pulses (in horizontal position, where the event rate is highest). The distortion introduced in the spectral measurements by this filtering is minimal.

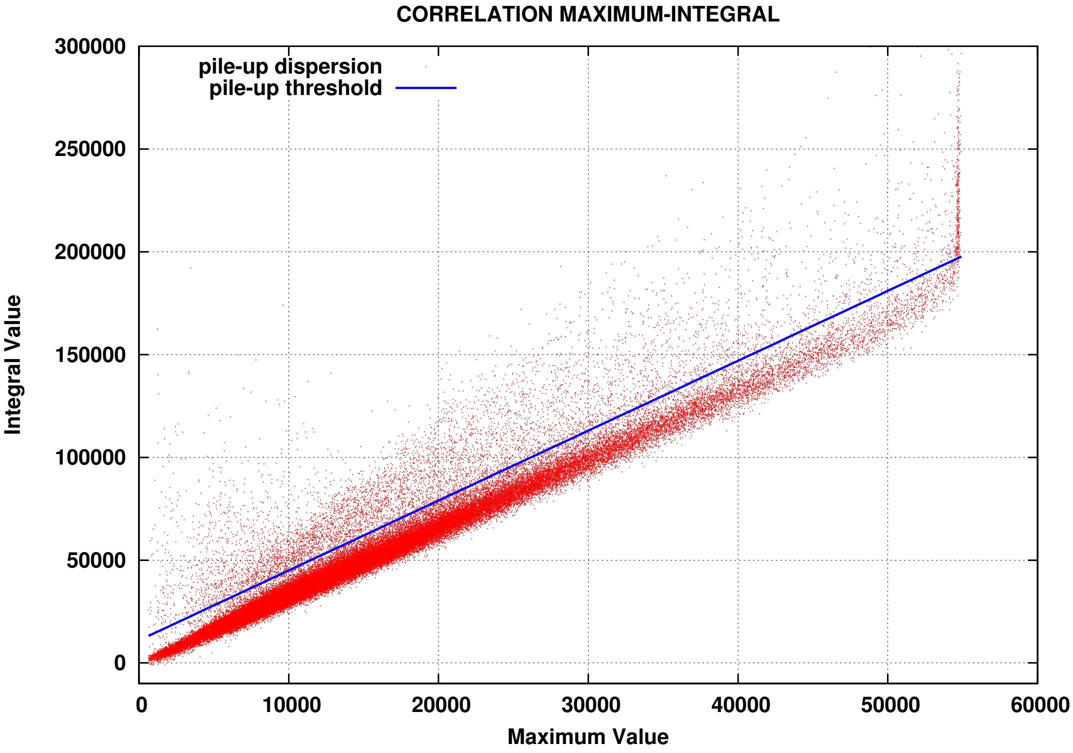

Figure 5.3: Pulse integral value (in arbitrary units) vs. pulse maximum value for 20,000 events measured with the robotic arm in horizontal position. The blue line marks the threshold above which events are considered pile-up and discarded.

.

5.3.3 Derivation of time profiles

Time profiles are extracted from the series of individual photons (such as the ones shown in Fig. 5.2). For each photon (excluding pile-up events), the pulse arrival time is determined from its leading edge, detected when the signal crosses a threshold of 0.5 mV and stays above that threshold for more than 3 consecutive samples (30 ns). The accuracy of this algorithm is limited by the sampling time of our system, which amounts to 14 ns with respect to the trigger signal.

The energy of the pulses is determined from the integral of the detected pulse. Once a valid pulse has been captured (duration above 30 ns), the system calculates the definite integral using the trapezoidal method between the position of the maximum value and a position delayed 100 ns with respect to it. The correlation between pulse integral values and photon energy values was determined using the 511-keV and 1175-keV full-energy peaks of a ^{22}Na calibration source, acquired in self-trigger mode with high voltage magnets in the room turned off. The FWHM energy resolution of the system in these calibration peaks was estimated 5.5% at 511 keV.

As we have mentioned in Section 5.3.2, pile-up events were excluded from the spectral analysis. The obtained spectra were also corrected for the efficiency of the detector (shown in Fig. 5.4), calculated via Monte Carlo simulation with penEasy/PENELOPE [93, 106] under the assumption that the incidence angle of photons is roughly perpendicular to the base of the scintillating crystal and taking into account that the dimensions of the crystal are similar in all axis (2.5 cm in length and diameter), thus minimizing the influence of the angle of incidence in the efficiency to less than 3% for incidences up to 45º (and less than 10% for perpendicular incidences, significantly less likely to occur), according to our simulations.

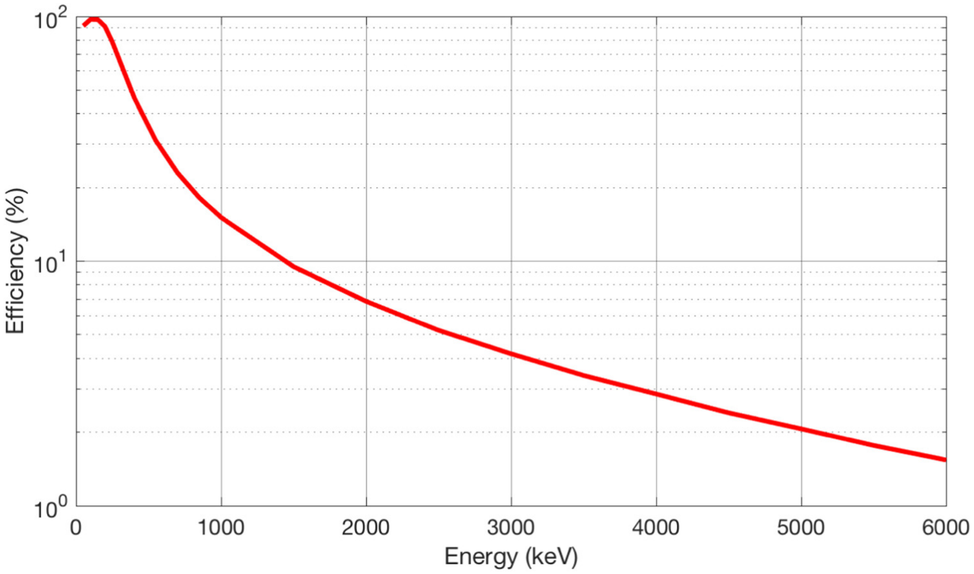

Figure 5.4: Detector efficiency as a function of the energy of the incoming photons, calculated via Monte Carlo simulation.

.

5.4 Results

In the reported irradiation tests, our CeBr$_3$-PMT detection system registered with 100-ns accuracy the time profiles for different beam orientations. Each of the profiles shown in Fig. 5.5

corresponds to an average of 20,000 trigger events, post-processed for background subtraction and pile-up filtering. Three acquisitions were performed without a target at three different gantry angles (horizontal, vertical and 45 degrees), plus a fourth one, in vertical orientation, using a water phantom as a target. The four measured profiles show a quasi-identical time behavior and differ only in the number of events. As we expect from the distribution of Compton events, when the beam is placed horizontally pointing towards the detector, the number of registered events increases, and it is minimum when the beam is pointing downwards. There are no significant differences between the profiles obtained with the beam in vertical position with and without a water target, from where we can deduce that most measured photons originate in the treatment nozzle and the contribution of particles scattered from the target is minimal.

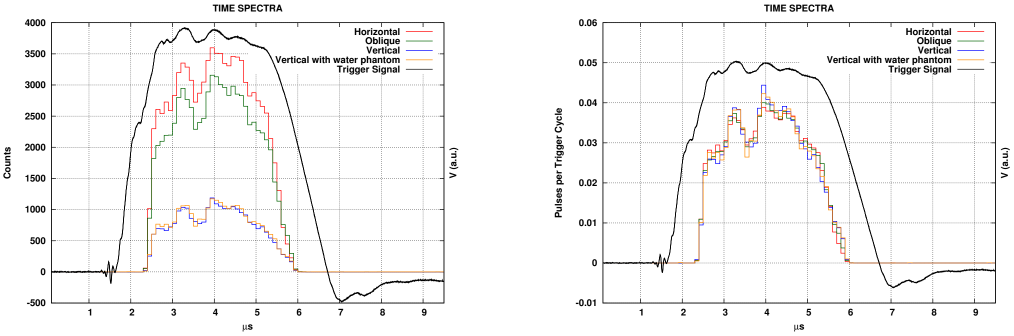

Figure 5.5: Time fluence profiles registered for the four different beam configurations (horizontal, oblique, vertical, vertical with target) for 20,000 triggered events. Bottom: Time fluence profiles normalized to the number of captured events (i.e. non-empty trigger cycles).

.

The energy spectra measured in the control room for the three different orientations are displayed in Fig. 5.6. These energy spectra registered at the measurement position (see Fig. 5.1), after potentially several Compton scattering events and significant hardening of the beam through the shielding material and modulated by the energy response from the scintillating crystal (Fig. 4). At low energies (below 600 keV), the energy distribution of received photons seems to be independent of the position of the accelerator (within uncertainty ranges). However, above this threshold, we observe a higher proportion of energetic photons for more direct beam incidence positions. This is expected, as photons arriving to the detector in less direct trajectories have undergone more Compton scattering and thus have a lower energy. The average photon energies are 0.69 MeV, 0.67 MeV and 0.62 MeV for the horizontal, oblique and vertical positions, respectively.

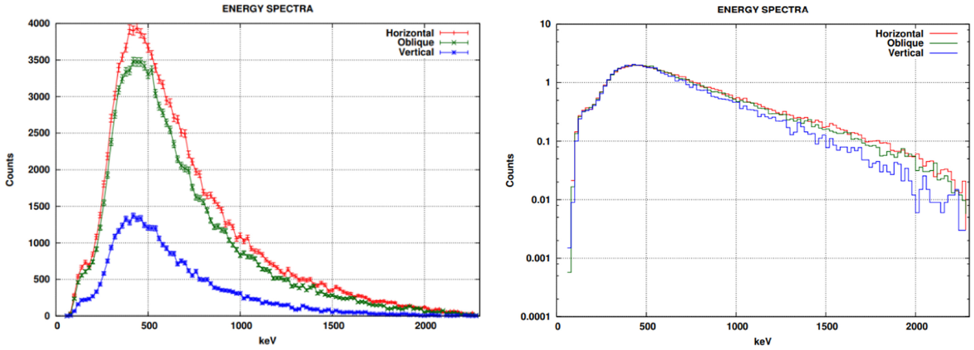

Figure 5.6: Measured energy spectra for different beam orientations and without target, displayed in linear (left) and log (right) scales, corrected for detector response.

5.5 Conclusions

With the presented system, it is possible to acquire simultaneously, from the LINAC control room, the time profile of the dose pulse and the energy spectrum of the scattered radiation outside the bunker. This characterization of the beam is relevant not only for research purposes (γ-acoustics, development of new detectors) but it could constitute a useful tool to assess the performance and stability of the LINAC. For instance, an increase in the ratio of radiation-empty pulses (or a decrease in the average number of photons detected per pulse) could be an indication of incorrect machine operation. In protontherapy, it has been proposed to measure the photons originated in the irradiation place, in the distal end to the entrance of the beam in the patient, to monitor placement of the patient and accuracy of the proton range estimate. Our measurements in the LINAC can be considered as a proof of concept for all these measurements.

Fully digital treatment of the pulses allows us to easily filter the intense electromagnetic noise and simplifies the derivation of the energy spectrum of the received photons, consideration of pulse pile-up, allows for averaging of data from consecutive radiation pulses, and maximizes the information obtained from the detector without the need for additional complex electronics.

Batch measurements of 20,000 triggered signals, at a pulse rate repetition of 188 Hz, were acquired in less than 2 min. Even placing our detectors outside the treatment room, we are able of capturing, on average, more than one usable (i.e. not piled-up) photon per trigger at every beam orientations (1.3, 3.7 and 4.3 photons per trigger for the vertical, oblique and horizontal angles, respectively), with the fraction of triggered pulses without any photon acquisition at 24.7%, 1.1% and 0.4% at the three respective angles. This rate is sufficient to acquire enough statistics during normal patient, QA or research irradiation. Further analysis of multi-photon events could, if needed, increases the number of usable events and therefore the acquisition efficiency. Moreover, an analysis of the proportion of empty pulses and mean number of photons per pulse could be an indication of the correct operation and stability of the LINAC, since a higher-than-usual number of radiation-empty pulses could be linked with system malfunction.

With regards to the energy spectra measured outside the bunker (Fig. 5.6), its relation to the full spectral information from the treatment beam is difficult to obtain. Even with a full Monte Carlo analysis [107, 108, 109] including simulation of the treatment nozzle and room shielding geometry and spectrum correction for angular-dependent detector efficiency [106], the derived spectra are still limited by the response of the crystals to photon energies above 1.5 MeV (Fig. 5.4). Moreover, the pile-up correction negatively affects the registration of energetic photons (above 2 MeV).

In summary, the proposed setup has been successfully used to accurately measure the time profile and energy spectrum of the scattered radiation outside the treatment room from a Cyberknife$^{\mathrm{TM}}$ clinical accelerator.

Chapter 6

High Performance Digital Acquisition III: Development of a new setup for the study of the γ-MRI imager

6.1 Introduction

In this chapter we will continue with the development of new DDAQs geared towards applications involving high rates of events. As in other chapters before, there is a medical application behind this system. Again, we are not going to discuss the results of the experiment, which is not the purpose of this thesis, but on the features of the DAQ developed and tested. This work was performed within the CERN-UCM-UNIGE and HEdS-Geneva collaboration to develop a new hybrid medical imaging modality with promising benefits for *in vivo* studies. This technique is based on combining the high spatial resolution of Magnetic Resonance Imaging (MRI) while increasing the sensitivity of the technique using radioactive tracers as contrast agents. This new technique is also called Polarized Nuclear Imaging (PNI) [110, 111].

6.2 Theoretical Background

MRI is founded on the magnetization of atomic nuclei with spin, for instance hydrogen inside tissues, due to a external magnetic field. This magnetization of the nuclei is aligned to some extent with the external field [112]. If we turn on a radio frequency (RF), it can change (flip) the magnetic state of the nuclei tipping the nuclei spins of the tissue. Normally the spins tend to come back to his original position after some characteristic times, (T_1) for the longitudinal component of the magnetization, and (T_2) for the transverse. The precession of the spins, or change from longitudinal into transverse magnetizaton and vice-versa, induce an RF signal that can be recorded in a receiver coil[112]. (T_1) and (T_2) contain the information of the tissue and are used to generate a image.

The use of hyperpolarized gasses as contrast in MRI is a well-known practice with various years of experience [113]. These gases have nuclei with nonzero magnetic moment, and the are polarized, for instance with the Spin-Exchange Optical Pumping technique (SEOP) [114]. This technique is based in irradiating an alkali metal vapor with resonant circularly polarized light. This generate a population accumulation of one spin state of the alkali metal electrons and a depletion of the other, creating a electrical spin polarization. The collision of the the alkali vapor particles with the gas particles transfer the polarization of the alkali electrons with noble gas nuclei force the later to polarize. This process goes on until yielding a steady-state nuclear spin polarization. If a RF is turn on tipping the nuclear spin of the hyperpolarized gas, a NMR can be generated too, with relaxation times T_1 and T_2, as in ordinary MRI. This is specially practical in zones where the hydrogen concentration is low, such as the lungs. In these zones the concentration of the contrast can be increased with the inhalation of gas by the patient which will fill the MRI signal, compensating the lack of hydrogen in the zone.

The new PNI technique proposed by [110] suggests obtaining the image information through γ-rays detection. For instance, native Xe nuclei are stable, but there are some isomers of this nucleus like $^{129\mathrm{m}}$Xe and $^{131\mathrm{m}}$Xe whose decay could be of great interest for imaging. These isomers have a transition decay $\frac{11}{2}^{-} \rightarrow \frac{3}{2}^{+}$. The important part in this transitions is that their geometric emission has a dependence with the polarization of the nucleus. Thus in presence of an external field, if polarized, the radiation coming from decay of these nuclei exhibits an anisotropy that increases with the polarization of the gas. If we polarize the sample, the emission on the traverse axis of the external magnetic field increases and it decreases on its longitudinal (parallel to the magnetic field) direction[115, 116]. This effect is shown in the Fig 6.1.

Polarization of hyperpolarized nuclei can be achieved through SEOP process as for the stable ^{129}Xe contrast in the presence of a magnetic field. If we were to make a normal MRI, we would send a RF pulses that tips the spin of the nuclei and we would wait to receive the RF generated by the relaxation of the spins to make the signal analysis. The idea behind PNI is to use the asymmetry of the gamma decays of the isomer verson of the contrast nuclei, that is, the variation on the γ counts at different angles to the magnetic field, instead of using coils to pick up the very faint and nosisy signals typical of MRI. The idea is to study by how much the number of counts for detectors in the transverse and longitudinal axis changes. For instance, We define the sample in the center of a coordinate axis XYZ, being Z the direction of the magnetic field where the polarization exists and we tip the spin whit a RF into the transverse Y plane. An increase of the counts on a detector located on the Z axis will appear. This excess of counts will disappear with the relaxing of the spins. Also this increase will change with spin precesion. If we study this variation we obtain T_1 and T_2 values of a typical MRI and can make an image of the Xe distribution.

In our realization of the experiment, performed in Geneva, the metastable Xe isotope, produced at ILL, was contained in a glass cell and placed in the center of a static magnetic field. This

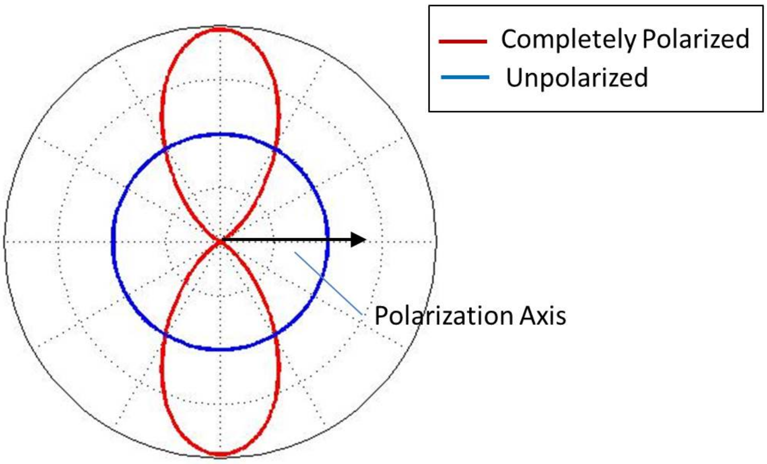

Figure 6.1: Example of angular distribution of ^{131m}Xe 164 keV γ rays with 0% and 100% polarization [111]

glass bowl was introduced into a insulating oven and was hyperpolarized with the SEOP method. We tried to measure the anisotropy generated with this technique using multiple γ detectors surrounding the oven, trying to detect the geometrical distribution of the γ emission.

6.3 Experimental setup

The details of this experiment which this thesis deals with is only the development of the detectors and DAQ, but before going in depth into it, we make a brief resume of the set up.

The system consist of a glass cell filled with alkali metal rubidium as well as buffer gases N_2 and He. The radioactive ^{m}Xe was placed into the glass cell that later we would hyperpolarized. The surrounding oven was communicated with a system consisting of an air compressor and a heater. The oven had a double function, in the first place, it was used to heat the Rb in order to generate a Rb vapor that can transfer its polarization to the Xe. The other function is to isolate the surrounding detectors in order to avoid effects due to their temperature dependence.

The polarization was generated with a laser laser diode arrray, the model is called BrightLase®Ultra-100$^{\mathrm{TM}}$ from QPC Lasers [117]. This laser provides a 50 W continuous-wave 794.7 ± (0.3) nm beam with 0.4 nm maximum spectral bandwidth, coupled to an 800 μm optical fiber. A quarter-wave plate is used in order to left-circularly polarize the light. A wavemeter is located in the back of the oven in order to check out the laser transmission. This way it is possible to monitor when the Rb absorbed the laser light and the polarization starts to occur.

After the Rb spin was transferred to ^{m}Xe we were able to align the Xe with a static magnetic field, this field was of 4.5 mT and generated by two Helmotz coils. In the Fig. 6.2 a scheme of the detectors is shown.

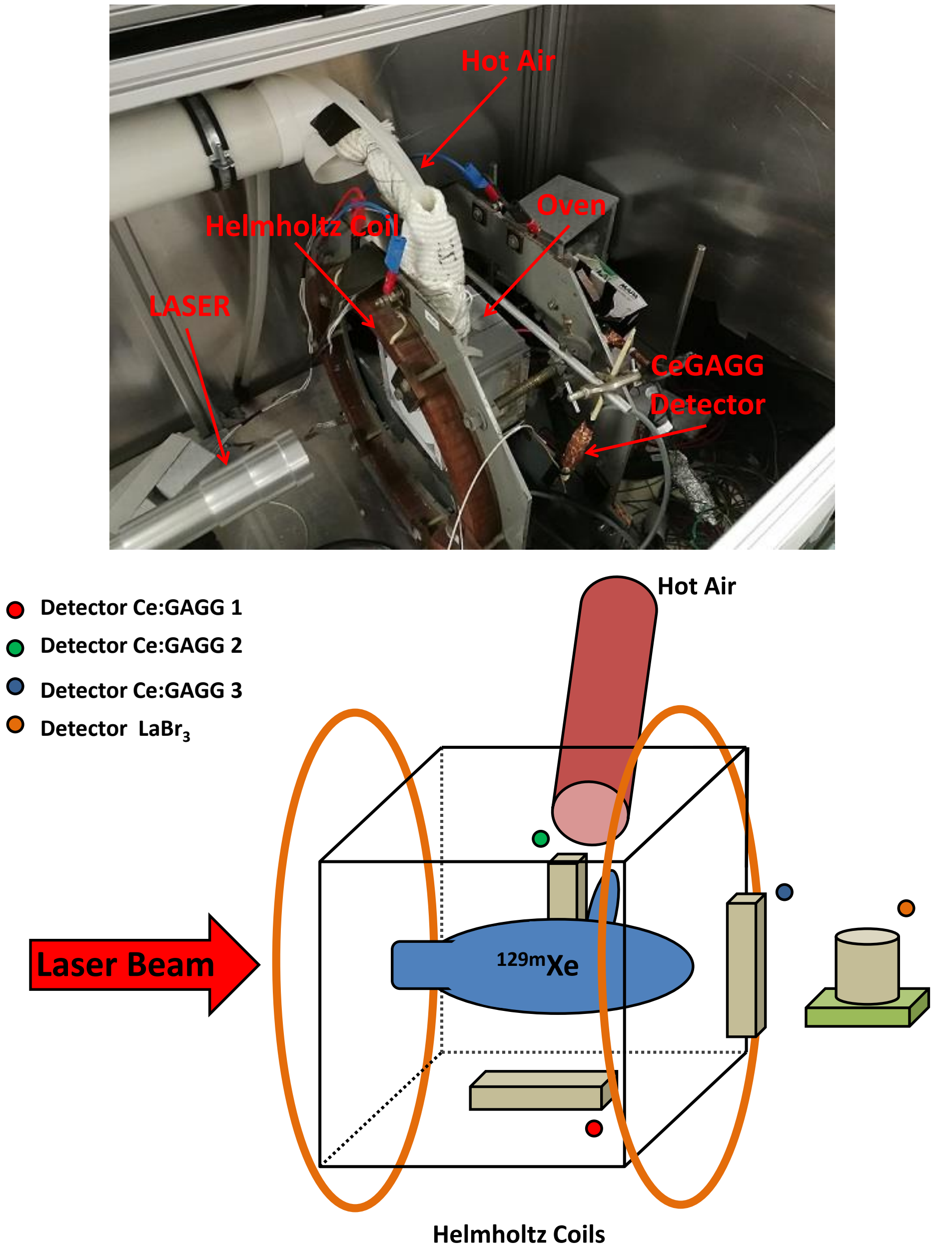

Figure 6.2: Schematic of the experimental set up showing the position of each γ detector.

6.3.1 Detector Setup

The experimental setup consists of three CeGAGG scintillator crystals coupled to a SiPM S13360-6075CS from Hamamatsu. The size of the crystals is 1x1x3 cm^3. SiPMs are a key ingredient in this experiment. They are not affected by magnetic fields, they are very compact in size and they require a small DC bias voltage, which make them perfect for high granularity, easy placement, detectors. In the Fig. 6.3 a photography of three detector is shown. CeGAG scintillator was chosen. It has a good photon yield (50000 photons/MeV), no internal activity and a large stopping power, and further its emission wavelength matches well the SiPM spectral sensitivity. Scintillator surfaces were covered with Teflon tape, except for the one in contact with the SiPM. Optical grease from Saint-Gobain was used in the scintillator-SiPM junction. Above the Teflon, a layer of tedlar film was used as finish wrapping of the detectors, to stop external light. Finally, we added a fourth detector made of $LaBr_3$(Ce) scintillator with a cylindrical shape of 2 cm in diameter and 2.5 cm height, coupled to a 2x2 MicroFJ-60035 SiPMs matrix, each pixel of 6x6 mm^2 from SensL. The smaller stopping power than CeGAGG was compensated by the larger size of the crystal. $LaBr_3$(Ce) is highly hygroscopic and thus had to be encapsulated in an aluminum case, with a front window of 0.5 mm thickness.

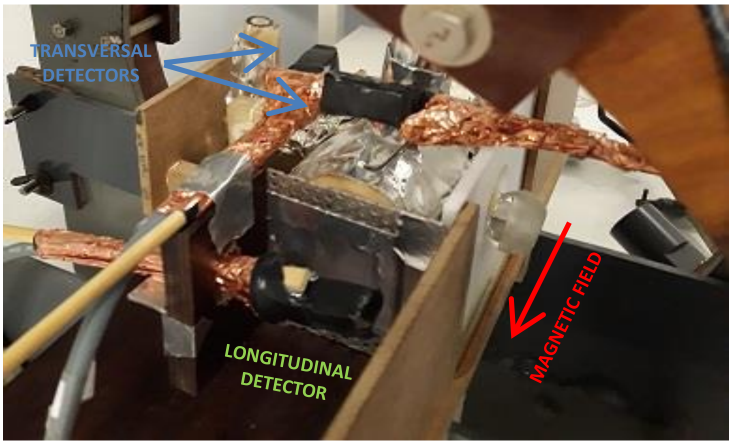

Figure 6.3: Photography of the three CeGAGG located above the glass gas container. This is a preliminary version of the setup, before we included the oven to maximise the heat of the rubidium while reducing the heat irradiation around the detectors. It can be seen the compact size of the detectors which make them perfect to this kind of experiment, because of their ease of placement.

A fully DDAQ was employed, in order to handle large rates with no dead time losses. The system is based in the digitization of the SiPM signals, once shaped to partially integrate them, at 9.5 MS/s per channel, using a 4-channel digital scope (Picoscope 2406B), acquiring in streaming mode, that is, the signal is digitized and continually sent to the PC in triggerless fashion. The PC processes on the fly the pulses from the four detectors. The software employs a pipeline architecture using multiple threads, two threads reading the scope data, another one identifying pulses from the trigger conditions, substracting the baseline, performing the energy integral and writing the binary list-mode event files, and finally another one performing energy histograms, rates and run time plots. As said before, the DAQ was able to acquire about 1 sample every 100 ns, per channel. This was enough to analyze the pulses from the CeGAGG+SiPM combination, which spanned about 1.5 μs, but in the case of LaBr$_3$(Ce) a shaping circuit was employed to stretch the pulses. With this DAQ and detectors combinations, we obtained an energy resolution of about 7.5% and 5% for the 662 keV peak, for CeGAGG and LaBr$_3$(Ce) respectively. The setup could sustain in excess of 70000 counts per seconds in each detector with dead times (coming merely from pulse pile-up) of less than 5%, more than enough for our experiment. Fig. 6.2 shows the arrangement of each detector, the CeGAGG3 and the LaBr$_3$(Ce) were located in the longitudinal line of the magnetic field and the CeGAGG1 and CeGAGG2 are positioned transversely to the field.

Another advantage of our DAQ is that the data is recorded in list mode. The variation of the temperature has negative effect in the SiPMs, because their gain changes almost linearly with temperature. In this experiment, although the oven isolated the detectors from the heat, the continuous flux of air heat needed for vapor generation and the laser heat dissipation increased slowly but continuously the temperature near the oven. This variation induced a shift in the SiPMs gain that also produced a shift in the energy spectra of each detector. As we have all the events recorded as a function of the acquisition time, it is easy to re-calibrate them. The idea is to split the acquisition in time windows of a few seconds and to look whether the energy peaks shift from time to time, in order to correct the shift. An example of this process is shown in Fig. 6.4. Another possible solution to the gain shift was proposed. It consisted of the use of a variable voltage bias source and to change such bias to correct for the SiPMs drift in chain due to temperature variations. This solution implied a more complex electronics and for this reason, we finally chose the online data correction instead.

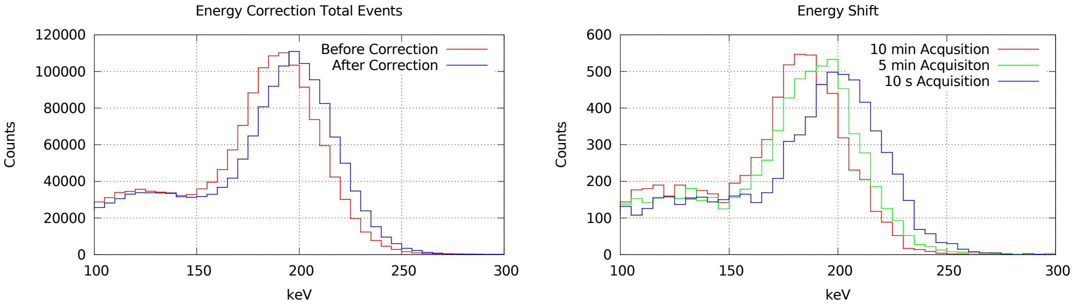

Figure 6.4: Comparison of energy spectra with and without shift correction (right) and the evolution oh the energy shift in function of the time (left). Each spectrum is a five seconds acquisition.

And finally the last test of the detector was to assess their immunity to magnetic fields. SiPM performance is independent on external magnetic fields, but in order to make sure that the γ detectors and their electronics are in no way compromised by the magnetic field, several quick tests were made. In this one, we use a CsI(Tl) of 8x8x30 crystal coupled to one of the S13360-6075CS SiPM mm^3 measuring the energy spectrum of a ^{152}Eu during a few minutes turning the magnetic field on-off. This crystal was used in a fist stage of the experiment, as it was considered a possible candidate for this application, but its long decay constant (1000 ns), wide larger than the CeGAGG constant (88 ns) made us to preferred this second option. In the Fig 6.5 it is shown the vanishingly small effect of the magnetic field on the detectors.

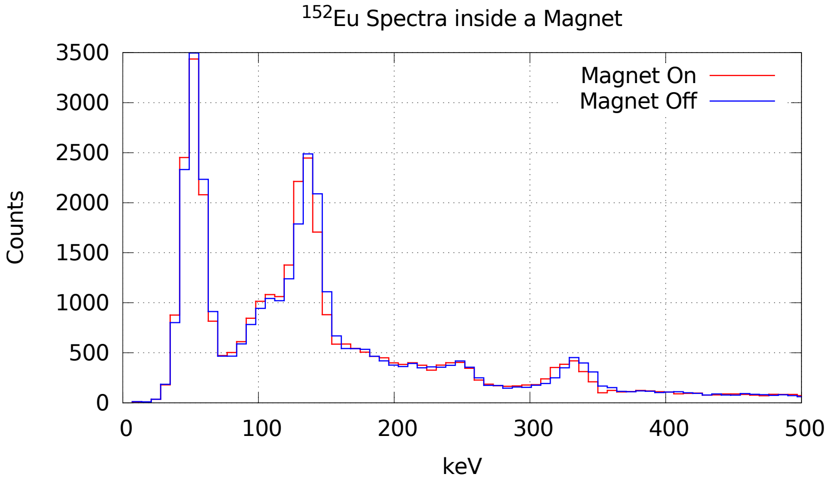

Figure 6.5: Effect on the detector of external magnetic fields. We see that the magnetic field has no effect on the energy spectra obtained with the the detectors.

6.4 Preliminary Acquisitions

A full analysis of the experiment and data obtained can be found in ref.[118, 119]. As a proof of concept of the viability of our DDAQ detector system, we will show the analysis of the geometric dependence for one of the experimental measurements.

As mentioned before, the signal we look for is the variation in counts for a ^{129m}Xe depending on the direction of emission, with respect to the external magnetic beam, in the presence of polarization. In this case we study the variation of anisotropy emission of the 196 keV γ of the ^{129}Xe when we switch on and of a static external magnetic field, not particularly strong. In this experiment, we heat the Rb until around 100º C, moment at which enough quantity of vapor is generated. The Rb is polarized with the laser and the polarization transfer from Rb to ^{129}Xe was initiated by the collisions between the vapor particles and the ^{129m}Xe atoms. The transfer of polarization takes a few seconds [120, 121]. The idea was to identify the anisotropy that should be visible when the spin of ^{129m}Xe aligns with the external magnetic field.

In our case, the counts on the transverse detectors to the magnetic field should increase with respect to the one of the longitudinal detectors. During these tests, When the temperature of the glass was high enough to produce a significant amount of vapor we turn on the laser and we inspect the count rate with the four detectors for 20 minutes without external magnetic field. After these 20 minutes, we turned on the magnetic field and repeat the measurement. Once finished, we repeated the measure without the magnetic field. Several runs of this cycle were repeated.

Fig 6.6 shows the energy spectra for each detector for the 20 minutes of each measurement. These spectra had been generated after correcting for the energy shift due to the continuous temperature increase in the detectors once the oven and the laser are turned on. The three spectra look pretty similar, with small variations in the heights of the peaks, but no change in the asymmetry of the distribution of counts, which would indicate the polarization of the $^{129\mathrm{m}}$Xe was seen, within statistical fluctuations.

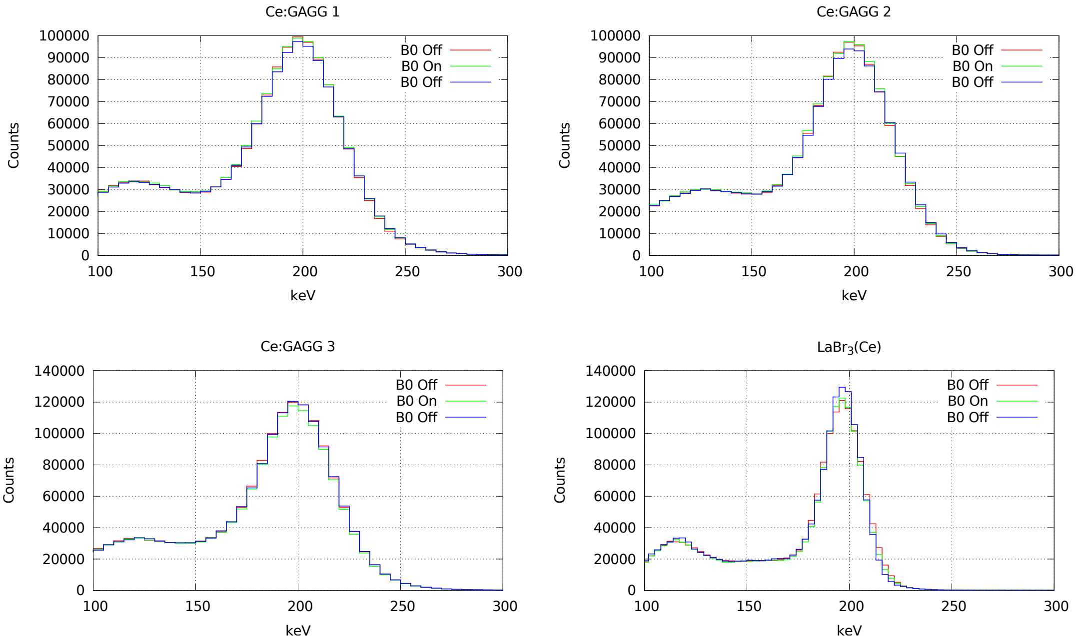

Figure 6.6: Energy spectra of the four detectors for three different conditions

.

In order to understand the lack of polarization, we split the list-mode data into 10 seconds frames. For each subframe, energy windows around the 195 keV peak where set, and we counted the events inside the energy windows. We try to identify the anisotropy by looking for asymmetries using eq. 6.1. In this equation N$_1$ and N$_2$ are the counts in each detector. In Fig. 6.7 shows the evolution of the asymmetries during these 10 s frames. This figure shows that a clear asymmetry between the longitudinal and transverse detectors appears, when the magnetic field is switched on. This did not happen between the detectors that are all of them transverse to the magnetic field. This is a positive indication that at least a small anisotropy of the γ emission is present, and thus some degree of polarization of the nuclei is induced.

$$A = \frac{N_1 - N_2}{N_1 + N_2} \tag{6.1}$$

In the table 6.1 we show the variation of the asymmetry. Due to differences in efficiency,

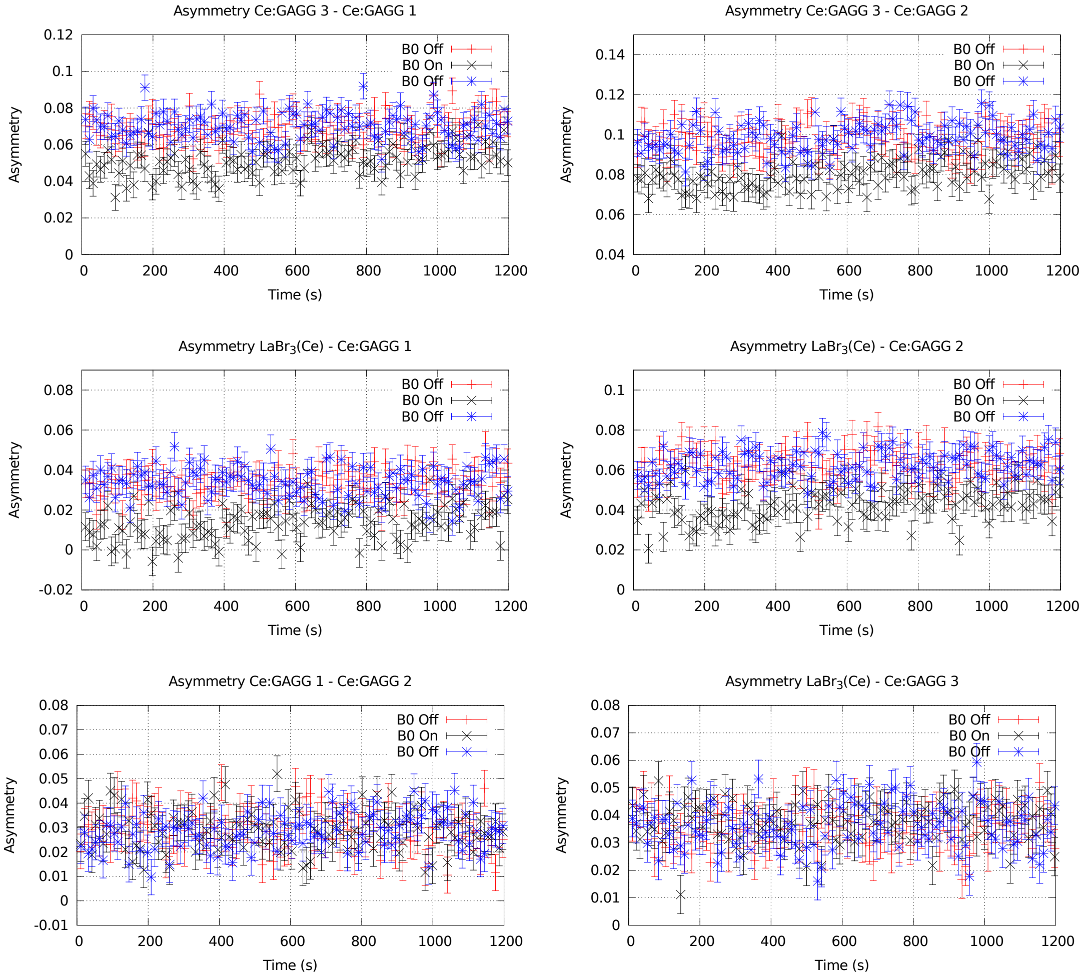

Figure 6.7: Evolution of the asymmetries in function of the time

.

placement and gain among the detectors, the asymmetry with no field is not exactly zero, what we seek is for a variation of the asymmetry with field off and on. We can observe that the asymmetry change by 20% to 50%, depending on the detectors pair inspected. This change only appears in the combination of a longitudinal detector with a transverse one. In the combination of detectors in the same transverse plane to the magnetic field there is not a change that can be observe, within the statistical errors. This number reaffirms the idea that we have found a clear asymmetry when the polarized gas is aligned.

Detectors	B0 Off	B0 On	B0 Off
Ce:GAGG 3 - Ce:GAGG 1	$(6.9 \pm 0.1)\cdot 10^{-2}$	$(5.2 \pm 0.1)\cdot 10^{-2}$	$(7.0 \pm 0.1)\cdot 10^{-2}$
Ce:GAGG 3 - Ce:GAGG 2	$(9.8 \pm 0.1)\cdot 10^{-2}$	$(8.0 \pm 0.1)\cdot 10^{-2}$	$(9.9 \pm 0.1)\cdot 10^{-2}$
Ce:GAGG 1 - Ce:GAGG 2	$(2.9 \pm 0.1)\cdot 10^{-2}$	$(2.9 \pm 0.1)\cdot 10^{-2}$	$(2.6 \pm 0.1)\cdot 10^{-2}$
$LaBr_3$(Ce) - Ce:GAGG 1	$(3.3 \pm 0.1)\cdot 10^{-2}$	$(1.4 \pm 0.1)\cdot 10^{-2}$	$(3.4 \pm 0.1)\cdot 10^{-2}$
$LaBr_3$(Ce) - Ce:GAGG 2	$(6.2 \pm 0.1)\cdot 10^{-2}$	$(4.3 \pm 0.1)\cdot 10^{-2}$	$(6.2 \pm 0.1)\cdot 10^{-2}$
$LaBr_3$(Ce) - Ce:GAGG 3	$(3.6 \pm 0.1)\cdot 10^{-2}$	$(3.8 \pm 0.1)\cdot 10^{-2}$	$(3.6 \pm 0.1)\cdot 10^{-2}$

Table 6.1: Average asymmetries for every possible detector combinations with and without magnetic field.

6.5 Discussion

The results of the experiment are preliminary and are still under analysis. Although in principle we expected a large asymmetry, larger than 40% asymmetries are reported in previous experiments [111, 110], one has to take into account that we are dealing with a different isotope of Xenon, with a larger magnetic moment and in this case the maximum polarization/alignment which can be obtained would be reduced. In the experiment we also lacked independent information about the degree of polarization reached in the nuclei, as in other experiments the process is performed inside a MRI or with an MRI setup, with RF and coils which allow to measure the polarization of the nuclei. Further, the shift in gain of the detectors when the oven and laser was on, made it difficult to perform longer runs which would introduce smaller statistical errors. However, as explained before, our role in this experiment had to do with the detector, DDAQ development and test. In this regards, we developed an online and an offline version of the analysis software. These were essential tools during the experiment. The software could deal with the data from the four detectors, in streaming mode, thus no electronics and processing dead-time was involved at these rates. Pulses were processed, gain-scaled to correct for the gain shift, baseline-subtraction, and energy integrated, with histograms of energy and rates being displayed every couple of seconds on the screen, while time-stamped events were dumped into the disk of the computer, which was being controlled remotely. The energy resolution obtained was good enough, although we hope to improve it in the future with larger SiPM arrays. In this regards the test of the DDAQ and detectors were very satisfactory and a lot of experience has been gained for the future. This experiment is the core of a proposal submitted to the UE as an open FET call last june, 2020, and that we have just learned that it has been approved.

6.6 Conclusion

The preliminary tests of our detectors and DDAQ for the $\gamma-$MRI experiment in ^{129m}Xe was very promising, we were able to deploy a system with high rate capabilities, within a compact size and that it is fully immune to the effects of magnetic field. This make it possible to place the detectors close to the region of interest, and thus to obtain increased sensitivity and even during high data rate. Better temperature control or insulation from the heat in the glass bowl would be desirable, though.

Conclusions of this thesis

In this thesis we have studied fully digital DAQ systems, or DDAQ, that is, data acquisition systems where the signal from the detectors is digitized as close to where it is generated as possible, and pulse shaping and processing is performed *in silico*, instead of the conventional approach, where the signals from the detector are amplified and shaped by analog circuits before being read by the ADC.

In the first part of this thesis, this digital procedure has proven to perform equally well or even better than highly optimized analogue equivalent systems [31, 32, 33, 34] in determingin both the energy and the time stamp of detections in nuclear radiation systems, and it has the advantage of lacking physical constrains in the shaping and processing of the pulses, being the flexibility of the software the unique limitation. We have shown in chapter 2 that the use of machine learning strategies for the optimization of the relevant parameters of the algorithms provides excellent results, which can outperform, for the same detectors, the best results of the conventional DAQ. Indeed in chapter 3 we have also seen that the genetic algorithm (GA) could be a universal scheme to find the best possible filter and shaping algorithm in many situations. In all, we have illustrated the applicability of the GA to three different setups, including a new scintillator crystal made of $\mathrm{LaBr_3(Ce+Sr)}$, and a PA3325-WB-0808 SiPM matrix used as photodetector coupled to a standard $\mathrm{LaBr_3(Ce)}$ crystal. The GA optimized the parameters of the filter and shapers without human intervention, outperforming the best results of the conventional DAQ approach. The main reasons for the improvement lies in that the DDAQ allows to change and reanalyze the acquired data with many different filters and algorithms, until the best results for energy and time are found.

In the second part of this thesis we focus less in obtaining the best determination of energy and time, but on the ability of handling high rates, and on the low cost and ease of deployment allowed by the DDAQ strategies. It has been shown in chapters 4 to 6, the viability of our system to handle large count rates while maintaining very usable energy and time information. We evaluated very inexpensive, compact and versatile compact based on USB digital scopes. Our results were limited by the computing power of the notebook employed, and with more powerful computers the maximum event rates can be much higher. These results opens the door to very simple DDAQ systems suitable for complex experiments, demanding in count rate. Indeed, we foresee that with a much more powerful computer (10 cores instead of two, for instance), we would saturate the counting ability of detectors with the stretched pulses up to 1 us, being able of recording several million counts across four detectors altogether, more than enough for the application in protontherapy, PET and γ-MRI imaging discussed in this thesis. Our results have convinced our group to initiate the acquisition of high end (and high cost) digitizers and computers to systematically replace our conventional DAQ.

We will finalize this concluding chapter with a free personal reflectoins. Any group working in experimental nuclear physics for a decade or two, as it is the GFN, will have shelves full of NIM and VME modules for preamplifiers, fast amplifiers, spectroscopy amplifiers, TDCs, TACs, scalers, ADCs, coincidence units, CFDs, fan-in fan-outs, etc., etc. They will probably be worth in the >50 k€. There are many chances that some of the modules have been used only a couple times. They are bulky and setting up an experiment with them is a lengthy operation, provided the crates are available. Yet it is a well proven technology which has been around for longer than 50 years, researchers around the world know how to use them and, provided you have enough number and variety of modules, they are a versatile and powerful way of setting up nuclear physics experiments. And so we did, in experiments at ISOLDE, ILL and CMAM..., in which as a PhD student the author of this thesis was involved, including bringing many modules in the suitcases while traveling to the experiment, and witnessing the classical approach at play. It works. It is solid. We know how to make it very performing. But it is based on very specialized equipment, only a couple of companies are still designing and producing them, they are very expensive and they do not evolve fast at all. The community of users is small and with relatively deep pockets.

On the other hand, we live, more and more, in a digital world. Our mobile phones and computer analog signals are continuously digitized and sent away in digital form, and vice-versa, and in our TVs streaming digital content is converted in analog levels on the screens. ADC and DAC chips are everywhere, with enhanced resolution (more bits), lower power consumption, smaller size, shrinking costs and faster sampling speeds. They are used by billions of people all over the world, and they are improving as we speak, growing intelligence and large attached memories. Digital data acquisition in nuclear physics is becoming not only a possibility but rather a necessity. Old players in the NIM game, such as CAEN, have moved many of its products into the fully digital realm. We have tested some of them and they deliver, are simple to use, not incredibly expensive compared to the conventional equivalent, and flexible enough if the built-in algorithms in their FPGA suit your needs. We have purchased already several of these improved digitizers and plan to acquire several more. But in the case you need to reprogram the FPGAs, a different, much higher level of complexity will be involved, requiring the skills of personnel specifically trained in FPGA and ASICs, which is not always available if the nuclear physics group is not very large.

The alternative are high performing digitizers (>12 bits, >2 Gs/s) or oscilloscopes coupled to an industry standard PC. Still relatively inexpensive and much more flexible, if you are willing to code digital processing algorithms in the computer from scratch. With these components and a few (or many) hours spent in front of the computer, it is possible to obtain for instance timing resolution of our fast-timing detectors that outperform the already highly optimized, world record figures in its class, of the conventional analog DAQ. Even more, the optimization, characterization and calibration of the parameters, typical of CFD-based DAQ for timing measurements, in order for instance to correct for time walk, can easily take several days. But with the fully DDAQ, we can let the computer do the task for us. It may still take one night, but it can be all done by the computer provided with a machine learning strategy. In our case we employed a Genetic Algorithm, a trademark of our group. Future large-scale projects in which the GFN is involved, such as the Fast-Timing Array FATIMA, will for sure take the DDAQ path sooner than later. The knowledge gained in this thesis will allow us to keep in the forefront of this transition into the digital domain.

But nuclear physics experiments can also go digital the cheap way. This thesis reports on a generation of fully digital acquisition systems designed and employed by the GFN for over five years. We can say for sure that many, if not all, the experiments described in the second part of this thesis would not have been possible without the effort spent by the group, and in particular during this PhD work, in the development of the experience, hardware and software to implement a DDAQ for these experiments. The resulting setups are compact and inexpensive. Consider that you can have a 8-bit scope able of 1 Gs/s sampling for less than 100 €, although a 250-€unit would be advisable in order to have a fast connection with the PC.

This exploration has already identified some points to improve, such as replacing the RC-CR pulse stretchers by gated integrators, task which rest in our roofs, but that is not complicated at all. Another point to improve is the bottleneck of the communication between the digitizer and the computer. But this, relying on industry standards for commodity appliances, is being solved on its own as we speak. Improved USB and other communication protocols already exist and soon, without intervention from our part, the communications narrow path will be a highway.

Then we will focus on the other weak element of the DDAQ chain: the computer which processes the data. In our former tests, we used a small notebook with an SSD, a very modest CPU and small amount of memory. The number of events was limited to around 400 kevents/s, aggregated. Recently we have trade in a slightly more powerful yet very compact computer, and the speed increased by 50%. Computers are evolving fast, and they are inexpensive. We can use GPUs to process the signals. The only other ingredient we will need in order to take full advantage of more powerful CPUs, communications and digitizers, is the experience, the algorithms and the codes. And these we already have them. The work presented here paved the way for a digital GFN. Full replacement of conventional, NIM based, DAQ in nuclear experiments is not yet here for every application, but it is not far away, specially for small setups with a few detectors.

Finally, the next step in our move into digital street will be the purchase of several very high-performing digitizing cards for the PC (above 10 k€each, 12 bits or more, 1 Gs/s or more), which will benefit from the very fast PCIe and PCIX links to send the data in streaming mode at maximum sampling rate. They are still a bit more expensive than the NIM-based alternative, on a per channel basis, but surely they will compete soon, specially for setups with many detectors when we want to achieve the maximum performance, where scale economy or agreements with the vendors to lower the prices when many identical units are purchased, may lower costs.

Appendix A

Main contributions of this thesis

While this PhD. thesis was being carried out, partial results have been presented in publications in international journals and relevant conferences in the field. The contributions derived from this thesis are presented in the following list.

A.1 Published articles in indexed international journals

1. **V. Sanchez-Tembleque**, V. Vedia, L.M. Fraile, S. Ritt, J.M. Udias, Optimizing time-pickup algorithms in radiation detectors with a genetic algorithm, *Nuclear Instruments and Methods in Physics Research Section A: Accelerators, Spectrometers, Detectors and Associated Equipment*, 927(54-62), 2019

2. **V. Sanchez-Tembleque**, D. Sanchez-Parcerisa, V. Valladolid-Onecha, L. M. Fraile, J. M. Udias, Simultaneous measurement of the spectral and temporal properties of a LINAC pulse from outside the treatment room, textit"Radiation Physics and Chemistry, 158(1-5), 2019

3. L.M. Fraile, **V. Sanchez-Tembleque**, J. Benito, M. García-Díez, J.M. Udías, V. Vedia, Advanced scintillators for fast-timing applications, *Nuclear Instruments and Methods in Physics Research Section B: Beam Interactions with Materials and Atoms*, 463(394-397), 2020

4. J. Sánchez-Jiménez, A. Lopez-Montes, L. Núñez-Martínez, A. Villa-Abaunza, L. M. Fraile, **V. Sanchez-Tembleque**, J. M. Udias, 223Ra-dichloride spectrometric characterization: Searching for the presence of long-lived isotopes with radiological protection implications, *European Journal of Medical Physics*, 35(97-101), 2017

5. R. Lică, G. Benzoni, A. I. Morales, M. J. G. Borge, L. M. Fraile, H. Mach, M. Madurga, C. Sotty, V. Vedia, H. De Witte, J. Benito, T. Berry, N. Blasi, A. Bracco, F. Camera, S. Ceruti, V. Charviakova, N. Cieplicka-Oryńczak, C. Costache, F. C. L. Crespi, J. Creswell, G. Fernández-Martínez, H. Fynbo, P. Greenlees, I. Homm, M. Huyse, J. Jolie, V. Karayonchev, U. Köster, J. Konki, T. Kröll, J. Kurcewicz, T. Kurtukian-Nieto, I. Lazarus, S. Leoni, M. Lund, N. Marginean, R. Marginean, C. Mihai, R. Mihai, A. Negret, A. Orduz, Z. Patyk, S. Pascu, V. Pucknell, P. Rahkila, J. M. Regis, F. Rotaru, N. Saed-Sami, **V. Sanchez-Tembleque**, M. Stanoiu, O. Tengblad, M. Thuerauf, A. Turturica, P. Van Duppen, N. Warr. β decay studies of n-rich Cs isotopes with the ISOLDE Decay Station, *Journal of Physics G: Nuclear and Particle Physics*, 44, 2017

6. D. Sanchez-Parcerisa, O. Giza, J. Camacho, **V. Sanchez-Tembleque**, S. Avery, J. Udias, EP-1734: Photo- and proto- acoustic dose monitoring in radiosurgery and proton beams, *Radiotherapy and Oncology*, 127 , 2018

7. R. Lică, G. Benzoni, T. R. Rodríguez, M. J. G. Borge, L. M. Fraile, H. Mach, A. I. Morales, M. Madurga, C. O. Sotty, V. Vedia, H. De Witte, J. Benito, R. N. Bernard, T. Berry, A. Bracco, F. Camera, S. Ceruti, V. Charviakova, N. Cieplicka-Oryńczak, C. Costache, F. C. L. Crespi, J. Creswell, G. Fernez-Martínez, H. Fynbo, P. T. Greenlees, I. Homm, M. Huyse, J. Jolie, V. Karayonchev, U. Köster, J. Konki, T. Kröll, J. Kurcewicz, T. Kurtukian-Nieto, I. Lazarus, M. V. Lund, N. Mărginean, R. Mărginean, C. Mihai, R. E. Mihai, A. Negret, A. Orduz, Z. Patyk, S. Pascu, V. Pucknell, P. Rahkila, E. Rapisarda, J. M. Regis, L. M. Robledo, F. Rotaru, N. Saed-Samii, V. **Sanchez-Tembleque**, M. Stanoiu, O. Tengblad, M. Thuerauf, A. Turturica, P. Van Duppen, N. Warr. Evolution of deformation in neutron-rich Ba isotopes up to $A = 150$., *Phys. Rev. C*, 97, 2018.

8. O. M. Giza, D. Sanchez-Parcerisa, **V. Sanchez-Tembleque**, J. L. Herraiz, J. Camacho, S. Avery, J. M. Udias, Photoacoustic dose monitoring in clinical high-energy photon beams, *Biomedical Physics & Engineering Express*, 5.3(28-35), 2019

9. M. Piersa, A. Korgul, L. M. Fraile, J. Benito, E. Adamska, A. N. Andreyev, R. Álvarez-Rodríguez, A. E. Barzakh, G. Benzoni, T. Berry, M. J. G. Borge, M. Carmona, K. Chrysalidis, J. G. Correia, C. Costache, J. G. Cubiss, T. Day Goodacre, H. De Witte, D. V. Fedorov, V. N. Fedosseev, G. Fernéz-Martínez, A. Fijałkowska, M. Fila, H. Fynbo, D. Galaviz, P. T. Greenlees, R. Grzywacz, L. J. Harkness-Brennan, C. Henrich, M. Huyse, A. Illana, Z. Janas, K. Johnston, D. S. Judson, V. Karanyonchev, M. Kicińska-Habior, J. Konki, J. Kurcewicz, I. Lazarus, R. Lică, H. Mach, M. Madurga, I. Marroquín, B. Marsh, M. C. Martínez, C. Mazzocchi, N. Mărginean, R. Mărginean, K. Miernik, C. Mihai, E. Nácher, A. Negret, B. Olaizola, R. D. Page, S. Paulaskalas, S. Pascu, A. Perea, V. Pucknell, P. Rahkila, E. Rapisarda, J.-M. Régis, F. Rotaru, S. Rothe, **V. Sanchez-Tembleque**, G. Simpson, Ch. Sotty, L. Stan, M. Stănoiu, M. Stryjczyk, O. Tengblad, A. Turturica, J. M. Udías, P. Van Duppen, V. Vedia, A. Villa, S. Viñals, R. Wadsworth, W. B. Walters, N. Warr. β decay of ^{133}In: γ emission from neutron-unbound states in ^{133}Sn, *Phys. Rev. C*,

99, 2019

10. R. L. Canavan, M. Rudigier, P. H. Regan, M. Lebois, J. N. Wilson, N. Jovancevic, P.-A. Söderström, S. M. Collins, D. Thisse, J. Benito, S. Bottoni, M. Brunet, N. Cieplicka-Oryńczak, S. Courtin, D. T. Doherty, L. M. Fraile, K. Hadyńska-Klęk, G. Häfner, M. Heine, W. Iskra, Ł. V. Karayonchev, A. Kennington, P. Koseoglou, G. Lotay, G. Lorusso, M. Nakhostin, C. R. Niţă, S. Oberstedt, Zs. Podolyák, L. Qi, J.-M. Régis, **V. Sánchez-Tembleque**, R. Shearman, V. Vedia, W. Witt. Half-life measurements in ^{164,166}Dy using $\gamma-\gamma$ fast-timing spectroscopy with the ν-Ball spectrometer, *Phys. Rev. C*, 101:024313, (2020).

11. M. Rudigier, P.M. Walker, R.L. Canavan, Zs.Podolyák, P.H. Regan, P.-A. Söderström, M. Lebois, J.N. Wilson, N. Jovancevic, A. Blazhev, J. Benito, S. Bottoni, M. Brunet, N. Cieplicka-Oryńczak, S. Courtin, D.T. Doherty, L.M. Fraile, K. Hadynska-Klek, M. Heine, Ł.W. Iskra, J. Jolie, V. Karayonchev, A. Kennington, P. Koseoglou, G. Lotay, G. Lorusso, M. Nakhostin, C.R. Nita, S. Oberstedt, L. Qi, J.-M. Régis, **V. Sánchez-Tembleque**, R. Shearman, W. Witt, V. Vedia, K.O. Zell. Multi-quasiparticle sub-nanosecond isomers in ^{178}W, *Physics Letters B*, 801, 2020.

12. J. Benito, L. M. Fraile, A. Korgul, M. Piersa, E. Adamska, A. N. Andreyev, R. Álvarez-Rodríguez, A. E. Barzakh, G. Benzoni, T. Berry, M. J. G. Borge, M. Carmona, K. Chrysalidis, C. Costache, J. G. Cubiss, T. Day Goodacre, H. De Witte, D. V. Fedorov, V. N. Fedosseev, G. Fern;ez-Martínez, A. Fijałkowska, M. Fila, H. Fynbo, D. Galaviz, P. Galve, M. García-Díez, P. T. Greenlees, R. Grzywacz, L. J. Harkness-Brennan, C. Henrich, M. Huyse, P. Ibáñez, A. Illana, Z. Janas, J. Jolie, D. S. Judson, V. Karayonchev, M. Kicińska-Habior, J. Konki, J. Kurcewicz, I. Lazarus, R. Lică, A. López-Montes, M. Lund, H. Mach, M. Madurga, I. Marroquín, B. Marsh, M. C. Martínez, Mazzocchi, C. N. Mărginean, R. Mărginean, K. Miernik, C. Mihai, R. E. Mihai, E. Nácher, A. Negret, B. Olaizola, R. D. Page, S. V. Paulauskas, S. Pascu, A. Perea, V. Pucknell, P. Rahkila, C. Raison, E. Rapisarda, J.-M. Régis, K. Rezynkina, F. Rotaru, S. Rothe, D. Sánchez-Parcerisa, **V. Sanchez-Tembleque**, K. Schomacker, G. S. Simpson, Ch. Sotty, L. Stan, M. Stănoiu, M. Stryjczyk, O. Tengblad, A. Turturica, J. M. Udías, P. Van Duppen, V. Vedia, A. Villa-Abaunza, S. Viñals, W. B. Walters, R. Wadsworth, N. Warr. Detailed spectroscopy of doubly magic ^{132}Sn. *Phys. Rev. C, 102*, 2020.

A.2 Conference proceedings published in indexed international journals

1. **V. Sanchez-Tembleque**, L. M. Fraile, V. Vedia, M. Carmona, K. Kamada, Y. Shoji, A. Yoshikawa, J. M. Udias, Evaluation of inorganic scintillators for high performance ToF PET applications, *2015 IEEE Nuclear Science Symposium Conference Record*

2. **V. Sanchez-Tembleque**, V. Vedia, M. Carmona, L. M. Fraile, S. Ritt, J. M. Udías, Digital strategies for time and energy measurement for ultra fast scintillators, *2016 IEEE Nuclear Science Symposium Conference Record*

3. **V. Sanchez-Tembleque**, L. M. Fraile J. M. Udías, Time Over Threshold Data Acquisition System for PET, *2017 IEEE Nuclear Science Symposium Conference Record*

4. **V. Sanchez-Tembleque**, V. Vedia, L. M. Fraile, J. M. Udías, Optimizing Time-Pickup Algorithms in Radiation Detectors with a Genetic Algorithm, *2017 IEEE Nuclear Science Symposium Conference Record*

5. M. Garcia-Diez, **V. Sanchez-Tembleque**, L. M. Fraile, S. Ritt, J. M. Udías, High energy resolution inorganic scintillators read by SiPM arrays, *2019 IEEE Nuclear Science Symposium Conference Record*

6. M. Piersa, A. Korgul, L.M. Fraile, J. Benito, E. Adamska, R. Álvarez-Rodríguez, A.E. Barzakh, G. Benzoni, T. Berry, M.J.G. Borge, M. Carmona, K. Chrysalidis, G. Correia, C. Costache, T. Day Goodacre, D.V. Fedorov, V.N. Fedosseev, G. Fernández-Martínez, M. Fila, D. Galaviz, R. Grzywacz, C. Henrich, A. Illana, Z. Janas, K. Johnston, V. Karanyonchev, M. Kicińska-Habior, R. Lică, M. Madurga, I. Marroquín, B. Marsh, C. Martínez, C. Mazzocchi, K. Miernik, R. Mihai, B. Olaizola, S. Paulaskalas, J.-M. Rǵis, S. Rothe, **V. Sanchez-Tembleque**, G. Simpson, Ch. Sotty, L. Stan, M. Stănoiu, M. Stryjczyk, A. Turturica, J.M. Udías, V. Vedia, A. Villa, W.B. Walters. Investigation of Low-lying States in ^{133}Sn Populated in the β Decay of ^{133}In Using Isomer-selective Laser Ionization. *Acta Phys. Pol. B*, 49, 2018

7. E. Adamska, A. Korgul, A. Fijałkowska, K. Miernik, M. Piersa, R. Canavan, D. Etasse, N. Jovančević, M. Lebois, M. Rudigier, D. Thisse, J.N. Wilson, P. Adsley, A. Algora, M. Babo, K. Belvedere, J. Benito, A. Blazhev, G. Benzoni, A. Boso, S. Bottoni, M. Bunce, R. Chakma, N. Cieplicka-Oryńczak, M. Ciemała, S. Collins, L. Cortés, P. Davies, C. Delafosse, M. Fallot, B. Fornal, L.M. Fraile, R.-B. Gerst, D. Gjestvang, A. Gottardo, V. Guadilla, G. Hafner, K. Hauschild, M. Heine, C. Henrich, I. Homm, F. Ibrahim, Ł.W. Iskra, P. Koseoglou, T. Kröll, T. Kurtukian-Nieto, L. Le-meur, S. Leoni, J. Ljungvall, A. Lopez-Martens, R. Lozeva, I. Matea, J. Nemer, S. Oberstedt, W. Paulsen, Y. Popovitch, L. Qi, D. Ralet, P.H. Regan, D. Reygadas Tello, K. Rezynkina, **V. Sanchez-Tembleque**, C. Schmitt, P.-A. Söderström, C. Surder, G. Tocabens, V. Vedia, D. Verney, N. Warr, B. Wasilewska, J. Wiederhold, M. Yavahchova, F. Zeiser. γ-ray Spectroscopy of ^{85}Se Produced in ^{232}Th Fission. *Acta Phys. Pol. B*, 51, (2020).

A.3 Works presented in international or national conferences

Authors: **V. Sanchez-Tembleque**, L. M. Fraile, V. Vedia, M. Carmona, K. Kamada, Y. Shoji, A. Yoshikawa, J. M.Udias

Title: Evaluation of inorganic scintillators for high performance ToF PET applications
Type of presentation: Poster
Congress: 2015 IEEE Nuclear Science Symposium and Medical Imaging Conference
Place and date: San Diego, USA, 31 Oct - 7 Nov, 2015

Authors: **V. Sanchez-Tembleque**, V. Vedia, M. Carmona, L. M. Fraile, S. Ritt, J. M. Udías
Title: Digital strategies for time and energy measurement for ultra fast scintillators
Type of presentation: Poster
Congress: 2016 IEEE Nuclear Science Symposium and Medical Imaging Conference
Place and date: Strasbourg, France, 29 Oct - 6 Nov, 2016

Authors: **V. Sanchez-Tembleque**, V. Vedia, M. Carmona, L. M. Fraile, S. Ritt, J. M. Udías
Title: Análisis digital para medidas de tiempo y energía con centelladores ultra rápidos
Type of presentation: Oral
Congress: VIII CPAN Days
Place: Zaragoza, Spain, 28-30 Nov, 2016

Authors: **V. Sanchez-Tembleque**, D. Sanchez-Parcerisa, L. M. Fraile, J. M. Udías
Title: Medida simultánea del espectro y el perfil temporal del pulso de un LINAC desde fuera de la sala
Type of presentation: Poster
Congress: V Congreso Conjunto SEFM-SEPR
Place: Girona, Spain, 13-16 Jun, 2017

Authors: **V. Sanchez-Tembleque**, V. Vedia, L. M. Fraile, J. M. Udías
Title: Optimizing Time-Pickup Algorithms in Radiation Detectors with a Genetic Algorithm
Congress: XXXVI Reunión Bienal de la RSEF
Place: Santiago de Compostela, Spain, 17-21 Jul, 2017

Authors: **V. Sanchez-Tembleque**, D. Sanchez-Parcerisa, L. M. Fraile, J. M. Udías
Title: Medida simultánea del espectro y el perfil temporal del pulso de un LINAC desde fuera de la sala
Type of presentation: Poster
Congress: XXXVI Reunión Bienal de la RSEF
Place: Santiago de Compostela, Spain, 17-21 Jul, 2017

Authors: **V. Sanchez-Tembleque**, V. Vedia, L. M. Fraile, J. M. Udías
Title: Optimizing Time-Pickup Algorithms in Radiation Detectors with a Genetic Algorithm
Type of presentation: Poster

Congress: XIV International Conference on Scintillating Materials and their Applications
Place: Chamonix, France, 18-22 Sept, 2017

Authors: **V. Sanchez-Tembleque**, L. M. Fraile, J. M. Udías
Title: Time over Threshold Data Acquisition System for PET
Type of presentation: Poster
Congress: 2017 IEEE Nuclear Science Symposium and Medical Imaging Conference
Place: Atlanta, EEUU, 21-28 Oct, 2017

Authors: **V. Sanchez-Tembleque**, V. Vedia, L. M. Fraile, J. M. Udías
Title: Optimizing Time-Pickup Algorithms in Radiation Detectors with a Genetic Algorithm
Type of presentation: Poster
Congress: 2017 IEEE Nuclear Science Symposium and Medical Imaging Conference
Place: Atlanta, EEUU, 21-28 Oct, 2017

Authors: **V. Sanchez-Tembleque**, M. Garcia-Diez L. M. Fraile, J. M. Udías
Title: Evaluation of Large Monoholitic LaBr3(Ce,Sr) Scintillators for Timing and Energy Resolution
Type of presentation: Poster
Congress: 2018 IEEE Nuclear Science Symposium and Medical Imaging Conference
Place: Sidney, Australia, 1-17 Nov, 2018

Authors: **V. Sanchez-Tembleque**, M. Garcia-Diez, L. M. Fraile, J. M. Udias
Title: Characterization of scintillator crystals using current SiPMS arrays
Type of presentation: Oral
Congress: XXXVII Reunión Bienal de la RSEF
Place: Zaragoza, Spain, 15-21 Jul, 2018

Authors: **V Sanchez-Tembleque**, C. M. Backer, C. Baumer, J. Benito, S. España, A. Espinosa, L.M. Fraile, P. Galve, M. Garcia-Diez, J.L. Herraiz, P. Ibañez, D. Sánchez-Parcerisa, A. Shagalakova, B. Timmermann, J. M. Udias, V. Valladolid-Onecha, V. Vedia
Title: Activation of Contrast Agents for Range Verification in Proton Therapy
Type of presentation: Oral
Congress: XXXVII Reunión Bienal de la RSEF
Place: Zaragoza, Spain, 15-21 Jul, 2018

Authors: M. Garcia-Diez, **V. Sanchez-Tembleque**, L. M. Fraile, J. M. Udías
Title: High energy resolution inorganic scintillators read by SiPM arrays
Type of presentation: Poster
Congress: 2019 IEEE Nuclear Science Symposium and Medical Imaging Conference
Place: Manchester, UK, 26 Oct - 2 Nov, 2018

Authors: **V. Sanchez-Tembleque**, S. España, A. Espinosa, L. M. Fraile, M. Garcia-Diez, C. Gutierrez-Neira, P.Ibañez, D. Sanchez-Parcerisa, V. Valladolid-Onecha, J. M. Udias
Title: Design of a Digital Data Acquisition System for the Study of Prompt Gamma-Rays from Contrast Agents in Protontherapy
Type of presentation: Oral (Accepted)
Congress: 2020 IEEE Nuclear Science Symposium and Medical Imaging Conference
Place: Boston, EEUU (online Conference), 31 Oct - 7 Nov, 2020

List of Figures

List of Tables

Bibliography

[1] Kenneth S Krane. *Introductory nuclear physics.* Wiley, New York, NY, 1988.

[2] Willian R. Leo. *Techniques for Nuclear and Particle Physics Experiments.* Springer, Berlin, Heidelberg, Berlin/Heidelberg/New York, 1994.

[3] Simon R. Cherry, James A. Sorenson, and Michael E. Phelps. chapter 1 - what is nuclear medicine? In Simon R. Cherry, James A. Sorenson, and Michael E. Phelps, editors, *Physics in Nuclear Medicine (Fourth Edition)*, pages 1 – 6. W.B. Saunders, Philadelphia, fourth edition edition, 2012.

[4] G. F. Knoll. *Radiation Detection and Measurement 3rd ed.* Wiley, New York, NY, 2000.

[5] G. Bizarri. Scintillation mechanisms of inorganic materials: From crystal characteristics to scintillation properties. *Journal of Crystal Growth*, 312(8):1213 – 1215, 2010. The 17th American Conference on Crystal Growth and Epitaxy/The 14th US Biennial Workshop on Organometallic Vapor Phase Epitaxy/The 6th International Workshop on Modeling in Crystal Growth.

[6] M. Moszyński. Inorganic scintillation detectors in γ-ray spectrometry. *Nuclear Instruments and Methods in Physics Research Section A: Accelerators, Spectrometers, Detectors and Associated Equipment*, 505(1):101 – 110, 2003. Proceedings of the tenth Symposium on Radiation Measurements and Applications.

[7] G Bondarenko, P Buzhan, B Dolgoshein, V Golovin, E Guschin, A Ilyin, V Kaplin, A Karakash, R Klanner, V Pokachalov, E Popova, and K Smirnov. Limited geiger-mode microcell silicon photodiode: new results. *Nuclear Instruments and Methods in Physics Research Section A: Accelerators, Spectrometers, Detectors and Associated Equipment*, 442(1):187 – 192, 2000.

[8] P. Buzhan, B. Dolgoshein, L. Filatov, A. Ilyin, V. Kantzerov, V. Kaplin, A. Karakash, F. Kayumov, S. Klemin, E. Popova, and S. Smirnov. Silicon photomultiplier and its possible applications. *Nuclear Instruments and Methods in Physics Research Section A:*

Accelerators, Spectrometers, Detectors and Associated Equipment, 504(1):48 – 52, 2003. Proceedings of the 3rd International Conference on New Developments in Photodetection.

[9] Fabio Acerbi and Stefan Gundacker. Understanding and simulating sipms. *Nuclear Instruments and Methods in Physics Research Section A: Accelerators, Spectrometers, Detectors and Associated Equipment*, 926:16 – 35, 2019. Silicon Photomultipliers: Technology, Characterisation and Applications.

[10] Carlo Tintori. *WP2081 Digital Pulse Processing in Nuclear Physics.* CAEN, 2.1 edition, 2011.

[11] R. W. Hamming. *Digital Filters.* Prentice Hall, Englewood Cliffs, N.J, 1998.

[12] CAEN. `https://caen.it/`.

[13] NUTAQ. `https://nutaq.com/`.

[14] Alazartech PCI Digitizers. `http://alazartech.com`.

[15] Acquitek. `http:acquitek.com/`.

[16] XIA. `https://xia.com/`.

[17] Grupo de Fisica Nuclear, Unviersidad Complutense de Madrid. `http://nuclear.fis.ucm.es`.

[18] H. Mach, R.L. Gill, and M. Moszyński. A method for picosecond lifetime measurements for neutron-rich nuclei: (1) outline of the method. *Nuclear Instruments and Methods in Physics Research Section A: Accelerators, Spectrometers, Detectors and Associated Equipment*, 280(1):49 – 72, 1989.

[19] FATIMA - FAst TIMing Array Project. `http://nuclear.fis.ucm.es/fasttiming/`.

[20] Isotope Separator On Line DEvice (ISOLDE). `https://isolde.web.cern.ch/`.

[21] Institut Laue–Langevin (ILL). `https://ill.eu/`.

[22] Laboratori Nazionali di Legnaro (LNL). `https://lnl.infn.it/`.

[23] V. Sanchez-Tembleque, V. Vedia, L.M. Fraile, S. Ritt, and J.M. Udias. Optimizing time-pickup algorithms in radiation detectors with a genetic algorithm. *Nuclear Instruments and Methods in Physics Research Section A: Accelerators, Spectrometers, Detectors and*

Associated Equipment, 927:54 – 62, 2019.

[24] V. Sánchez-Tembleque, V. Vedia, M. Carmona, L. M. Fraile, S. Ritt, and J. M. Udías. Digital strategies for time and energy measurement for ultra fast scintillators. In *2016 IEEE Nuclear Science Symposium, Medical Imaging Conference and Room-Temperature Semiconductor Detector Workshop (NSS/MIC/RTSD)*, pages 1–2, 2016.

[25] V. Sanchez-Tembleque, V. Vedia, L. M. Fraile, and J. M. Udias. Optimizing time-pickup algorithms in radiation detectors with a genetic algorithm. In *2017 IEEE Nuclear Science Symposium and Medical Imaging Conference (NSS/MIC)*, pages 1–3, 2017.

[26] L.M. Fraile, V. Sánchez-Tembleque, J. Benito, M. García-Díez, J.M. Udías, and V. Vedia. Advanced scintillators for fast-timing applications. *Nuclear Instruments and Methods in Physics Research Section B: Beam Interactions with Materials and Atoms*, 463:394 – 397, 2020.

[27] M. Garcia-Diez, V. Sanchez-Tembleque, L. M. Fraile, and J. Manuel Udías. High energy resolution inorganic scintillators read by sipm arrays. In *2019 IEEE Nuclear Science Symposium and Medical Imaging Conference (NSS/MIC)*, pages 1–3, 2019.

[28] PRONTO Project. `http://nuclear.fis.ucm.es/pronto/`.

[29] V. Sanchez-Tembleque, L. M. Fraile, V. Vedia, M. Carmona, K. Kamada, Y. Shoji, A. Yoshikawa, and J. M. Udias. Evaluation of inorganic scintillators for high performance tof pet applications. In *2015 IEEE Nuclear Science Symposium and Medical Imaging Conference (NSS/MIC)*, pages 1–4, 2015.

[30] V. Sanchez-Tembleque, L. M. Fraile, and J. M. Udias. Time over threshold data acquisition system for pet. In *2017 IEEE Nuclear Science Symposium and Medical Imaging Conference (NSS/MIC)*, pages 1–3, 2017.

[31] L.M. Fraile, H. Mach, V. Vedia, B. Olaizola, V. Paziy, E. Picado, and J.M. Udías. Fast timing study of a cebr3 crystal: Time resolution below 120ps at 60co energies. *Nuclear Instruments and Methods in Physics Research Section A: Accelerators, Spectrometers, Detectors and Associated Equipment*, 701:235 – 242, 2013.

[32] L.M. Fraile, H. Mach, E. Picado, V. Vedia, and J.M. Udías. Study of the time response of a luag(pr) crystal for fast timing applications. *Nuclear Instruments and Methods in Physics Research Section A: Accelerators, Spectrometers, Detectors and Associated Equipment*, 713:27 – 32, 2013.

[33] V. Vedia, H. Mach, L.M. Fraile, J.M. Udías, and S. Lalkovski. Enhanced time response of 1-

in. labr3(ce) crystals by leading edge and constant fraction techniques. *Nuclear Instruments and Methods in Physics Research Section A: Accelerators, Spectrometers, Detectors and Associated Equipment*, 795:144 – 150, 2015.

[34] V. Vedia, M. Carmona-Gallardo, L.M. Fraile, H. Mach, and J.M. Udías. Performance evaluation of novel labr3(ce) scintillator geometries for fast-timing applications. *Nuclear Instruments and Methods in Physics Research Section A: Accelerators, Spectrometers, Detectors and Associated Equipment*, 857:98 – 105, 2017.

[35] C. Fernández-Ramírez, E. De Guerra, A. Udias, and J. M. Udías. Properties of nucleon resonances by means of a genetic algorithm. *Physical Review C*, 78:65212, 06 2008.

[36] Saint Gobain. *Brillance 380 Brochure.*

[37] Hamamatsu Phonics. *Photomultiplier Tube R9779 Specifications*, 2009.

[38] S. Ritt. Design and performance of the 6 ghz waveform digitizing chip drs4. In *2008 IEEE Nuclear Science Symposium Conference Record*, pages 1512–1515, 2008.

[39] S. Ritt. *DRS4 Data Sheet.* Paul Scherrer Inst, Villigen, Switzerland, 0.9 edition, 2008. An optional note.

[40] D. Stricker-Shaver, S. Ritt, and B. J. Pichler. Novel calibration method for switched capacitor arrays enables time measurements with sub-picosecond resolution. *IEEE Transactions on Nuclear Science*, 61(6):3607–3617, 2014.

[41] W. K. Warburton and W. Hennig. New algorithms for improved digital pulse arrival timing with sub-gsps adcs. *IEEE Transactions on Nuclear Science*, 64(12):2938–2950, 2017.

[42] R. W. Hamming. *Digital Filters (3rd Ed.).* Prentice Hall International (UK) Ltd., GBR, 1989.

[43] D. E. Goldberg. *Genetic Algorithms in Search, Optimization & Machine Learning.* Addison-Wesley, Reading MA, 1989.

[44] L. Davis. *Handbook of Genetic Algorithms.* Van Nostrand Reinhold, New York, 1991.

[45] A. A. Torn and A. Zilinskas. Global optimization, notes in computer science 350 (springer-verlag, berlin, 1989).

[46] M. D. Vose. *The Simple Genetic Algorithm.* MIT Press, Cambridge, MA, 1999.

[47] Z. Michalewicz. *Genetic Algorithms + Data Structures = Evolution Programs.* Springer, Berlin/Heidelberg/New York, 1999.

[48] K. Deb. *Multi-Objective Optimization Using Evolutionary Algorithms.* Wiley, New York, 2002.

[49] J Cal-González, J L Herraiz, S España, P M G Corzo, J J Vaquero, M Desco, and J M Udias. Positron range estimations with PeneloPET. *Physics in Medicine and Biology*, 58(15):5127–5152, jul 2013.

[50] L. J. Eshelman and D. J. Shaffer. Preventing premature convergence in genetic algorithms by preventing incest. In *Proceedings of the 4th International Conference on Genetic Algorithms*, page 115, 1991.

[51] T. Back. Optimal mutation rates in genetic search. In *Proceedings of the 5th International Conference on Genetic Algorithms*, page 2, 1993.

[52] R.E. Bell. Comparison of leading-edge and crossover timing in coincidence measurements. *Nuclear Instruments and Methods*, 42(2):211 – 212, 1966.

[53] J. B. S. Waugh. Leading edge timing circuit for ge-li detectors. *IEEE Transactions on Nuclear Science*, 15(3):509–517, 1968.

[54] S. Seifert, R. Vinke, H. T. van Dam, H. Löhner, P. Dendooven, F. J. Beekman, and D. R. Schaart. Ultra precise timing with sipm-based tof pet scintillation detectors. In *2009 IEEE Nuclear Science Symposium Conference Record (NSS/MIC)*, pages 2329–2333, 2009.

[55] Mehmet Aykac, Inki Hong, and Sanghee Cho. Timing performance comparison of digital methods in positron emission tomography. *Nuclear Instruments and Methods in Physics Research Section A: Accelerators, Spectrometers, Detectors and Associated Equipment*, 623(3):1070 – 1081, 2010.

[56] B. Joly, G. Montarou, J. Lecoq, G. Bohner, M. Crouau, M. Brossard, and P. Vert. An optimal filter based algorithm for pet detectors with digital sampling front-end. *IEEE Transactions on Nuclear Science*, 57(1):63–70, 2010.

[57] Dennis R Schaart, Stefan Seifert, Ruud Vinke, Herman T van Dam, Peter Dendooven, Herbert Löhner, and Freek J Beekman. LaBr3:ce and SiPMs for time-of-flight PET: achieving 100 ps coincidence resolving time. *Physics in Medicine and Biology*, 55(7):N179–N189, mar 2010.

[58] Patrick Eckert, Hans-Christian Schultz-Coulon, Wei Shen, Rainer Stamen, and Alexander

Tadday. Characterisation studies of silicon photomultipliers. *Nuclear Instruments and Methods in Physics Research Section A: Accelerators, Spectrometers, Detectors and Associated Equipment*, 620(2):217 – 226, 2010.

[59] Z. Deng, Yanzhao Li, and Q. Xie. Quadratic programming time pickoff method for multi-voltage threshold digitizer in pet. In *2013 IEEE Nuclear Science Symposium and Medical Imaging Conference (2013 NSS/MIC)*, pages 1–4, 2013.

[60] Markus Jäger and Tilman Butz. Fpga implementation of digital constant fraction algorithm with fractional delay for optimal time resolution. *Nuclear Instruments and Methods in Physics Research Section A: Accelerators, Spectrometers, Detectors and Associated Equipment*, 674:24 – 27, 2012.

[61] A. Fallu-Labruyere, H. Tan, W. Hennig, and W.K. Warburton. Time resolution studies using digital constant fraction discrimination. *Nuclear Instruments and Methods in Physics Research Section A: Accelerators, Spectrometers, Detectors and Associated Equipment*, 579(1):247 – 251, 2007. Proceedings of the 11th Symposium on Radiation Measurements and Applications.

[62] Cheng-Ming Du, Jin-Da Chen, Xiu-Ling Zhang, Hai-Bo Yang, Ke Cheng, Jie Kong, Zheng-Guo Hu, Zhi-Yu Sun, Hong Su, and Hu-Shan Xu. Study of time resolution by digital methods with a DRS4 module. *Chinese Physics C*, 40(4):046101, apr 2016.

[63] M Nakhostin, Zs Podolyak, and P H Regan. Digital processing of signals from LaBr3:ce scintillation detectors. *Journal of Instrumentation*, 9(12):C12049–C12049, dec 2014.

[64] C.J. Prokop, S.N. Liddick, N.R. Larson, S. Suchyta, and J.R. Tompkins. Optimization of the national superconducting cyclotron laboratory digital data acquisition system for use with fast scintillator detectors. *Nuclear Instruments and Methods in Physics Research Section A: Accelerators, Spectrometers, Detectors and Associated Equipment*, 792:81 – 88, 2015.

[65] J. Glodo, W. W. Moses, W. M. Higgins, E. V. D. van Loef, P. Wong, S. E. Derenzo, M. J. Weber, and K. S. Shah. Effects of ce concentration on scintillation properties of labr/sub 3/:ce. *IEEE Transactions on Nuclear Science*, 52(5):1805–1808, 2005.

[66] Mikhail S. Alekhin, Sandra Weber, Karl W. Krämer, and Pieter Dorenbos. Optical properties and defect structure of sr2+ co-doped labr3:5scintillation crystals. *Journal of Luminescence*, 145:518 – 524, 2014.

[67] Saint Gobain. *Brillance 390S*.

[68] Martin Nikl and Akira Yoshikawa. Recent r&d trends in inorganic single-crystal scintillator materials for radiation detection. *Advanced Optical Materials*, 3(4):463–481, 2015.

[69] Fabio Acerbi and Stefan Gundacker. Understanding and simulating sipms. *Nuclear Instruments and Methods in Physics Research Section A: Accelerators, Spectrometers, Detectors and Associated Equipment*, 926:16 – 35, 2019. Silicon Photomultipliers: Technology, Characterisation and Applications.

[70] C. Mihai, G. Pascovici, G. Ciocan, C. Costache, V. Karayonchev, A. Lungu, N. Mărginean, R.E. Mihai, C. Neacşu, J.-M. Régis, A. Turturica, S. Ujeniuc, and A. Vasiliu. Development of large area silicon photomultipliers arrays for γ-ray spectroscopy applications. *Nuclear Instruments and Methods in Physics Research Section A: Accelerators, Spectrometers, Detectors and Associated Equipment*, 953:163263, 2020.

[71] Tommaso Cervi, Marta Babicz, Maurizio Bonesini, Andrea Falcone, Alessandro Menegolli, Gian Luca Raselli, Massimo Rossella, and Marta Torti. Characterization of sipm arrays in different series and parallel configurations. *Nuclear Instruments and Methods in Physics Research Section A: Accelerators, Spectrometers, Detectors and Associated Equipment*, 912:209 – 212, 2018. New Developments In Photodetection 2017.

[72] A. Fazzi, M. Nocente, M. Tardocchi, V. Varoli, G. Gorini, M. Lorenzoli, C. Pirovano, G. Valvo, G. Fallica, and C. Cazzaniga. A large area sipm array coupled to a labr3 crystal for a tpr spectrometer. In *2013 IEEE Nuclear Science Symposium and Medical Imaging Conference (2013 NSS/MIC)*, pages 1–4, 2013.

[73] Alexei Ulyanov, Oran Morris, Lorraine Hanlon, Sheila McBreen, Suzanne Foley, Oliver J. Roberts, Isaac Tobin, David Murphy, Colin Wade, Nick Nelms, Brian Shortt, Tomas Slavicek, Carlos Granja, and Michael Solar. Performance of a monolithic labr3:ce crystal coupled to an array of silicon photomultipliers. *Nuclear Instruments and Methods in Physics Research Section A: Accelerators, Spectrometers, Detectors and Associated Equipment*, 810:107 – 119, 2016.

[74] G. L. Montagnani, L. Buonanno, D. Di Vita, A. Minerva, M. Carminati, F. Camera, A. Gola, V. Regazzoni, F. Acerbi, and C. Fiorini. Development of 3" labr3 sipm-based detection modules for high dynamic range gamma ray spectroscopy and imaging. In *2018 IEEE Nuclear Science Symposium and Medical Imaging Conference Proceedings (NSS/MIC)*, pages 1–2, 2018.

[75] Minicircuits datasheet zfl-500ln-bnc+. `https://www.minicircuits.com/WebStore/dashboard.html?model=ZFL-500LN-BNC%2B`.

[76] R. Vinke, S. Seifert, D. R. Schaart, F. P. Schreuder, M. R. de Boer, H. T. van Dam, F. J. Beekman, H. Löhner, and P. Dendooven. Optimization of digital time pickoff methods for

labr3-sipm tof-pet detectors. In *2009 IEEE Nuclear Science Symposium Conference Record (NSS/MIC)*, pages 2962–2968, 2009.

[77] ON Semiconductor. *Introduction to the Silicon Photomultiplier (SiPM)*, 2018.

[78] M. Garcia-Diez et al, private communication.

[79] Kathryn D Held, Antony J Lomax, and Esther G C Troost. Proton therapy special feature: introductory editorial. *The British Journal of Radiology*, 93(1107):20209004, 2020. PMID: 32081045.

[80] Robert R. Wilson. Radiological use of fast protons. *Radiology*, 47(5):487–491, 1946. PMID: 20274616.

[81] S E McGowan, N G Burnet, and A J Lomax. Treatment planning optimisation in proton therapy. *The British Journal of Radiology*, 86(1021):20120288–20120288, 2013. PMID: 23255545.

[82] Tai-Ze Yuan, Ze-Jiang Zhan, and Chao-Nan Qian. New frontiers in proton therapy: applications in cancers. *Cancer Communications*, 39(1):61, 2019.

[83] Antje-Christin Knopf and Antony Lomax. In vivo proton range verification: a review. *Physics in Medicine and Biology*, 58(15):R131–R160, jul 2013.

[84] M Mumot, C Algranati, M Hartmann, J M Schippers, E Hug, and A J Lomax. Proton range verification using a range probe: definition of concept and initial analysis. *Physics in Medicine and Biology*, 55(16):4771–4782, aug 2010.

[85] Katia Parodi and Jerimy C. Polf. In vivo range verification in particle therapy. *Medical Physics*, 45(11):e1036–e1050, 2018.

[86] Katia Parodi, Harald Paganetti, Helen A. Shih, Susan Michaud, Jay S. Loeffler, Thomas F. DeLaney, Norbert J. Liebsch, John E. Munzenrider, Alan J. Fischman, Antje Knopf, and Thomas Bortfeld. Patient study of in vivo verification of beam delivery and range, using positron emission tomography and computed tomography imaging after proton therapy. *International Journal of Radiation Oncology*Biology*Physics*, 68(3):920 – 934, 2007.

[87] S. España, X. Zhu, J. Daartz1a, G. El Fakhria, T. Bortfeld, and H. Paganetti. The reliability of proton-nuclear interaction cross-section data to predict proton-induced pet images in proton therapy. *Physics in Medicine and Biology*, 56(2687), 2011.

[88] I. Perali, A. Celani, P. Busca, C. Fiorini, A. Marone, M. Basilavecchia, T. Frizzi,

F. Roellinghoff, J. Smeets, D. Prieels, F. Stichelbaut, F. Vander Stappen, S. Henrotin, and A. Benilov. Prompt gamma imaging with a slit camera for real-time range control in proton therapy: Experimental validation up to 230 mev with hicam and development of a new prototype. In *2012 IEEE Nuclear Science Symposium and Medical Imaging Conference Record (NSS/MIC)*, pages 3883–3886, 2012.

[89] V. Valladolid-Onecha. Verificacion de Rango de Protones mediante el uso de Contrastes. Master's thesis, Unviersidad Complutense de Madrid, Madrid, 2018.

[90] A. Espinosaa. Erasmus Mundus Joint Master Degree on Nuclear Physics. Master's thesis, Unviersidad Complutense de Madrid, Madrid, 2018.

[91] PicoTechnology. *PicoScope Serie 6000 Datasheet.*

[92] Zhang Huaiqiang, Bin Tang, He-Xi Wu, and Zhuo-Dai Li. Study of sallen–key digital filters in nuclear pulse signal processing. *Nuclear Science and Techniques*, 30, 10 2019.

[93] J. Sempau F. Salvat, J. Fernández-Varea. *PENELOPE-2008: A Code System for Monte Carlo Simulation of Electron and Photon Transport.* 2009.

[94] Jeffrey J. Pasternak and Eric E. Williamson. Clinical pharmacology, uses, and adverse reactions of iodinated contrast agents: A primer for the non-radiologist. *Mayo Clinic Proceedings*, 87(4):390 – 402, 2012.

[95] Nuclear structure and decay data. https://www.nndc.bnl.gov/nudat2/).

[96] Victor Sanchez-Tembleque, Daniel Sanchez-Parcerisa, Victor Valladolid-Onecha, Luis Mario Fraile, and Jose Manuel Udias. Simultaneous measurement of the spectral and temporal properties of a linac pulse from outside the treatment room. *Radiation Physics and Chemistry*, 158:1 – 5, 2019.

[97] A S Beddar, T R Mackie, and F H Attix. Water-equivalent plastic scintillation detectors for high-energy beam dosimetry: I. physical characteristics and theoretical considerations. *Physics in Medicine and Biology*, 37(10):1883–1900, oct 1992.

[98] J. Kim, E. Park, Y. Jung, B. C. Kim, J. H. Kim, C. Yi, I. J. Kim, and C. Kim. X-ray acoustic-based dosimetry using a focused ultrasound transducer and a medical linear accelerator. *IEEE Transactions on Radiation and Plasma Medical Sciences*, 1(6):534–540, 2017.

[99] Olivia M Giza, Daniel Sánchez-Parcerisa, Víctor Sánchez-Tembleque, Joaquin L Herraiz, Jorge Camacho, Stephen Avery, and José Manuel Udías. Photoacoustic dose monitoring in

clinical high-energy photon beams. *Biomedical Physics & Engineering Express*, 5(3):035028, apr 2019.

[100] D. Sanchez-Parcerisa, O. Giza, J. Camacho, V. Sanchez-Tembleque, S. Avery, and J. Udias. Ep-1734: Photo- and proto- acoustic dose monitoring in radiosurgery and proton beams. *Radiotherapy and Oncology*, 127:S928, 2018. ESTRO 37, April 20-24, 2018, Barcelona, Spain.

[101] S. Hickling, P. Léger, and I. El Naqa. On the detectability of acoustic waves induced following irradiation by a radiotherapy linear accelerator. *IEEE Transactions on Ultrasonics, Ferroelectrics, and Frequency Control*, 63(5):683–690, 2016.

[102] M. E. Garcia, G. M. Pastor, and K. H. Bennemann. Theory for the photoacoustic response to x-ray absorption. *Phys. Rev. Lett.*, 61:121–124, Jul 1988.

[103] Norman A. Baily. A review of the processes by which ultrasound is generated through the interaction of ionizing radiation and irradiated materials: Some possible applications. *Medical Physics*, 19(3):525–532, 1992.

[104] J. Brownridge, S. Samnick, P. Stiles, P. Tipton, J. Veselka, and N. Yeh. Determination of the photon spectrum of a clinical accelerator. *Medical Physics*, 11(6):794–796, 1984.

[105] Carel W E van Eijk. Inorganic scintillators in medical imaging. *Physics in Medicine and Biology*, 47(8):R85–R106, apr 2002.

[106] E. Picado, M. Carmona-Gallardo, J. Cal-González, L.M. Fraile, H. Mach, J.M. Udías, and V. Vedia. Efficiency measurement and monte carlo simulations of a cebr3 scintillator. *Applied Radiation and Isotopes*, 120:71 – 75, 2017.

[107] C.-M. Ma and S.B. Jiang. Monte carlo modelling of electron beams from medical accelerators. *Physics in Medicine and Biology*, 44(12):R157–R189, 1999. cited By 130.

[108] G.X. Ding. Energy spectra, angular spread, fluence profiles and dose distributions of 6 and 18 mv photon beams: Results of monte carlo simulations for a varian 2100ex accelerator. *Physics in Medicine and Biology*, 47(7):1025–1046, 2002. cited By 131.

[109] F. Verhaegen and J. Seuntjens. Monte carlo modelling of external radiotherapy photon beams. *Physics in Medicine and Biology*, 48(21):R107–R164, 2003. cited By 270.

[110] William A. Tobias Yuan Zheng, G. Wilson Miller and Gordon D. Cates. A method for imaging and spectroscopy using γ-rays and magnetic resonance. *Nature*, 537:652 – 655, 2016.

[111] Yuan Zheng. *Low field MRI and the Development of Polarized Nuclear Imaging (PNI) - A New Imaging Modality.* PhD thesis, University of Virginia, 2016.

[112] Rachel W. Chan, Justin Y.C. Lau, Wilfred W. Lam, and Angus Z. Lau. Magnetic resonance imaging. In Roger Narayan, editor, *Encyclopedia of Biomedical Engineering*, pages 574 – 587. Elsevier, Oxford, 2019.

[113] M. S. Albert, G. D. Cates, B. Driehuys, W. Happer, B. Saam, C. S. Springer, and A. Wishnia. Biological magnetic resonance imaging using laser-polarized 129xe. *Nature*, 370:199 – 201, 1994.

[114] Danila A. Barskiy, Aaron M. Coffey, Panayiotis Nikolaou, Dmitry M. Mikhaylov, Boyd M. Goodson, Rosa T. Branca, George J. Lu, Mikhail G. Shapiro, Ville-Veikko Telkki, Vladimir V. Zhivonitko, Igor V. Koptyug, Oleg G. Salnikov, Kirill V. Kovtunov, Valerii I. Bukhtiyarov, Matthew S. Rosen, Michael J. Barlow, Shahideh Safavi, Ian P. Hall, Leif Schröder, and Eduard Y. Chekmenev. Nmr hyperpolarization techniques of gases. *Chemistry – A European Journal*, 23(4):725–751, 2017.

[115] N. R. Steenberg. Angular distribution of γ-radiation from polarized nuclei. *Phys. Rev.*, 84:1051–1052, Dec 1951.

[116] M. Kitano, F. P. Calaprice, M. L. Pitt, J. Clayhold, W. Happer, M. Kadar-Kallen, M. Musolf, G. Ulm, K. Wendt, T. Chupp, J. Bonn, R. Neugart, E. Otten, and HT Duong. Nuclear orientation of radon isotopes by spin-exchange optical pumping. *Nu. Phys Rev Lett.*, pages 2133–2136, 1988.

[117] Laser Operations LCC, Sylmar, CA, Sylmar, CA. *Datasheet.*

[118] R. Y. Engel. Planing, Simulation and Preparation of a Magnetic Resonant Imaging Experiment based on the Detection of Anisotropic gamma-Radiation from Hyperpolarized Isomers. Master's thesis, Carl-von-Ossietzky Universit at Oldenburg, European Center for Nuclear Research, Hochschule Emden/Leer, Geneve, 2018.

[119] E. L. Wistrom. Developing gamma-MRI with the Hyperpolarization of ^{129m}Xe and ^{131m}Xe by Spin Exchange Optical Pumping. Master's thesis, Faculty of Mathematics and Natural Sciences University of Oslo, Oslo, 2020.

[120] F. P. Calaprice, W. Happer, D. F. Schreiber, M. M. Lowry, E. Miron, and X. Zeng. Nuclear alignment and magnetic moments of ^{133}Xe, ^{133}Xe^{m}, and ^{131}Xe^{m} by spin exchange with optically pumped ^{87}Rb. *Phys. Rev. Lett.*, 54:174–177, Jan 1985.

[121] M. Kitano, M. Bourzutschky, F. P. Calaprice, J. Clayhold, W. Happer, and M. Musolf.

Measurement of magnetic dipole moments of $^{129}\mathrm{Xe}^{\mathrm{m}}$ and $^{131}\mathrm{Xe}^{\mathrm{m}}$ by spin exchange with optically pumped rb. *Phys. Rev. C*, 34:1974–1979, Nov 1986.